UNIVERSITY OF CALIFORNIA,

IRVINE

Turbulent Transport of Energetic Ions and Thermal Plasma

DISSERTATION

submitted in partial satisfaction of the requirements
for the degree of

DOCTOR OF PHILOSOPHY

in Physics

by

Shu Zhou

Dissertation Committee:
Professor William Heidbrink, Co-chair
Professor Roger McWilliams, Co-chair
Professor Zhihong Lin

2011

TABLE OF CONTENTS

LIST OF FIGURES

LIST OF TABLES

ACKNOWLEDGEMENT

Though only my name appears on the cover of this dissertation, a great many people have contributed to its production. I owe my gratitude to all those people who have made this dissertation possible and because of whom my graduate experience has been one that I will cherish forever.

Foremost, I would like to express my sincere gratitude to my advisors, Prof. William Heidbrink and Prof. Roger McWilliams, for their continuous support of my Ph. D. study and research, for their patience, motivation, enthusiasm, and immense knowledge. Their guidance helped me in all the time of research and writing of this thesis. They also always serve as my mentors in many aspects of my U. S. life.

Bill is such an energetic scientist. Working with him at the LAPD is always exciting learning experience. His dedication and attitude to science deeply influence me. He also teaches me how to work with great patience and efficiency, which will benefit me throughout my life.

I spent most of my Ph. D. life sitting behind Roger in his giant cubical laboratory. He is an encyclopedia, a realistic scientist, and a best counselor for everything. I always enjoy talking with him and glean a lot of insight. He helped me incorporate myself much better into this country as a foreigner. He also teaches me to be skeptical and think independently. I am so blessed to have Bill and Roger as my co-advisors.

I would like to thank Dr. Heinrich Boehmer for providing brilliant ideas and guidance to help my research. Heinz always has great ideas which can lead to successful experiments. His invaluable wisdoms lead me through my research and personal life.

My sincere thanks also go to Dr. Yang Zhang. He led me into this research project, and he is always a role model to me as a good researcher. My experiments are all based on the reliable hardware designed and developed by Heinz and him.

I would also like to thank the LAPD group at UCLA, including Prof. Walter Gekelman, Prof. Troy Carter, Dr. Steve Vincena, Dr. Shreekrishna Tripathi, Dr. Bart Compernolle, Marvin Drandell, Zoltan Lucky and Patrick Prybil for their hospitality at the facility and indispensible support to this thesis work. LAPD is a great facility for basic plasma physics study with state-of-the-art hardware and the most professional research team. None of my works is possible without the dedication of all the supporting researchers.

Last but not the least, I would like to thank my family: my parents Jianwei Zhou and Huili Jiang, for educating and supporting me throughout my life; my fiancée Yi Sun for always being with me through the good times and bad times of my graduate life.

CURRICULUM VITAE

FIELD OF STUDY:

Experimental Plasma Physics

EDUCATION:

Ph. D. in Plasma Physics,

University of California, Irvine 2007-2011

M.S. in Plasma Physics,

University of California, Irvine 2007-2009

B.S. in Applied Physics,

University of Science and Technology of China 2003-2007

PUBLICATIONS

"Dependence of fast-ion transport on the nature of the turbulence in the Large Plasma Device", Shu Zhou, W. W. Heidbrink, H. Boehmer, R. McWilliams, T. A. Carter, S. Vincena, S. K. P. Tripathi, Physics of plasmas **18**, 082104 (2011)

"Sheared-Flow Induced Confinement Transition in a Linear Magnetized Plasma", Shu Zhou, W. W. Heidbrink, H. Boehmer, R. McWilliams, T. A. Carter, S. Vincena, B. Friedman, D. Schaffner, submitted for publication in Physics of Plasmas, 2011

"Turbulent transport of fast ions in the Large Plasma Device", Shu Zhou, W. W. Heidbrink, H. Boehmer, R. McWilliams, T. A. Carter, S. Vincena, S. K. P. Tripathi, P. Popovich, B. Friedman, and F. Jenko, Phys. Plasmas, **17**, 092103 (2010)

"Doppler-shifted cyclotron resonance of fast ions with circularly polarized shear Alfvén waves", Yang Zhang, W. W. Heidbrink, Shu Zhou, H. Boehmer, R. McWilliams, T. A. Carter, S. Vincena, and M. K. Lilley, Phys. Plasmas, **16**, 055706 (2009)

PRESENTATIONS

"Study of Fast Ion Transport in Turbulent Waves in the Large Plasma Device"
Invited Talk, American Physical Society-Division of Plasma Physics, Salt Lake City, Nov. 2011, Shu Zhou
"Turbulent Transport of Fast Ions in the Large Plasma Device"
Joint EU-US Transport Task Force Workshop 2011, San Diego, CA, Apr. 2011
Shu Zhou, W. W. Heidbrink, H. Boehmer, R. McWilliams, T. A. Carter, S. Vincena, S. K. P. Tripathi

"Study of Turbulent Transport of Fast Ions in the Large Plasma Device"
Centre de Recherches en Physique des Plasmas, École Polytechnique Fédérale De Lausanne (EPFL), Lausanne, Switzerland, Dec. 2010
Shu Zhou, W. W. Heidbrink, H. Boehmer, R. McWilliams, T. A. Carter, S. Vincena, S. K. P. Tripathi

LIST OF SYMBOLS

$\mathbf{B}_0$	Ambient Magnetic Field
d_{port}	Distance Between Two Diagnostic Ports at LAPD
$D_{\perp}$	Diffusion Coefficient in Perpendicular Direction (To the Magnetic Fields)
e	Electronic Charge
I_{sat}	Ion Saturation Current
k_B	Boltzmann's Constant
$k_{\|\|}$, k_z	Wave Vector Component Parallel To $\boldsymbol{B}_0$
$k_{\perp}$	Wave Vector Component Perpendicular To $\boldsymbol{B}_0$
K	Kubo number
m	Mass; Wave Mode Number
M_i	Mass of Thermal Plasma Ions
n_e	Electron Density
n_i	Plasma Ion Density
t	Time
T_e	Thermal Electron Temperature
T_i	Thermal Ion Temperature
T_f	Fast Ion Cyclotron Period
$v_{\perp}$	Velocity Component Perpendicular To Magnetic Field
$v_{\|\|}$, v_z	Velocity Component Parallel To Magnetic Field
$\mathbf{v}_e$	Thermal Electron Velocity
$\mathbf{v}_i$	Thermal Ion Velocity
$\mathbf{v}_f$	Fast Ion Velocity
$\mathbf{v}_{De}$	Electron Diamagnetic Drift Velocity
$\mathbf{v}_{drift}$	Drift Velocity of the Fast Ions
V_f	Plasma Floating Potential
V_p	Plasma Potential
z	Axial Position In The LAPD Parallel To $\boldsymbol{B}_0$
δB	Magnetic Fluctuation Intensity
ϕ	Electric Potential
λ_c	Correlation Length of the Turbulent Waves

ε_0	Permittivity Of Free Space
θ	Pitch Angle of the Fast Ion Beam
θ_x	Cross Phase Between Two Signals
ω_{ci}	Plasma Ion Cyclotron Frequency
ρ_i	Thermal Ion Gyro Radius
ρ_f	Fast Ion Gyro Radius
ρ_e	Thermal Electron Gyro Radius
ρ_s	Thermal Ion Sound Radius
τ_c	Correlation Time of the Turbulent Waves
τ_{PAS}	Pitch Angle Scattering Time
Γ	Particle Flux
γ	Coherency
χ^2	Chi Square Test
$\mu 0$	Permeability Of Free Space
Ω_f	Fast Ion Gyro-Frequency

ABSTRACT OF THE DISSERTATION

Turbulent Transport of Fast Ions and Thermal Plasmas

By

Shu Zhou

Doctor of Philosophy in Physics

University of California, Irvine, 2011

Professor William Heidbrink, Co-chair

Professor Roger McWilliams, Co-chair

Three experiments are conducted to study the effect of the turbulent waves on the transport of fast ions and thermal plasmas. In the first experiment, strong drift wave turbulence with linear geometry is observed in the Large Plasma Device (LAPD) on density gradients produced by a plate limiter. Energetic lithium ions orbit through the turbulent region. Scans with a collimated ion analyzer and with Langmuir probes give detailed profiles of the fast ion spatial distribution and the fluctuating fields. The fast-ion transport decreases rapidly with increasing fast-ion gyroradius. Unlike the diffusive transport caused by Coulomb collisions, in this case the turbulent transport is super-diffusive. Analysis and simulation suggest that such super-diffusive transport is due to the interaction of the fast ions with the low-frequency two-dimensional electrostatic turbulence.

The second experiment studies the dependence of the fast ion transport on the nature of the turbulent waves. Strong turbulent waves with cylindrical geometry are observed in the LAPD on density gradients produced by an annular obstacle. The characteristics of the fluctuations are modified by changing the plasma species from helium to neon, and by modifying the bias on the obstacle. Different spatial structure sizes (L_s) and correlation lengths (L_{corr}) of the wave potential fields alter the fast ion transport. The effects of electrostatic fluctuations are reduced due to gyro-averaging, which explains the difference in the fast-ion transport. A transition from super-diffusive to sub-diffusive transport is observed when the fast ion interacts with the waves for most of a wave period, which agrees with theoretical predictions.

The transport of thermal plasmas under electrostatic waves is explored in the third experiment. Sheared azimuthal flow is driven at the edge of a magnetized plasma cylinder

through edge biasing. Strong fluctuations of density and potential ($\delta n / n \sim e\delta\phi / kT_e \sim 0.5$) are observed at the plasma edge, accompanied by large density gradient ($L_n = |\nabla \ln n|^{-1} \sim 2cm$) and shearing rate ($\gamma \sim 300kHz$). Edge turbulence and cross-field transport are modified by changing the bias voltage (V_{bias}) on the obstacle and the axial magnetic field (B_z) strength. In cases with low V_{bias} and large B_z, improved plasma confinement is observed, along with steeper edge density gradients. The radially sheared flow induced by $E \times B$ drift dramatically changes the cross-phase between density and potential fluctuations, which causes the wave-induced particle flux to reverse its direction across the shear layer and forms a transport barrier. In cases with higher bias voltage or smaller B_z, large radial transport and rapid depletion of the central plasma density are observed. Two-dimensional cross-correlation measurement shows that a mode with azimuthal mode number $m = 1$ and large radial correlation length dominates the outward transport in these cases. Linear analysis based on a two-fluid Braginskii model suggests that the fluctuations are driven by both density gradient and flow shear at the plasma edge.

Chapter 1
INTRODUCTION

1.1 Fast Ion Transport in Microturbulence

The influence of microturbulence on fast ion behavior in plasmas has attracted growing interest in fusion and space physics. Fast ions are ions with energies that are much larger than typical thermal plasma ions. These energetic ions execute orbits that are much larger than those of thermal particles in plasma ($\rho_f >> \rho_i >> \rho_e$, where ρ_f, ρ_i and ρ_e are the gyro radius of fast ion, thermal ions and thermal electrons). The velocity of fast ions (v_i) is usually intermediate between that of thermal electrons and thermal ions ($v_i << v_f << v_e$). The large orbit size and velocity make the fast ions interact differently with microturbulence in plasmas compared to thermal particles. Confinement of the fast ions is a critical issue in fusion experiments approaching ignition[1-2], and many space and astrophysical problems (see, e. g., Ref. 3 and references therein) depend on understanding fast ion dynamics in a turbulent medium. Many fast ion transport measurements in tokamaks are consistent with classical theory, yielding lower-level diffusion compared to thermal ions[2]. But some recent tokamak studies[4-8] observe anomalous transport of fast ions, in seeming contradiction with earlier experimental results and theories.

A widely accepted explanation for the low transport of fast ions is that energetic ions phase average over the microturbulence structure along its large gyro and drift orbits[9-11]. The typical decorrelation length or structure size of the plasma microturbulence is on the scale of the thermal ion gyroradius, which is much smaller than the orbit size of the fast ions. The idea of "gyroaveraging" states that the effective electrostatic or electromagnetic field applied to a fast ion is the average of the fields along one gyro orbit. In a tokamak, the fast ion trajectory is a combination of gyro orbit and drift orbit (either passing orbit or trapped orbit depending on its pitch angle parameter), thus gyroaveraging and orbit-averaging are both considered. In a simple linear device (such as the Large Plasma Device), the fast ion trajectory is mainly gyro motion, thus gyroaveraging is the major mechanism affecting the fast-ion interaction with the turbulent waves.

The validity of gyroaveraging depends on the spatial and temporal correlation between the fast ion orbit and the turbulent wave fields. The gyroaveraging effect is valid under the following assumption: the fast ion cyclotron period is much smaller than any of the wave time scale ($T_f << T_{wave}, \tau_c$, or $\Omega_f >> \omega_{wave}$), in other words, the background microturbulent fields are approximately static during one fast-ion gyro orbit. Furthermore, the fast-ion perturbed drift during one gyro-orbit is much smaller than the fast-ion gyroradius

($\bar{v}_{drift} \cdot T_f << \rho_f$), which means that the nonlinear frequency experienced by particle is much smaller than the cyclotron frequency ($\Omega_f >> \rho_f/v_{drift}$). With this assumptions, the turbulent wave field ϕ a fast ion feels can be replaced by the gyro-averaged value over a fast ion Larmor orbit:

$$\langle\phi\rangle(x_0) = \frac{1}{2\pi}\oint d\theta\, \phi(\bar{x}_0 + \bar{\rho}_f(\theta)) \qquad (1.1)$$

Where x_0 is the position of the gyro center and ρ_f is the gyro motion vector. We further assume that the Larmor orbit of a fast-ion is circular to a good approximation. Using discrete Fourier transform, the averaged potential can be written as

$$\begin{aligned}\langle\phi\rangle(x_0) &= \frac{1}{2\pi}\oint d\theta \sum_k \phi_k e^{i\bar{k}\cdot(\bar{x}_0+\bar{\rho}_f(\theta))} \\ &= \frac{1}{2\pi}\oint d\theta \sum_k \phi_k e^{i\bar{k}\cdot\bar{x}_0}\cdot\phi_k e^{i\bar{k}\cdot\bar{\rho}_f(\theta)} \\ &= \sum_k \phi_k e^{i\bar{k}\cdot\bar{x}_0}\frac{1}{2\pi}\oint d\theta\,\phi_k e^{i\bar{k}\cdot\bar{\rho}_f(\theta)} \\ &= \sum_k \phi_k e^{i\bar{k}\cdot\bar{x}_0} J_0(k\rho_f)\end{aligned} \qquad (1.2)$$

This equation reveals that the effect of gyroaveraging depends on ($k\rho_f$) or (ρ_f/λ), in which ρ_f is the fast ion orbit size, k and λ are the wave number and the spatial scale length of the turbulent field. A larger ratio of (ρ_f/λ) means that the fast-ion averages over more turbulent structures during one gyro-motion, which leads to a smaller effective potential on the fast ion. The typical value for (ρ_f/λ) for the fast particles produced in the fusion reaction is of the order of 10.

The gyroaveraging model describes the fast-ion motion in small amplitude, nearly static, 2D electrostatic turbulent fields very well. However, it fails when the time scale separation is not satisfied. For example, when the correlation time of the turbulent wave is short comparing with the fast-ion gyro period ($\tau_c < T_f$), then the background turbulent fields cannot be assumed static during one gyro orbit, and the averaging effect is different. The so-called Kubo number[12-13] is used in some simulation works to distinguish the fast-ion transport in microturbulence with different time scales. Kubo number is defined as $K = \frac{\tau_c}{\tau_{de}}$, where τ_c is the correlation time of the turbulent waves, and $\tau_{de} = \lambda_c / v_{drift}$ characterizes the scale time of the fast-ion drifting over the wave correlation length (λ_c). A systematic simulation study of the dependence of the fast-ion transport on Kubo number can be found in Ref. 12.

The gyroaveraging model depicts the spatial and energy dependence of the fast ion transport, while the time dependence of the transport can be described by the

autocorrelation of the fast ion velocity. Generally, the time dependence of the diffusion coefficient in a transport procedure can be expressed as[14]

$$D(t) = \int_0^t d\tau \cdot L_{ii}(\tau) \quad (1.3)$$

where $L_{ii}(t) = \langle \upsilon_i(0,0)\upsilon_i(x,t) \rangle$ is the Lagrangian autocorrelation function of the respective particle velocity. This equation shows that, as long as a Lagrangian correlation between the current particle velocity and its velocity at the starting point exists, the transport is in general non-diffusive. A typical relation between the diffusivity D and the wave-particle interaction time is shown in Fig. 3 of Ref. 15. Generally, for small times, before a particle feels the structure or the time dependence of the turbulent structures, the transport is super-diffusive, with $\upsilon_i(0,0) \cong \upsilon_i(x,t)$ and the diffusivity increase with time, $D(t) = \alpha t$. When the time scale of the wave-particle interaction is comparable to the wave period, the particle starts to feel the changes in phase and structure of the waves. The transport in this time scale is sub-diffusive, with D(t) decreasing in time. Only when the particle is fully decorrelated with the initial wave structures, $L_{ii}(t) = \langle \upsilon_i(0,0)\upsilon_i(x,t) \rangle = 0$ and the diffusivity D becomes a constant, is the particle motion diffusive.

More theoretical and simulation works published in recent years are focused on the transport of the energetic ions in toroidal geometry, which aims to explain the transport experiments in toroidal fusion devices. The energy scaling of the energetic particle transport has been thoroughly studied in both electrostatic and magnetic microturbulence[16-18]. However, these investigations disagree on the mechanisms and scaling dependencies of transport: Some claim the orbit averaging is rarely operative[16], while others suggest orbit averaging is generally valid for energetic ions[17]. Consequently the prediction of the scaling of fast ion diffusivity is controversial.

Experimentally, the study of fast ion transport by microturbulence is challenging. Diagnostic tools in fusion devices are limited to non-contact methods. In neutral-beam current drive experiments in ASDEX-Upgrade[4, 19], anomalous transport is inferred from the time evolution of the current profile. In DIII-D[6], spectroscopic and current-profile measurements provide evidence of transport in excess of neoclassical levels under some conditions[20-21]. Measurement in a toroidal magnetized plasma device (TORPEX) has begun[22-23]. In this thesis work, we report direct measurements of fast-ion transport in the presence of drift-wave turbulence. The Large Plasma Device (LAPD)[24] at UCLA provides a probe-accessible (see Chapter 2.2) plasma with comparable dimension to magnetic fusion devices. In order to destabilize low-frequency drift waves, a density gradient was created by placing an obstacle in the chamber to block primary electrons from the cathode-anode source[25]. The approach discussed in this thesis was to launch test-particle fast ion beams[26-27] with narrow initial width in phase space and to have the fast ion gyro orbit overlap with

the turbulent potential structure of the turbulence. Then the fast ion beam was detected at different distances away from the fast ion source by a collimated ion analyzer. This allows study of fast ion transport in phase space with time and space resolution. This technique has been successfully used in previous studies of fast ion classical diffusion[28] and of resonance with shear Alfven waves (SAW)[29-30]. A summary of the previous experimental works of the fast ion project at UC Irvine is given in Sec 1.3.

1.2 Thermal Plasma Transport in Electrostatic Waves

Modification of the plasma edge turbulence and turbulent transport has attracted continuous interest since the discovery of the high-confinement mode (H-mode), where a strong and sudden change in plasma characteristics, leading to improved energy confinement, is observed. H-mode in tokamaks[31] is triggered mostly when the heating power exceeds a threshold. Many experiments[32] and theories[33] ascribed the improved confinement to the formation of the steady sheared flows, which can stabilize plasma turbulence and form a transport barrier. The sheared flow in plasmas can be spontaneously generated by nonlinear interaction of the edge turbulence (zonal flows), or induced by externally applied radial electric fields ($E \times B$ drift). Experiments in the Continuous Current Tokamak (CCT)[34] were the first to demonstrate that a sharp transport barrier, accompanied by an H-mode like state, can be triggered by applied radial electric fields. Subsequently, many experiments have used external bias to study modification of the plasma turbulence and transport[35-38].

The basic physics involved in transport reduction by external bias is the effect of E×B velocity shear on the growth of and radial extension of the turbulent eddies in the plasma. The E×B drift is one of the most fundamental particle motions, regardless of the charge or mass of the particles. This provides a universal mechanism for affecting turbulence. In theory, the sheared E×B flow affects the edge turbulence and transport in two ways. The first is nonlinear decorrelation of turbulent structures[39], leading to a reduction in transport even though the underlying turbulence is not completely suppressed. The second is linear stabilization of the modes[40], leading to transport reduction through suppression of the fluctuations. The suppression of transport by decorrelation of the turbulent structures can be simply understood by evaluating the particle flux profiles. Assuming the particle transport is mainly driven by electrostatic E×B drift, the particle flux[38] is:

$$\begin{aligned}\Gamma_n &= \langle n v_r \rangle = \frac{\langle n E_\theta \rangle}{B_z} \\ &= \frac{2}{B}\int_0^\infty |n(\omega)||E_\theta(\omega)|\gamma_{n,E_\theta}(\omega)\cos(\theta_{n,E_\theta}(\omega))d\omega\end{aligned} \qquad (1.4)$$

where $n(\omega)$ and $E_\theta(\omega)$ are the FFT density and azimuthal electric field, $\gamma_{n,E_\theta}(\omega)$ and $\theta_{n,E_\theta}(\omega)$ are the cross-coherency and cross-phase between $n(\omega)$ and $E_\theta(\omega)$. Flow and flow shear can modify both the cross-phase $\theta_{n,E_\theta}(\omega)$ and the cross-coherency $\gamma_{n,E_\theta}(\omega)$ between density and potential fluctuations, leading to a reduction of transport even in the absence of amplitude reduction.

The linear stability effects of E×B velocity and velocity shear are more complex, since the physics is mode specific. Generally, the E×B velocity shear results in enhanced damping by mode coupling. On the other hand, sheared flow also provides a source of free energy to drive turbulence through mechanisms such as Kelvin-Helmholtz instability. It is sometimes argued[41] that in plasma, magnetic shear is capable of suppressing Kelvin-Helmholtz mode. However, the stability analysis of the edge modes is usually sensitive to geometry in this case, as well as the plasma equilibrium profiles and other parameters. So analytical modeling and simulation studies based on the specific parameters of the experimental device are needed

Recent experiments[38, 42-43] in the Large Plasma Device (LAPD) at the University of California, Los Angeles (UCLA) have studied the effect of the sheared flow on the edge turbulence and turbulent transport by biasing a section of the vacuum chamber wall. Linear and nonlinear simulations aimed to model the plasma instabilities based on LAPD parameters are also developed[44-45]. In the current experiment, an annular-shaped obstacle with inner radius of *6cm* is placed concentrically with the main plasma of LAPD. The obstacle partially blocks the plasma source and induces a plasma column with 12cm in diameter downstream. The obstacle is biased by an external power supply, leading to sheared $E \times B$ drift at the edge of the plasma column. Modifications of the plasma characteristics and turbulent transport by changing the amplitude of the bias on the obstacle (V_{bias}), the axial magnetic field (B_z) strength and the plasma species (helium or neon) are fully documented and studied in this experiment.

1.3 Fast Ion Transport Project at UC Irvine

The fast ion transport project at UC Irvine started from September 2004. The project is supported by the Department of Energy (DOE) and has been renewed two times. Funded at $100k per year, the project aims to study a variety of aspects of the fast ion transport in the Large Plasma Device, including classical transport, transport by electrostatic waves (e. g. drift waves) and electromagnetic waves (e. g. Alfvén waves). Two Ph. D. students have graduated in this project: Dr. Liangji Zhao (2003-2005) has worked on the classical fast ion transport during the low-density afterglow plasmas in the LAPD. Dr. Yang Zhang (2004-2008) has worked on the fast-ion resonance with shear Alfvén waves and the spectral gap of shear Alfvén waves in a periodic array of magnetic mirrors. This thesis work (2007-2011) mainly focuses on the transport of the fast ions and thermal plasmas in low-frequency,

electrostatic microturbulence. The next phase of this project will study the nonlinear interaction between fast ions and broadband Alfvén waves.

In this thesis work, we have extensively studied the interaction between the fast ion test-particle beam and the electrostatic microturbulence with various characteristics, with two physics paper published[46-47]. We have also studied the thermal plasma confinement and cross-field transport under the effect of a variety of electrostatic waves (such as drift wave, interchange mode and Kelvin-Helmholtz instability), with one physics paper published[48]. We have designed and implemented a new fast-ion detector probe, aiming to increase the bandwidth of the collected signal and accurately measure the energy of the fast ion beam. We closely collaborate with research teams from the Basic Plasma Science Facility at UCLA, and the École Polytechnique Fédérale de Lausanne (EPFL). We have presented papers at various domestic and international conferences.

1.3.1 Classical Transport of Fast Ions in Plasmas

Classical fast-ion transport during the afterglow of the LAPD was investigated[28] (Dr. Liangji Zhao, 2003-2005). A 3-cm diameter RF ion gun launched a pulsed, ~300 eV ribbon shaped argon ion beam parallel to or at 15 degrees to the magnetic field in the LAPD. The parallel energy of the beam was measured by a two-grid energy analyzer at two axial locations (z = 0.32 m and z = 6.4 m) from the ion gun in the LAPD. To measure cross-field transport, the beam was launched at 15 degrees to the magnetic field. To avoid geometrical spreading, the radial beam profile measurements were performed at different axial locations where the ion beam was periodically focused. The measured cross-field transport is in agreement to within 15% with the analytical classical collision theory and the solution to the Fokker-Planck kinetic equation. Collisions with neutrals have a negligible effect on the beam transport measurement but do attenuate the beam current. The beam energy distribution measurements were calibrated by LIF (laser induced fluorescence) measurements performed in the Irvine Mirror.

1.3.2 Fast Ion Resonance with Shear-Alfvén Waves in Plasmas

The Doppler-shifted cyclotron resonance ($\omega - k_z v_z = \Omega_f$) between fast ions and shear Alfvén waves was experimentally investigated by Dr. Yang Zhang (2004-2008). A test particle beam of fast ions was launched by a Li+ source in the helium plasma of the Large Plasma Device, with shear Alfvén waves (SAW, amplitude $\delta B/B$ up to 1%) launched by a loop antenna. A collimated fast-ion energy analyzer measured the non-classical spreading of the beam, which is proportional to the resonance with the wave. A resonance spectrum is observed by launching SAWs at 0.3–0.8ω_{ci}. Both the magnitude and frequency dependence of the beam-spreading are in agreement with the theoretical prediction using a Monte Carlo Lorentz code that launches fast ions with an initial spread in real/velocity space and

random phases relative to the wave. Measured wave magnetic field data were used in the simulation.

1.4 Content of Thesis

This thesis covers two topics: fast ion transport in electrostatic turbulent waves, and thermal plasma cross-field transport in various electrostatic wave instabilities. **Chapter 2** introduces the experimental apparatus, including the LAPD, the fast-ion source and diagnostic tools, and the data analysis methods. **Chapter 3** discusses the energy scaling of the fast ion beam cross-field transport in large amplitude drift-wave turbulence with linear geometry. **Chapter 4** discusses the dependence of the fast ion transport on the nature of the turbulence. A variety of background turbulent waves with different spatial-temporal scales are driven, and the fast-ion beam diffusions in these waves are extensively explored. **Chapter 5** discusses sheared-flow induced thermal plasma confinement transition in LAPD. A conclusion to this thesis work and future work in the next phase of the fast-ion project is stated in **Chapter 6**.

Chapter 2
EXPERIMENTAL APPARATUS

2.1 Basic Plasma Science Facility at UCLA: The Upgraded LAPD

Commenced in August 2001, the Basic Plasma Science Facility (BaPSF) at the University of California, Los Angeles serves to perform frontier-level experiments in plasma physics and technology. The upgraded Large Plasma Device[24] (LAPD) that forms the core of the facility provides a broad range of plasma conditions for experiments on outstanding problems on the behavior of plasmas. The LAPD (Fig. 2.1) has a 20-m-long, 1-m-diameter cylindrical vacuum chamber, coaxial with 56 solenoid magnetic field coils. The magnetic coils can provide an axial magnetic field (B_z) of up to 3.5 kilogauss (steady state), directing towards the plasma source (South). The axial magnetic field used in this thesis work ranges from 600 gauss to 1800 gauss. The LAPD is mounted with 450 radial ports, allowing a nearly 360-degrees view of the plasmas along the machine length. Most of the ports are conventional KF-NW40 and KF-NW50 circular ports, which are suitable for diagnostic probes and other small devices. Rectangular ports (octo-ports) with $4.25" \times 12.75"$ (width × height) outlet are available on both the west side and the top of the LAPD at Port 7,13,19,24,30,35,41 and 47. These rectangular ports are designed for large ion sources and other large devices (e. g., radial-frequency (RF) antennas and obstacles, see descriptions in Sec. 2.3).

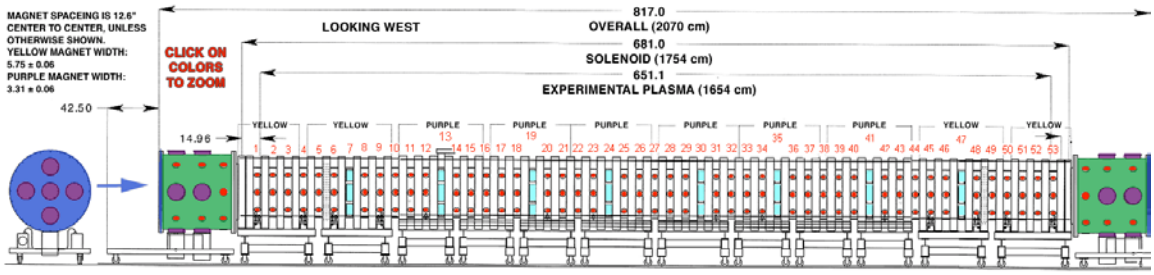

FIG. 2.1 Schematic of the upgraded Large Plasma Device, with port numbers labeled. Rectangular ports are mounted on both the west side and the top of the LAPD at Port 7,13,19,24,30,35,41 and 47. Typical sections used in the current experiments are between Port 30 and Port 35. The fast-ion source is usually mounted on the west side of Port 35.

Pulsed plasmas with ~10 ms duration are created using a barium oxide coated cathode source with a molybdenum mesh anode placed 0.55m away from the cathode. A 4-Farad capacitor bank is connected between the cathode and the anode to supply a total discharge current of up to 32kA. During the pulsed-discharge time, fast electrons with energy of ~50eV are created. These electrons flow along the axial magnetic field line through the

gridded anode and ionize the working gas in the main chamber to form a plasma column. The uniform plasma column has a maximum length of 18 meters and a diameter up to 75cm. The plasma length and the density profile perpendicular to the magnetic fields can be tailored to study various plasma behaviors that depend on the axial or radial gradient in density, temperature and potential.

2.2 Diagnostic Tools in LAPD

The fast-ion project benefits from the professional and supportive scientific research team of the Basic Plasma Science Facility at UCLA. State-of-the-art plasma diagnostic tools are available and set up for these experiments. Conventional plasma diagnostic tools used for this thesis project study includes: triple and swept Langmuir probes, Gundestrup (Mach) probes, B-dot probes, high-speed camera imaging, and interferometers.

2.2.1 Triple and Swept Langmuir Probe

Langmuir probes with signal, double or triple electrodes are widely used for basic plasma diagnostics. The triple Langmuir probe[49] is commonly used for measurement of plasma density (n_e), temperature (T_e), floating potential (V_f) and their fluctuations with good time resolution. A typical circuit for the triple probe used in LAPD is shown in Figure 2.2. A 65V bias is applied between two electrodes. The negative electrode (with potential V_i) collects ion saturation current (I_{sat}), while the positive electrode collects an electron current with amplitude equal to I_{sat}. The third electrode is floating to measure the floating potential (V_f).

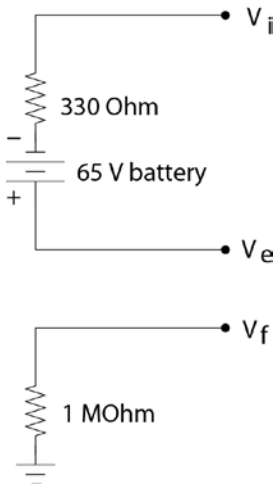

FIG. 2.2 Typical circuit setup for a conventional triple Langmuir probe used in the LAPD.

The plasma density and electron temperature can be calculated by:

$$T_e = (V_e - V_f)/\ln 2\,;\; n_e = I_{sat}/(A_{eff} e\sqrt{k_B T_e / M_i}) \qquad (2.1)$$

where V_e is the potential measured at the positive electrode, A_{eff} is the effective collection area of the electrode. Note that the triple-probe theory is based on the assumption that the electron population in the probe area is in thermodynamic equilibrium with a distribution that obeys the Boltzmann relation ($n_1/n_0 \sim e\phi_1/kT_e$). In LAPD, the electron distribution includes the thermal plasma electrons, and a high-energy tail of the ionizing electrons (with energy of ~50eV) generated from the cathode-anode discharge. So the proportionality between V_f and the plasma potential, as well as the T_e measurement, is questionable when the energetic electron population is presented.

Another common setup for the Langmuir probe is to apply a sweeping bias voltage on a single-electrode probe. By analyzing the I-V trace between the applied bias and the collected current[50], equilibrium values of the plasma density, potential and electron temperature can be derived. The swept setup directly measures the plasma potential V_p, and more accurately measures T_e and n_e. However, the fluctuations of these physics quantities cannot be measured using this setup. Thus in most data reported in this thesis work, both triple-probe measurement and swept-probe measurement are made and compared to describe the plasma conditions more accurately.

A third setup employs two Langmuir probes to measure the electrostatic wave structures of the density and potential fluctuations in LAPD. A reference probe is placed at the area with the largest density or potential fluctuation amplitude, while a second moving probe is placed a certain axial distance away from the reference probe. The moving probe scans the plane perpendicular to the magnetic field, with the reference probe signal recorded simultaneously. By analyzing the spatial-temporal correlation between the signals from the moving probe and from the reference probe, information about the wave structure size, correlation length and mode numbers are obtained (see Chapter 2.4.2 for detail).

2.2.2 Gundestrup (Mach) Probe

A Gundestrup (Mach) probe[51-53] with six faces is available to measure plasma flows. The Mach probe design is based on the model of the plasma density distribution near a Langmuir probe with background plasma flow. An empirical relation between the collected flux and the plasma flow velocity for a simple 2-faces Mach probe is

$$\frac{\Gamma_{up}}{\Gamma_{down}} = \exp(Kv_f), \qquad (2.2)$$

where Γ_{up} and Γ_{down} are the upstream and downstream ion flux (proportional to I_{sat} signal), v_f is the flow velocity and K is an empirical calibration factor (with a typical value of ~1.3 for $T_i \leq 3T_e$). Practically, probes with multiple faces are used for more accurate flow measurement.

2.3 Irvine Fast-Ion Source and Detectors

2.3.1 Thermionic Lithium Aluminosilicate Ion Source

The ion beam source[27] currently used for all experimental studies reported in this thesis work is a thermionic emitter filled with lithium compound. The emitter is heated by a wound coil of molybdenum wire solidly potted into the emitter body cavity with high purity Al_2O_3. The emission current increases with the total heating power applied on the heater. A typical heater current is 11A and typical voltage is 7V, leading to a total heating power of ~80W and emission current density of $\sim 100 \mu A/cm^2$. The fast ion energy is set by applying an external bias on the body of the emitter, which forms a potential difference between the emitter and the molybdenum grid (usually grounded to the LAPD chamber wall) at the aperture of the ion gun. An additional grid is placed between the aperture and the emitter and usually biased to -90V. This grid does not modify the final ion beam energy, however, it forms accelerate-decelerate electric fields and increases the total emission current. The shaft of the ion gun is cooled by high-pressure air to prevent over-heating of the electric connections between the heater leg and the power supply. An additional orifice with outlet diameter of ~5mm is placed before the 0.6" aperture of the ion gun to accurately control the width of the ion beam. The lithium ion emitter typically has an operating lifetime of ≥20 hours with heating power ≤80W, while higher heating power will not only increase the emission current but also deplete the emitter rapidly. The lithium ion source fits into the rectangular ports in LAPD and is usually operated with a pitch angle to produce an ion beam with a helical trajectory. The estimated angular divergence[54] of the beam is ~3° and the energy divergence is <4%.

2.3.2 Retarding-Field Fast-ion Detector

Development of diagnostic probes for analyzing the fast ion beam signal is essential and challenging. The ultimate goal of the fast-ion analyzer probe is to accurately measure the spatial and energy distribution of the fast-ion test beam population. The most direct and practical method to measure the fast-ion signal is to collect the fast ions using a conducting collector. A gridded fast-ion analyzer probe has been designed and successfully used in several previous experiments (and also widely used in the experiments reported in this thesis work). This probe features a collimated design, which aims to collect the fast-ion beam with the same pitch angle (to the axial magnetic fields) as the analyzer. And two Molybdenum grids are mounted in front of the copper collector-disk. The grids can be biased positively or negatively to repel the thermal ions and electrons, which improves the signal-to-noise level for the collected signal. However, this fast-ion analyzer probe has several limitations:

(1) The fast-ion current signal collected is $\sim 10nA$. A 1MΩ resistor is used to convert the current signal to voltage for the data acquisition system (DAQ). Signals are further

amplified by a Lecroy DA1822A differential amplifier. The total capacitance of the coaxial signal line is ~300pF, which leads to a frequency limit of the signal of ~500Hz. ($\omega_{3DB} = 1/RC = 3.33\text{kHz}$). Signals with higher frequencies are filtered out. In experimental studies of the fast-ion interaction with the shear Alfvén waves, the Alfvén wave frequencies are ~500kHz, thus a probe design capable of collecting signals with higher bandwidth is desired.

(2) The angular acceptance of the fast-ion analyzer is limited by the geometry of the grids, the collector disk and the spacing between them. The current version of the analyzer has a limited acceptance angle of $\sim \pm 15^{\circ}$. This collimated design helps discriminate fast-ion beam signals from thermal plasma currents. However, the pitch-angle profiles of the fast-ion beam are modified by wave-particle interaction and by classical Coulomb collision. A probe design with wider acceptance angle serves better in studying the wave-induced velocity-space diffusion of the fast ions.

(3) The analyzer probe works well in fast-ion beam signal collection, however, with no energy resolution. The design of the retarding grids does not serve the purpose of portraying the energy distribution of the fast-ion population. The two grids in this probe are typically biased to ~-9V and ~+50V in order to repel thermal electrons and ions, while a bias voltage comparable to the fast ion energy (~300-1000V) are required to study the beam energy distribution. New design of the retarding grid is needed.

A new design of the fast-ion analyzer has been made and tested, with its schematics and photos shown in Fig. 2.3. The analyzer head is a cylinder with a dimension of 0.97"×0.63", which fits into conventional KF40 flanges and ports (with I. D. ~40mm~1.57") at LAPD. The analyzer head is mounted on a stainless steel probe shaft with 95mm O. D., and electrically isolated with the shaft by Teflon. The inner structure of the analyzer features a cylindrical focusing electrode, two flat single-layer grids, two copper disks (serves as a collector and a dummy). The electrodes and grids are isolated from the analyzer housing by boron nitride. Boron nitride provides good electrical isolation, and has a very small thermal expansion coefficient, which is suitable for use in the LAPD.

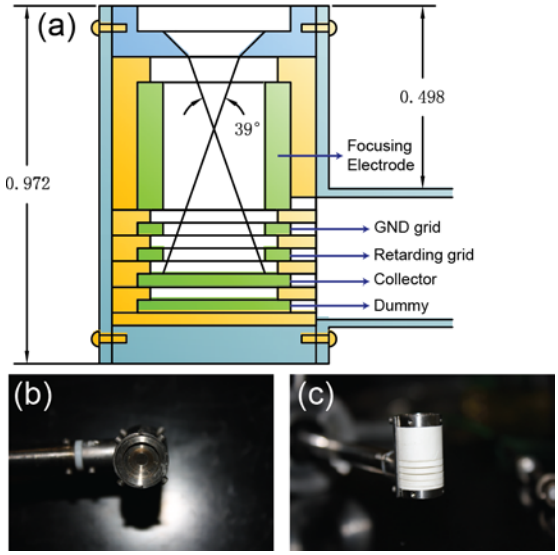

FIG. 2.3 Schematic (a) and photos (b-c) of the new fast-ion collector design (dimensions in inch). The design is in cylindrical geometry. The materials used are stainless steel (blue), boron nitride (yellow) and molybdenum (green).

The purpose of the focusing electrode is to convert a divergent fast-ion population into a quasi-parallel beam, and the retarding grid provides a planar retarding field for discriminating the energy of the collected fast ions. The combination of the focusing electrode and the retarding grid allows analysis of the beam particle total kinetic energy distribution with improved energy resolution. The collector-dummy set are used to cancel the RF pickup noise signal collected from the plasma fluctuations and other noise sources, with the differential signal between the collector and the dummy recorded. Similar designs of such retarding-field energy analyzer can be found in Ref. [55] and references therein.

The new design is modeled and simulated before manufacture. The static electric fields in the analyzer housing are modeled using COMSOL. To model the effects of the focusing electrode, the bias on the electrode is set to be 600V, which matches the typical fast-ion energy (~600eV) in the study. Then the electric fields are imported into a particle tracing code to study the fast ion trajectories with various injection angles and energies. Figure 2.4 shows the static potential and electric fields inside the analyzer housing, simulated by COMSOL. The electric fields applied by the hollow-cylindrical electrode are focusing towards the axis of the cylinder. Lithium ions with pitch angle ranges from -45° to 45° (relative to the axial direction of the analyzer) are followed, with their trajectories under the electric fields calculated.

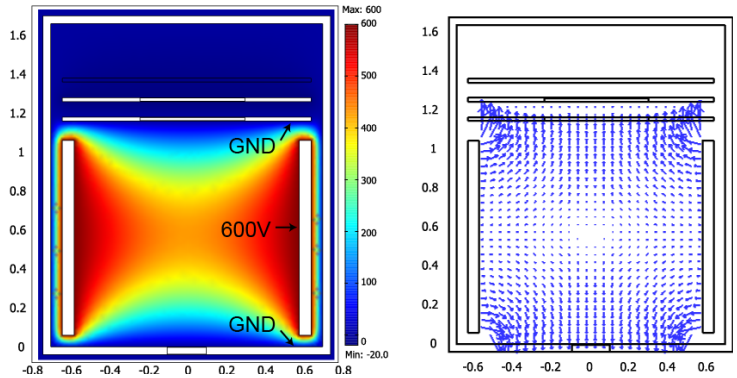

FIG. 2.4 Calculated potential contours (left) and electric fields (right) inside the analyzer housing with the focusing electrode biased to 600V.

Injection ions with different energies (400eV-1000eV) are calculated (Fig. 2.5) to study the energy-dependence of the focusing effect on the divergent beam. The focusing effect is optimized when the injection ion energy is the same as the bias on the focusing electrode.

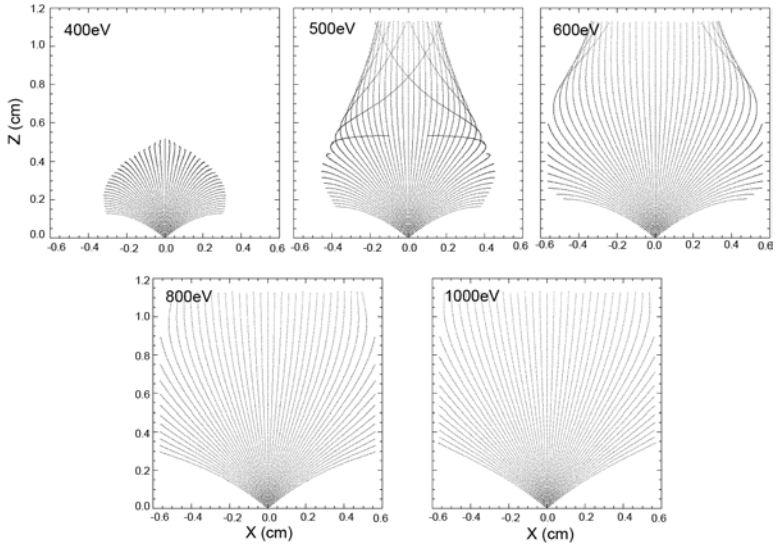

FIG. 2.5 Fast-ion trajectories with various energies and pitch angles inside the fast-ion analyzer, with the focusing electrode biased to 600V. The focusing effect is optimized when the collected fast-ion energy matches the bias on the focusing electrode.

Ions with a pitch angle of -20°-20° are deflected to quasi-parallel to the axial direction, for which their total energy can be accurately measured by a planar retarding field. Ions with lower energy than the electrode bias are over-focused or reflected, while ions with higher energy are under-focused. The effect of the finite inlet aperture size of the analyzer on the final beam energy resolution is also simulated (Fig. 2.6). Ion beams with different pitch angles (0°, 5°, 10°, 20°) and a finite width (~1.5mm) are simulated. The average energy of the ions along the axial direction is calculated, since a planar retarding field can only

discriminate ion energy perpendicular to the equal potential line. Ion beam axial energy (E_z) decreases with larger injection angle, indicating that the energy resolution is lowered.

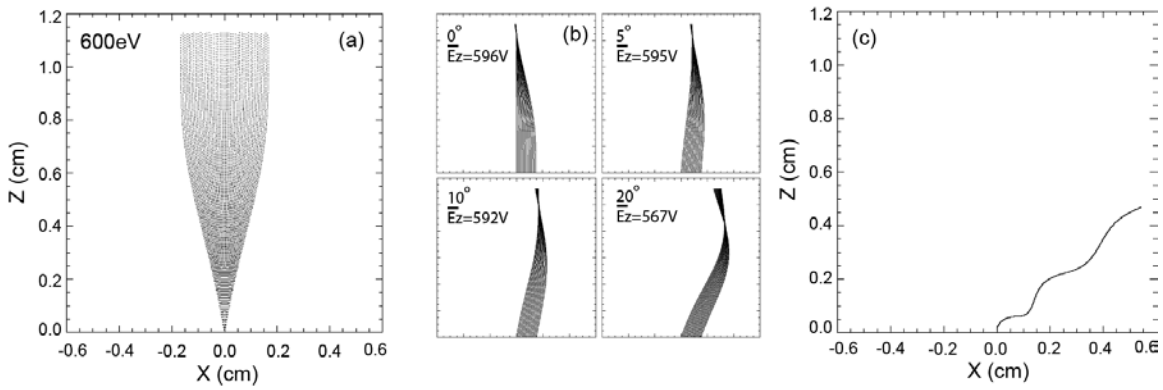

FIG. 2.6 (a) Fast-ion trajectories with energy of 600eV and -10°-10° pitch angels. (b) The average perpendicular energy of the fast ion beam with a width of 1.5mm and various injection pitch angle. (c) Trajectory of a 100eV electron with 0° initial pitch angle.

A 10° injection angle leads to an error ($\delta E/E$) in the energy measurement of ~1%. The error is ~5% for 20° injection angle, which indicates that the beam is over-focused in this case. The electron behavior inside the analyzer is also examined. Trajectories of electrons with energy of 100eV and pitch angle of 0° are simulated. Electron trajectories show that the focusing electrode collects the thermal electron population, preventing them from reaching the collector-disk. The simulation results suggest that the design of the fast-ion analyzer with a focusing electrode and a retarding grid can accurately measure the energy of the fast ion with a pitch angle of -10°-10°, while the thermal plasma ions and electrons are either repelled or collected before reaching the collector-disk.

The new analyzer design was tested in vacuum with no plasma presented. Figure 2.7 shows typical curves of the collected current signal with sweeping bias on the retarding grid, with the fast ion source placed ~30cm away from the collector, with 0° and 10° injection angle.

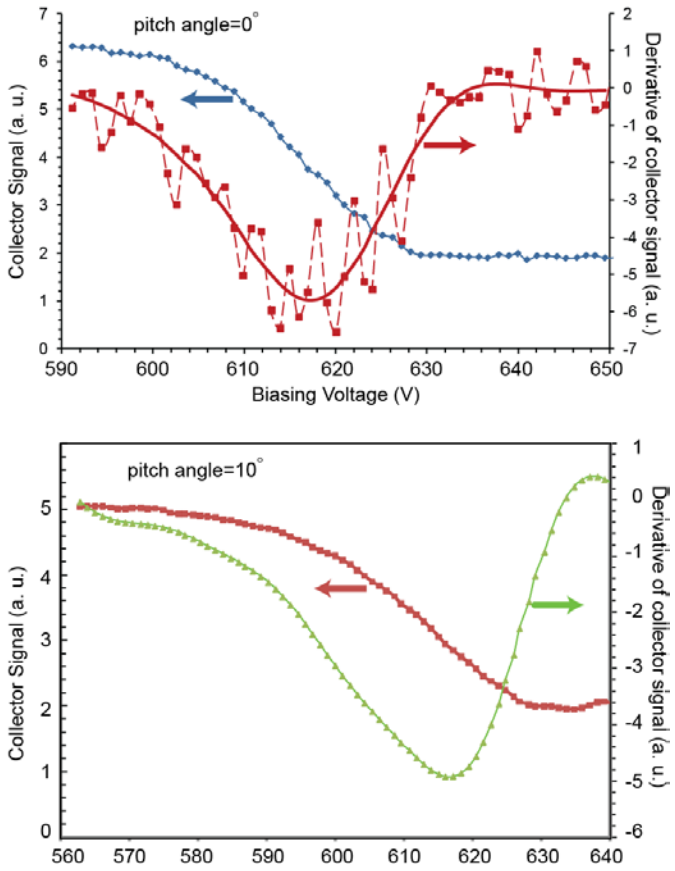

FIG. 2.7 Collected fast ion current signal with swept bias on the retarding grid. The fast-ion energy is set to be 600eV. Two injection pitch angles (0°, 10°) are tested.

The derivative of the collector signal shows the energy distribution of the fast-ion population. The energy distribution function typically has full-width at half-maximum of ~20eV. With no focusing electrode, it is expected that the measured fast ion energy for 600eV fast ion beam with 10° injection angle is 580eV, while with 0° injection angle is 600eV. However, Fig. 2.7 shows that with both 0° and 10° injection angle, the fast ion population peaks at 615eV, which indicates that the fast-ion beam is focused and the total energy is measured.

The performance of the energy analyzer tested at the LAPD is degraded. In the active discharge of the LAPD, the signal to noise level of the probe is much lower than that in vacuum. And due to the Debye shielding effect of the high thermal plasma density, the front grids and electrodes can not efficiently deflect thermal ions and electrons. Micro-arcing between the retarding grid and the collector happens when the bias voltage is high (~600eV), which adds additional noise to the collected signal. Figure 2.8 shows a response of the collector signal to the bias voltage of the retarding gird for a ~600eV beam. The slope of the signal is located at ~750V, which deviates from the actual fast-ion energy. The error in the energy measurement might be due to the Debye shielding on the retarding grid, or

disruption of the equipotential lines in the analyzer due to static charges built up. More testing and development of the energy analyzer are needed.

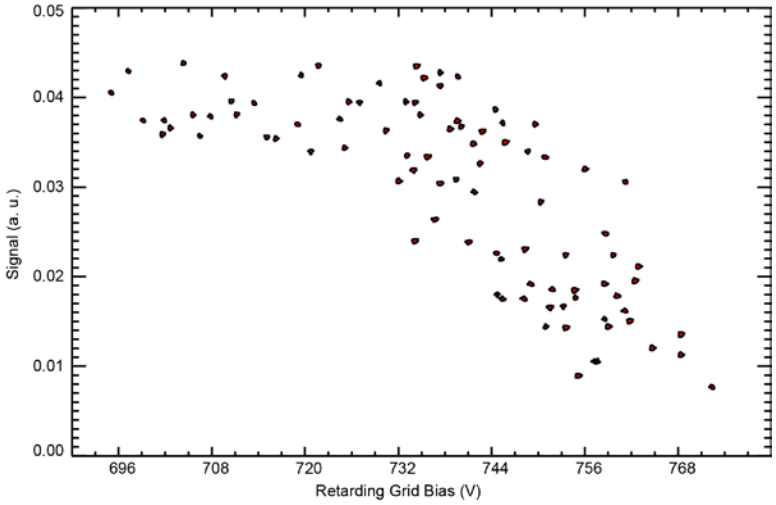

FIG. 2.8 The collector signal of a ~600eV beam versus bias voltage of the retarding grid. The test is performed with the retarding field energy analyzer in the LAPD helium plasmas.

Another direction of upgrading the probe for fast-ion diagnostics is to increase the time response of the probe. As discussed before, the time resolution of the current analyzer is limited by the 1MΩ resistor used for signal collection, which is necessary for the small collector current signal (~10nA). However, it also limits the time response of the probe by the RC time of the circuit. An alternative method for data collection is to use a relatively small load resistor (~1kΩ) and a pre-amplification circuit very near the analyzer head. This setup reduces both the capacitance and resistance of the signal collection circuit and improves the time response of the signal. A schematic of the pre-amplification circuit is shown in Fig. 2.9, with a high-speed differential receiver amplifier chip (AD 8129) used.

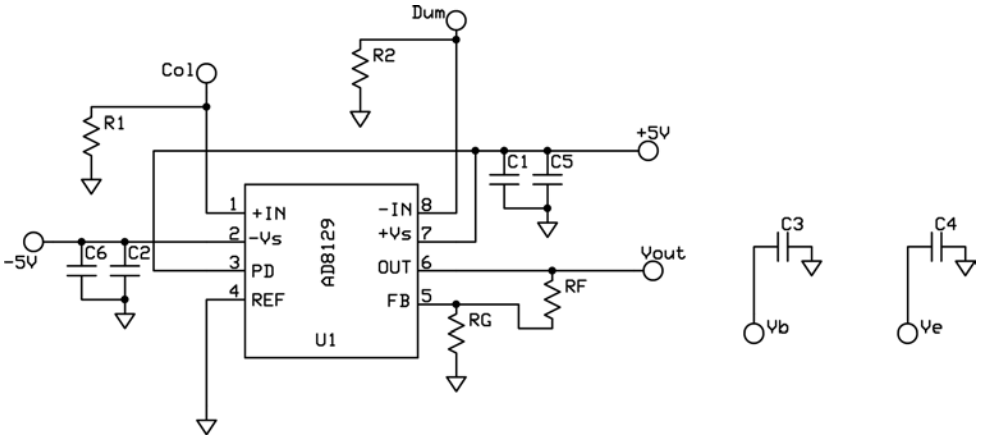

FIG. 2.9 Schematic of the amplifier circuit. C1=C2=0.1μF; C3=C4=C5=C6=10μF; R1=R2=1kΩ; R_F=2kΩ; R_G=20Ω; Gain=1+R_F/R_G≅100.

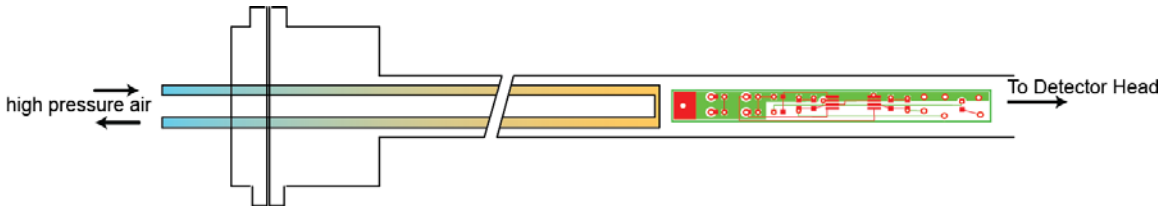

FIG. 2.10 Schematic of the amplifier circuit board and associated high-pressure air cooling inside the probe shaft.

However, operated in the LAPD chamber, the probe is under the blackbody radiation from the hot-cathode (≥1500K). The heat accumulation, depending on the distance from the cathode, can raise the surface temperature of the probe up to several hundred degrees (℃), in which the pre-amplification circuit fails to work. Thus internal cooling on the circuit board inside the probe shaft is necessary. Figure 2.10 shows the schematics of the PCB circuit board and the internal cooling tube inside the probe shaft. The U-shape copper tube with 3mm O. D. is sealed from vacuum by o-rings. High-pressure air circulates inside the tube to remove the heat residual on the PCB board. The probe with pre-amplification circuit is already tested in vacuum, and requires further testing and adjustment in the LAPD environment.

2.4 Data Analysis Methods

Analyzing the collected fast-ion signal and the plasma diagnostic data is a very important part of this thesis work. IDL based codes are used to read and process the large volume diagnostic data collected during the experimental runs. The analysis on the fast ion signals mainly includes statistical averaging and functional fitting. The plasma fluctuations are analyzed using different methods, mostly in the frequency domain to reveal different aspects of the turbulent wave characteristics. For example, the correlation length and the mode numbers of the turbulent waves are derived from cross-correlation analysis; bi-spectrum analysis is used to explore nonlinear coupling of the different wave modes. Several important aspects of the data analysis methods are introduced in detail in this section.

2.4.1 Beam profile analysis

The collected fast-ion beam data from the data acquisition (DAQ) system are voltage signals. The collected fast ion current is measured through a 1MΩ load resistor and further amplified by a Lecroy DA1822A differential amplifier (usually ×10). A special synchronization between the lithium source and the LAPD plasma is employed, so that the ~ 20 ms fast-ion pulse is turned on and off every two plasma discharges, with an adjustable delay and duration. The background signal is taken when the source is disabled for one

shot right after the previous beam-on shot. Even number of shots is repeated at one spatial location before the probe drive moves on. The signals with the source off are subtracted from the signals with the source on. The fast-ion signals shown in this work are net signals with background subtractions.

A typical beam profile is shown in Fig. 2.11 where the collected beam spot size is compared to the transverse orbit size.

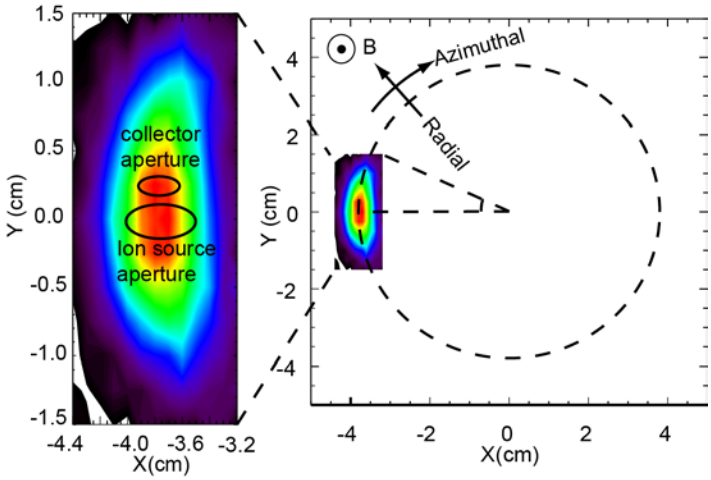

FIG. 2.11 (Right) Projection of the fast ion orbit onto the horizontal plane, with the beam profile measured 3 ports from the source overlaid. (Left). Detail of the beam profile, together with the projection of the ion source and collector apertures.

The aperture size of the ion gun is 0.5cm, which is the initial width of the beam. The analyzer has an aperture of 0.3cm. To obtain an accurate quantitative measurement of fast ion diffusion, the 2D beam signal array from the collector is analyzed to yield the radial and azimuthal profile separately.

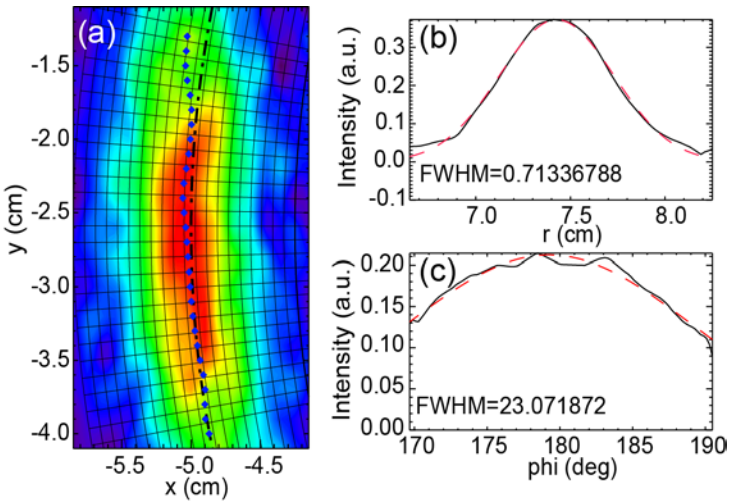

FIG. 2.12 A typical collected beam profile and data analysis process. (a) Contour of the signal amplitude. Dotted line: fitted gyro-orbit. Solid line: mesh imposed to calculate the beam FWHM. (b) Beam radial profile and its gauss fit. (c) Beam azimuthal profile and its gauss fit.

Figure 2.12 demonstrates a typical analysis of the beam profile. First, the beam trajectory is fitted into the observed contour plot with its gyroradius [dashed line in Fig. 2.12(a)], using Gaussian centers of all the row profiles along the x direction (blue diamonds). Then a fine grid along the fitting orbit is developed (solid lines) and the beam profile is projected onto the grid. The weight of each radial and azimuthal profile along the new grid is calculated by the χ^2 goodness of its Gaussian fits. By averaging over all radial and azimuthal profiles, the weighted average radial profile and azimuthal profile are obtained. Finally, a Gaussian fit is performed on the averaged profile to obtain its full width at half maximum (FWHM) [Fig. 2.12(b, c)].

The finite angular acceptance of the collector ($\pm$15°) affects the profiles in the azimuthal direction but not in the radial direction. To estimate the cut-off effect by the finite angular acceptance of the collector, the profile for one experimental condition was measured again with an analyzer that accepts incident ions from a broader range of angles. With this analyzer, the azimuthal profile is longer but the radial profile is unaffected, confirming that the radial profiles accurately represent the actual beam width. In this thesis work, only the radial profiles of the beam spots are used to quantify the diffusion of the fast-ions.

2.4.2 Cross-correlation analysis

Cross-correlation and cross-spectrum are powerful tools to reveal the wave characteristics of the plasma fluctuations. The setup for correlation diagnostics with two Langmuir probes are described in Sec. 2.2.1. Figure 2.13 illustrates the mechanism of this diagnostics. The fixed probe and the moving probe are separated axially by a distance, and the plasma density, potential and electron temperature signals from the two probes are collected simultaneously. If a wave structure with finite parallel and perpendicular wavelength exists

in the plasma fluctuations, from the cross-coherency and cross-phase between the two signals, information about the wavelength and correlation length can be obtained.

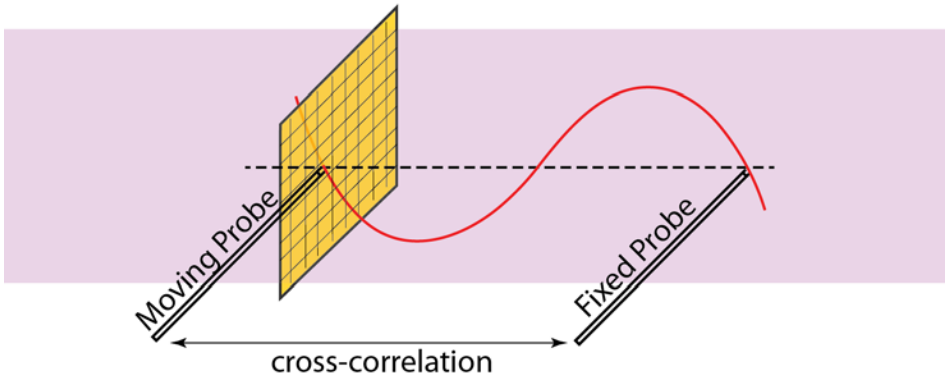

FIG. 2.13 Schematic of the two-Langmuir-probe setup for cross-correlation analysis.

Assuming $f_1(\omega, x, y)$ and $f_2(\omega, x, y)$ are the signal's fast Fourier transform (FFT) spectrum collected from the fixed probe and the moving probe, the cross spectrum between the two signals is:

$$S_{xspec}(\omega,x,y) = f_1(\omega,x,y)\cdot f_2^*(\omega,x,y) \qquad (2.3)$$

The cross-coherency can be calculated by:

$$\langle \gamma^2 \rangle = \frac{\langle S_{xspec}(\omega)\cdot S_{xspec}^*(\omega)\rangle}{(f_1(\omega)\cdot f_1^*(\omega))(f_2(\omega)\cdot f_2^*(\omega))}, \qquad (2.4)$$

with cross-phase:

$$\theta_x = \tan^{-1}\left(\frac{\mathrm{Im}(S_{xspec}(\omega))}{\mathrm{Re}(S_{xspec}(\omega))}\right). \qquad (2.5)$$

The power of the fluctuations can be obtained by

$$S_1(\omega,x,y) = f_1(\omega,x,y)\cdot f_1^*(\omega,x,y) \qquad (2.6)$$

Same method can be used to calculate the phase shift between plasma density (n_e) and potential (ϕ) from a triple Langmuir probe, which is very important to identify the nature of the wave modes:

$$\theta_{n,\phi} = \tan^{-1}\left(\frac{\mathrm{Im}(S_{n,\phi}(\omega))}{\mathrm{Re}(S_{n,\phi}(\omega))}\right). \qquad (2.7)$$

In Chapter 3-5, the cross-correlation analysis is the major tool to quantify the structures and mode numbers of the edge turbulent waves driven by gradients in both plasma density

and potential. Typical spatial contours of the cross-correlation functions can be found in Fig. 4.3(a) - 4.6(a). In most cases analyzed in this thesis work, the typical parallel wavelength of the edge turbulent waves studied is comparable to the LAPD machine size (~20 meters), and is much longer than the perpendicular wavelength (~ several centimeters) of the wave. Thus the cross-correlation function mainly indicates the 2D mode structures perpendicular to the ambient magnetic field.

2.4.3 Bispectral analysis

Bispectral analysis[56-57] is a higher order statistical technique which is useful to study systems that contain a quadratic nonlinearity. In this thesis work, three-wave nonlinear interaction in plasma turbulence is explored using FFT based bispectral analysis. The autobispectrum is defined as an ensemble average,

$$B(k_1,k_2)=\left\langle \phi(k_1)\phi(k_2)\phi^*(k_3)\right\rangle \qquad (2.8)$$

Where k_1, k_2 and k_3 are the wave numbers of three modes which obey the three-wave interaction criteria of conservation of momentum, and $\phi(k)$ is the Fourier transform of a data signal in k space. The squared autobicoherence is defined as

$$b^2(k_1,k_2)=\frac{\left|B(k_1,k_2)\right|^2}{\left\langle\left|\phi(k_1)\phi(k_2)\right|^2\right\rangle\left\langle\left|\phi(k_3)\right|^2\right\rangle}. \qquad (2.9)$$

The squared autobicoherence value is $\in[0,1]$, and is a quantitative measure of the amount of three-wave coupling.

Chapter 3
TURBULENT TRANSPORT OF FAST IONS IN ELECTROSTATIC WAVES WITH LINEAR GEOMETRY

3.1. EXPERIMENTAL SETUP

3.1.1 Overview

The experiment is performed in the Large Plasma Device (LAPD)[24] at UCLA. The axial magnetic field is uniform with $B_z \sim 1.2\text{kG}$. Typical parameters of the LAPD plasma during the discharge are $n_e \sim 2.0\times10^{12}\text{cm}^{-3}$, $T_e \sim 5\text{eV}$, $T_i \sim 1\text{eV}$. The line-integrated plasma density is measured by an interferometer. A triple Langmuir probe[49] is used to measure the spatial profile of the plasma density, temperature, floating potential and their fluctuations. The experimental setup and the typical fast ion trajectory are shown schematically in Fig. 3.1.

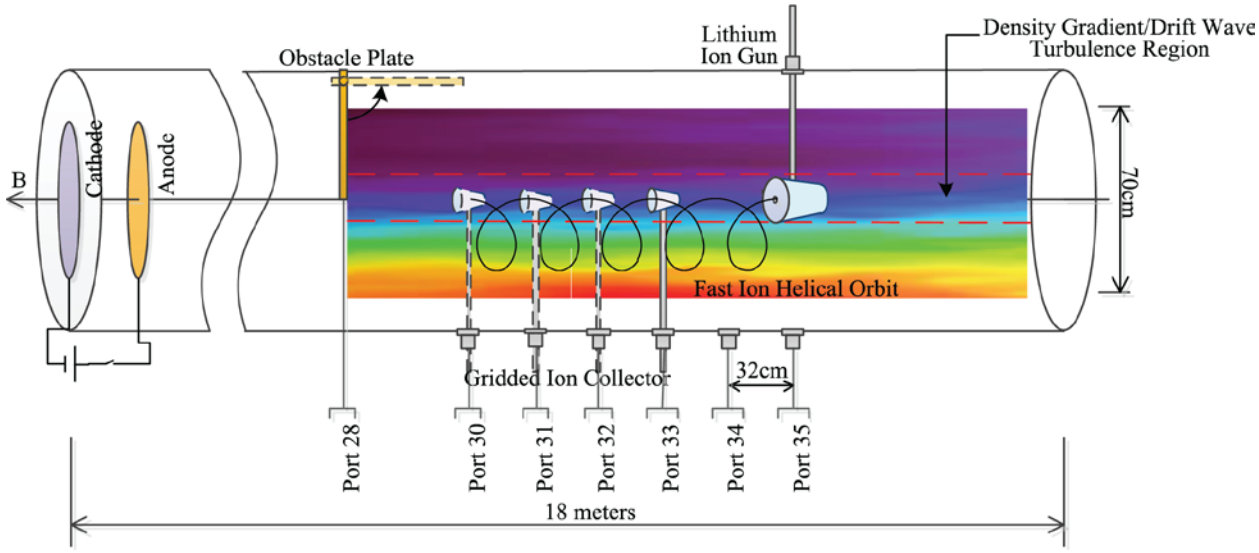

FIG. 3.1 Experimental setup in the LAPD. Fast ions interact with drift wave turbulence in the region between the two dash lines. The probe is inserted at different ports each time to study the spatial dependence of transport. The ion source and analyzer are axially aligned. The contour shows a typical density profile when plate-obstacle is deployed.

A rotatable, floating copper plate obstacle blocks half of the plasma column. (The plate can rotate out of the column to create a quiet reference condition.) A steep density gradient, along with large density fluctuations ($\delta n/n \sim 1$), is observed at the edge region in the shadow of the plate. Figure 3.2 shows the spatial profile of the density (n_e) and density fluctuation level (characterized by the standard deviation of the density) behind the plate

during the ~10 ms discharge time, where the plate edge is at x=0. The density gradient has a transverse scale length of ~5 cm (the background ion sound radius $\rho_s \sim 0.6\text{cm}$ and the ion gyro radius $\rho_i \sim 0.24\text{cm}$).

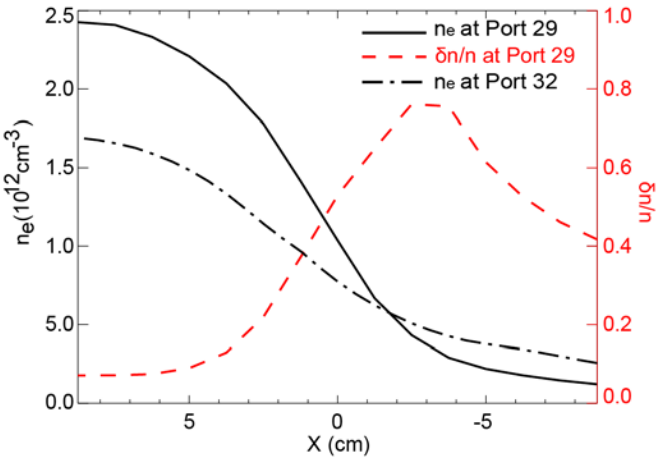

FIG. 3.2 Horizontal profiles of density at two different axial positions (solid and dash-dot lines) and of density fluctuations (dashed line), averaged between 2-6.5 ms in the active discharge. The edge of the plate-obstacle is at x=0, and the ionizing fast electrons are blocked in the x>0 region .

No ionizing fast electrons from the cathode-anode discharge are present in the area behind the plate, so that no volume ionization occurs. Therefore, the observed plasma density behind the plate is due to cross-field transport.

The lithium ion source (see Chapter 2.3.1) is inserted into the LAPD plasma via a rectangular side port (Port 35). Both the shaft and housing of the source are floating to minimize the perturbation to the main plasma column. With a 5 mm exit aperture, the ion source launches a low divergence (~ ± 5 degree) Li-7 ion beam. The beam energy is controlled by the bias voltage on the emitter, ranging from 400eV up to 1keV with a fluctuation level of ±5eV. Typical beam current densities are ~300μA/cm². The fast ion source is operated at various pitch angles with respect to the magnetic field. Thus the trajectories of fast ions are helical: gyro motion perpendicular to the magnetic field and parallel motion with constant velocity v_z along the magnetic field. The fast ion parameters are carefully chosen to make

$$d_{port} / v_z = T_f, \qquad (3.1)$$

where $d_{port} = 31.95\text{cm}$ is the distance between each two diagnostic ports and T_f is the fast ion gyro period. This way, the initially slightly divergent beam is refocused at each observation point.

The collimating fast-ion analyzer (see Chapter 2.3.2) is inserted at four different locations (2-5 ports away from the source) to measure the spreading of the ion beam as a function of

distance. The fast ion analyzer is composed of a 3mm copper disk collector, an identical dummy collector (to minimize common mode noise) and two molybdenum retarding grids. It is designed to reject thermal particles electrically and geometrically. Operated at the same pitch angle as the ion source, the analyzer is collimated to the direction of the fast ion beam to maximize the beam signal. The angular acceptance of the analyzer is limited to $\pm 15°$ by its geometry. Mounted on a computer-controlled 2D probe drive system, the ion analyzer is able to scan within a perpendicular plane to precisely contour the beam profile with ±0.5mm accuracy. The fast ion current and dummy pickup signals are fed into a Lecroy DA1822A differential amplifier with 1MΩ input impedance. The bandwidth of the collected signal is limited to ~5kHz by the RC time of the transmission circuit. Synchronization of the fast ion source, the LAPD discharge pulse and the data collection system is critical for studying wave-particle interaction. To create large amplitude drift wave turbulence, the experiment was performed during the active discharge, which is the first ~10ms of each LAPD cycle. The active discharge, compared to the afterglow, has a larger plasma density ($\sim 2.5\times10^{12}$ cm^{-3}) and higher plasma temperature (T_e ~5eV, T_i ~1eV), thus is suitable for creating a large density gradient. Figure 3.3(a) shows an example of the plasma density variation during the data collection time. It should be noted that during the active discharge, the collected signal-to-noise level is much lower compared to the afterglow, due to the large background density fluctuation.

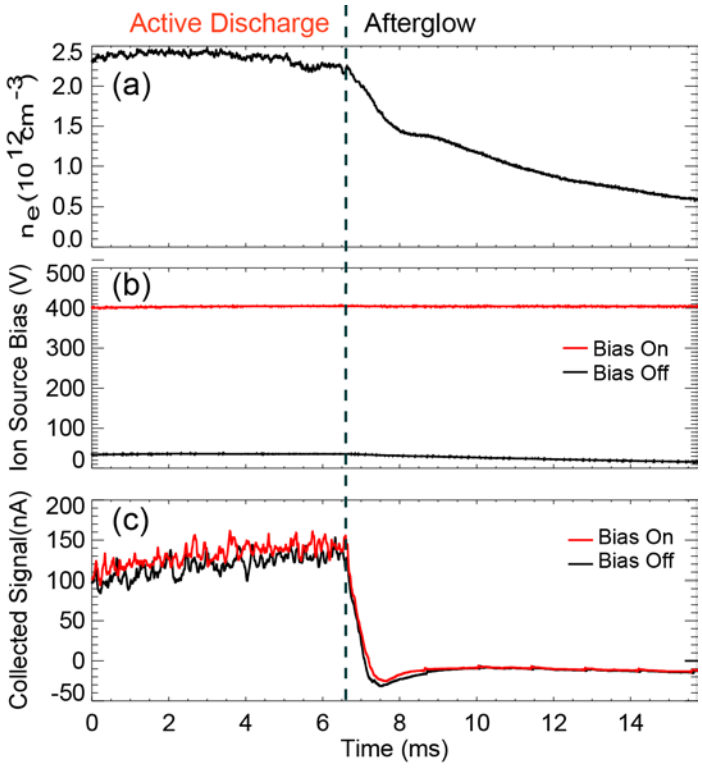

FIG. 3.3 Typical time evolution of (a) plasma density, (b) ion source operating voltage , and (c) collected signal during the data collection time window. The active discharge ends at ~6.5 ms. (a) Line-averaged plasma

density measured by the interferometer (b) Operating voltage on the ion source to launch a 400eV ion beam (c)Collected signal when the ion source operating voltage is on/off. The fast ion signal is the difference between these two. Signal collected 3 ports from the source.

To facilitate the extraction of the small beam signal from the large background plasma noise, the fast ion source is operated at half the LAPD discharge frequency by turning the ion source emitter bias on and off, and the difference between the signals is recorded. A sample emitter bias and the corresponding analyzer signal are shown in Fig. 3.3(b and c). The difference signal between bias on and off discharges yields the actual fast ion current. To further increase the signal-to-noise ratio, the signal is averaged over an even number of shots (usually 10 shots) at the same spatial location.

3.1.2 Drift wave characteristics

Drift waves associated with a steep density gradient have been studied extensively in the LAPD[25, 38]. Drift wave characteristics are diagnosed using radial inserted Langmuir probes and B-dot probes[58]. Two triple Langmuir probes, separated axially by 95.85cm, are used to analyze the parallel and perpendicular (to the magnetic field) correlation of the drift wave turbulence. The contour plot in Fig. 3.4(a) shows the transverse spatial distribution of the density turbulence amplitude. The corresponding spatially averaged fast Fourier transform (FFT) power spectrum of the fluctuations is shown in Fig. 3.4(b).

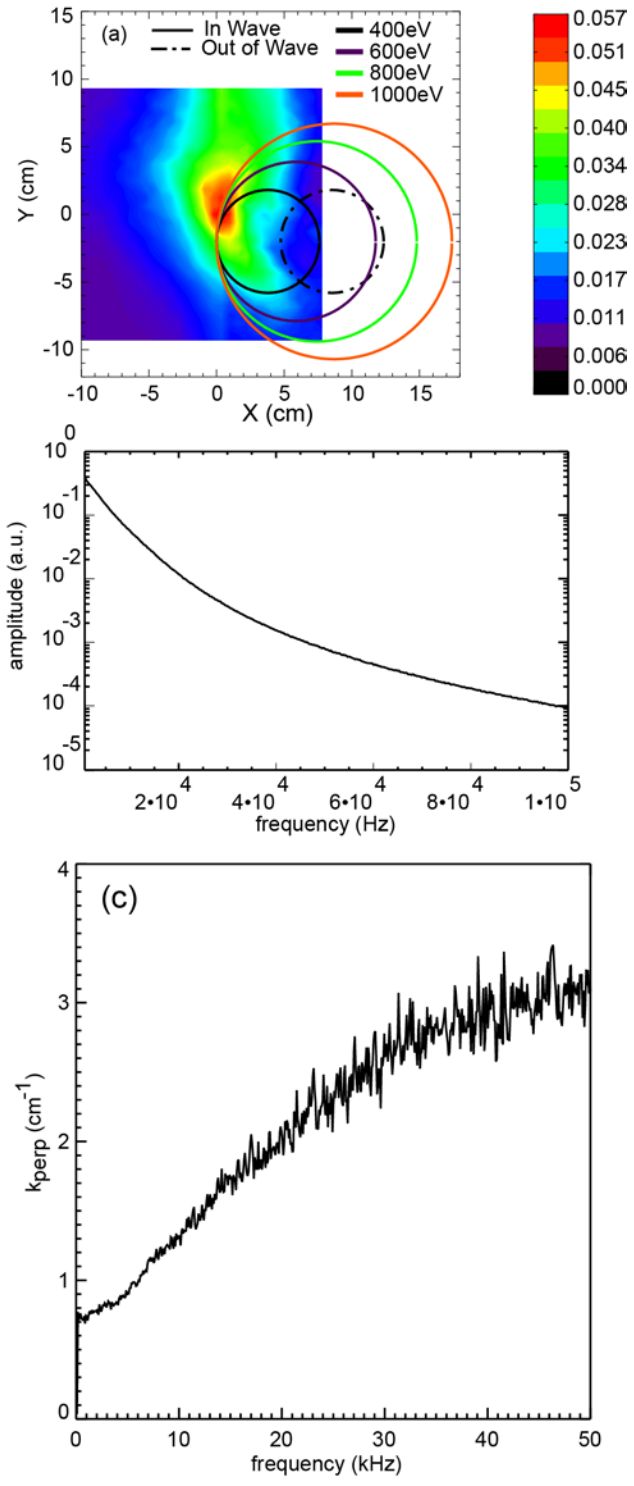

FIG. 3.4 Characteristics of drift wave turbulence created by the plate-obstacle in the FFT analysis with ~3ms time window. (a) Contour of the total power of the wave with frequency ranges 0.7~100 kHz, fast ion orbits with different energies is overlaid to show the overlap between the waves and particles. (b) Averaged fluctuation power spectrum (log-log). (c) Dispersion relation of the wave, calculated from the cross-correlation between two triple probes.

The phase velocity of the drift wave[59], can be estimated as

$$\upsilon_{De} = \frac{k_B T_e}{eB_0}\frac{n_0'}{n_0} \sim 1\times 10^3 \text{ m/s}, \qquad (3.2)$$

agrees with the slope of the measured wave dispersion relation [Fig. 3.4(c)]. Within the accuracy of axial alignment of the two triple probes separated by 95.85cm, small phase difference (~8 degree) is observed between the two signals, thus $k_{||} \cong 0$ can be assumed. *B-dot* probe measurements show a much lower level of magnetic fluctuation ($\delta B \sim 0.1\text{Gauss}$), indicating that the wave is mainly electrostatic.

Spatial alignment between the drift wave turbulence and the fast-ion orbit is crucial to optimize wave-particle interaction. The lithium ion source, the ion analyzer and the region of large turbulence amplitude are axially aligned. The fast ion orbits for different energies, projected onto Fig. 3.4(a), are carefully adjusted to make the best overlap with the turbulent wave, denoted as "in wave" (solid line). For the "in wave" case, the fast ion beam is affected by both the turbulent wave and Coulomb collisions. In order to separate the effect of the wave turbulence on beam spreading, the fast ion source is shifted horizontally by 5cm to remove the orbit from the strong turbulence region; this reference case is denoted as "out of wave" (dashed line). The Coulomb collision effect on beam spreading is comparable for both cases. Thus the difference in beam spreading is exclusively caused by the transport induced by wave turbulence. The classical Coulomb collision effect is also confirmed by recording the beam spreading with the plate-obstacle turned out of plasma.

3.2. EXPERIMENTAL RESULTS

3.2.1 Energy dependence of radial transport

Lithium 7 ion beams with four different energies (400eV, 600eV, 800eV, 1000eV) are launched and collected 3 ports (95.85cm) away to study the energy dependence of fast ion transport. By changing the pitch angle, ions with different energies are forced to have the same parallel velocity υ_z, which is determined by Eq. 3. 1; only the perpendicular energy changes. Detailed parameters for these four cases are listed in Table 1. Typical time scales listed in Table 2 show that, in this experiment, the fast ion cyclotron period is much shorter than the typical drift wave period or the correlation time of the turbulence.

Energy (eV)	$E_{\|\|}$ (eV)	E_{perp} (eV)	Pitch Angle θ (degree)	R_{gyro}(cm)
415	258	157	36.76	3.8
570	258	312	49.14	5.9
800	258	542	55.49	7.4

1000	258	742	59.55	8.7

Table 1. Parameters of the fast-ion orbits for the four conditions studied in the experiment.

Transport Related Time Scales	Time (ms)
Cyclotron period T_f	3.8e-3
Pitch angle scattering time τ_{pas}	5
Turbulence correlation time τ_c	~ 10
Drift wave period	0.1~10
Averaging time of the data	10

Table 2. Comparison of different time scales.

Figure 3.5 shows the 2D contour plots of the beam profiles collected 3 ports away from the ion source when the plate-obstacle is positioned to block half of the plasma column and the fast ion orbit overlaps the turbulence wave region. Its FWHM is shown as the "in wave" case (diamonds) in Fig. 3.6.

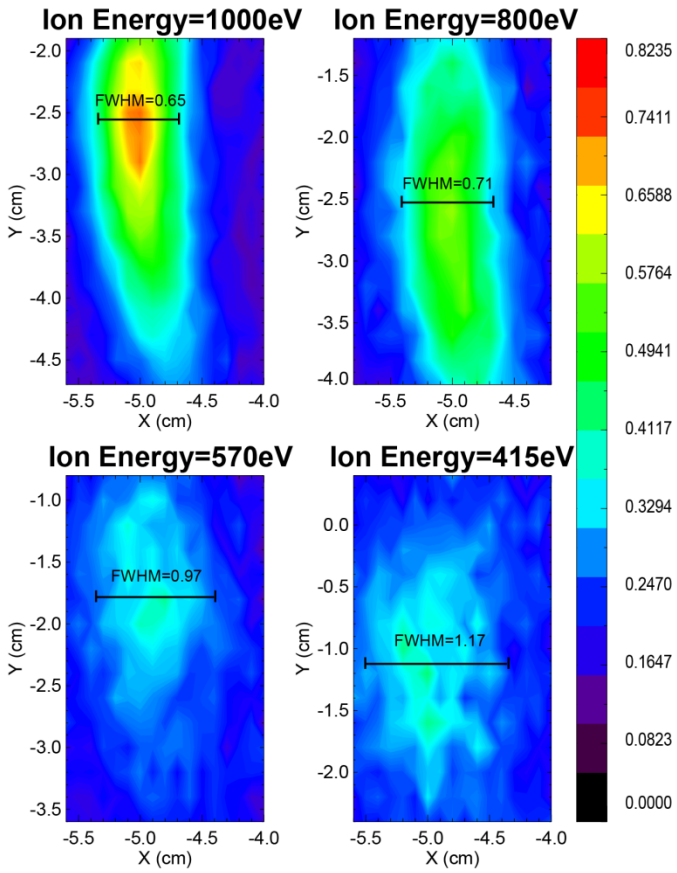

FIG. 3.5 Typical beam profiles for different fast ion energies, collected 3 ports (95.85 cm) away from the ion source.

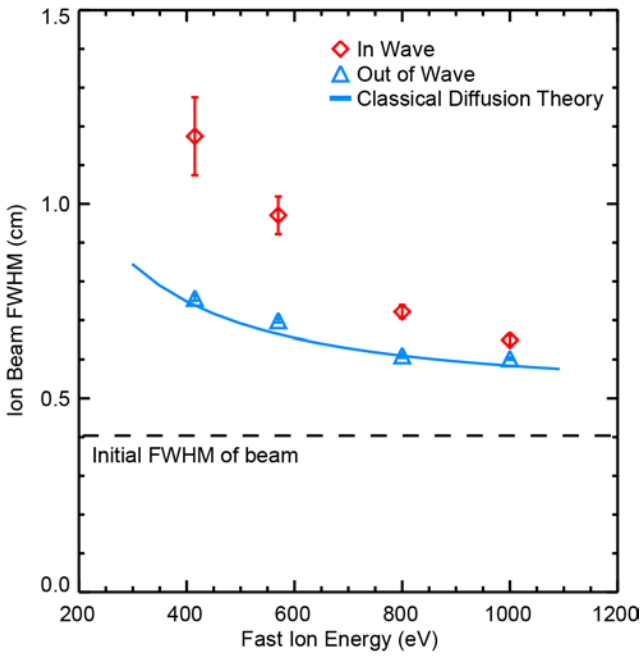

FIG. 3.6 Beam FWHM vs. energy with the plate inserted (diamond) and retracted (triangle). The solid line shows the dependence predicted by classical diffusion theory. The dashed line is the initial beam width caused by the finite aperture size of the ion source.

In Fig. 3.5, the contour of the beam spatial profile has a clear dependence on the fast ion energy. Greater fast ion transport is observed at lower beam energy. Note that the vertical length of the beam spot is limited by the angular acceptance of the fast ion analyzer, and does not describe the real beam azimuthal diffusion. Thus only the radial spreading of the beam is investigated. The radial FWHMs of the beam with and without the influence of drift waves show significant differences, especially at low beam energies (Fig. 3.6). The energy dependence of the beam FWHM is consistent with the observed original beam contour in Fig. 3.5.

The error bars shown in Fig. 3.6 are statistical error calculated among data taken at 10 consecutive LAPD discharges. During each discharge, 4000 samples, taken in ~10ms, are averaged to get the beam signal at a certain spatial location. The signal is also averaged by the RC time constant of the transmission circuit. The averaging of the signals filters out high frequency information but greatly increases the signal-to-noise ratio. Systematic errors include the axial and pitch alignment between the ion source and the ion analyzer. The axial alignment is carefully done with a telescope at the end viewpoint of LAPD. The pitch angles are adjusted by a digital level with accuracy of ~0.1°. Other possible errors include the fluctuation of the initial beam energy and angular divergence.

Besides the turbulence induced transport, the fast ion beam is always Coulomb scattered by the background plasma, resulting in classical diffusion of the beam. In this experiment,

the beam spatial profiles are also recorded for reference when the plate-obstacle is retracted, shown as "out of wave" data in Fig. 3.6.

The classical diffusion of fast ions in the LAPD plasma has been extensively studied, and expressions of the diffusivity have been developed theoretically and verified experimentally[28]. According to classical theory, the cross-field transport of particles is due to the pitch angle scattering with the background plasma in phase space, and the diffusivity is proportional to the background density. A theoretical prediction (solid line in Fig. 3.6) of the classical diffusion effect [following Eq. (12) in Ref. [28]] is found to agree quantitatively with the "out of wave" data. Consequently, induced beam transport due to the background plasma turbulence, which is always present in the non-equilibrium LAPD plasma during the active discharge, can be neglected for the "out of wave" case. In the "in wave" case, the fast ion beam is affected both by Coulomb collision and drift wave turbulence. Note that, the averaged background plasma density along the fast ion trajectory is lower by ~50% for this case due to density depression by the plate-obstacle, and the classical diffusivity is expected to be reduced by ~50%. The fast ion transport in this case is mainly due to interaction with drift wave turbulence.

3.2.2 Time dependence of radial transport

The fast ion beam signals are collected at 2-5 ports (63.9cm- 159.75cm) away from the ion source to study the time dependence of the beam radial transport, which, in this case, is equivalent to the spatial dependence. Because the fast ion parallel velocity is nearly constant for all energies, its total traveling time is proportional to the number of ports it passes. Contour plots of 400eV beam profiles at different distances from the ion source are shown in Fig. 3.7. Radial transport of the beam versus distance is observed, while the azimuthal spreading is not shown due to the limitation of the ion analyzer. The cut-off effect in the azimuthal direction is due to the $\pm 15°$ acceptance angle of the ion collector, while the actual azimuthal spreading is much broader due to the initial angular divergence. Thus the total energy collected by the ion analyzer is not conserved from port to port. The radial FWHM of the contours are shown in Fig. 3.8. The square of the FWHM is plotted in the figure to make a better comparison possible with the analytical models.

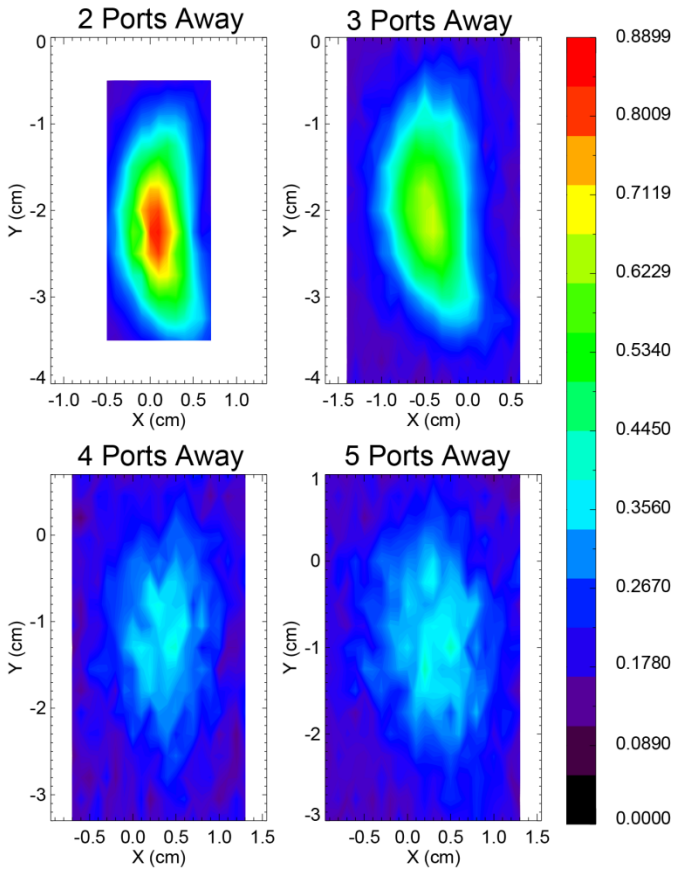

FIG. 3.7 Beam profile collected at different distances away (2-5 ports / 31.95-159.75 cm) from the ion source.

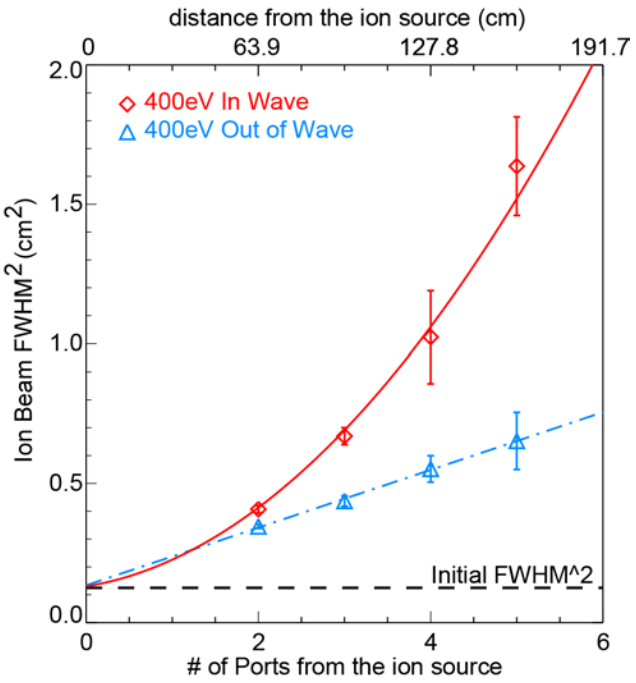

FIG. 3.8 The square of the radial ion beam FWHM vs. distance from the source. The "Out of Wave" data is fitted by a linear function. The "In Wave" data is fitted by a polynomial function of 2nd order.

For the "out of wave" case, the fast ion beam spreading is due to Coulomb scattering, as discussed in Ch. 3.2.1. In this case, with uniform axial speed, the time of travel t for an ion may be described by the axial distance travelled. In other words, by noting the number of axial ports, N, separating the ion beam source from the analyzer, the time t may be estimated if the parallel beam speed is known. Hence, a diffusive process would have $(\Delta r)^2 \propto t \propto N$. The proportionality constant between the diffusion coefficient and t was worked out[60] and experimentally confirmed in LAPD[28]. The data points are fitted to optimal curves to demonstrate their functional dependence on the traversed distance. Following Eq. 7 in Ref. [28], a linear fit

$$FWHM^2 = 8\ln 2(\langle \Delta r_0^2 \rangle + 2D_\perp t) \qquad (3.3)$$

for the "out of wave" data shows a diffusive nature of Coulomb scattering induced transport, with diffusivity $D_\perp = 2460 cm^2/s$.

For the "in wave" case, the density along the fast ion orbit is depressed by the plate-obstacle. Considering $D_\perp \propto n_{i,e}$, the estimated diffusivity due to Coulomb scattering is

$$D_\perp' = 1210 cm^2/s.$$

For this case, a discrepancy between the beam FWHM (diamonds) and the classical diffusion theory (dash dot line) is observed. The beam transport is much larger than

predicted by classical theory, indicating that turbulent transport dominates. Moreover, the "in wave" data cannot be fitted by a linear function. As discussed below, this reflects the non-diffusive nature of the transport.

3.3 DISCUSSION OF THE EXPERIMENTAL RESULTS

Since the turbulence wave frequencies we studied satisfy $\omega << \Omega_f$, and the fast ions only execute a few gyro-orbits, the turbulent electric fields are static on the fast-ion timescale. Also, the typical parallel wavelengths of the drift waves are long compared to the parallel distance of the fast ion trajectory. Thus an approximate model for the current experiment is that, each fast ion trajectory is affected by a quasi-2D, temporally constant electrostatic field. Different fast ions encounter changing realizations of the wave field, which randomizes the transport and results in the radial expansion of the beam spot.

The fast ion transport in such electrostatic turbulence is induced by two effects: change of fast-ion gyro radius due to change in particle perpendicular energy $\upsilon_\perp$, and drift of the fast-ion gyro center due to the turbulent electric field. The change in perpendicular energy follows the potential difference $\partial_t \phi$ during a gyro transit. One may estimate the change of the fast ion perpendicular energy $\Delta E_\perp \sim e\Delta\phi \sim \frac{n_1}{n_0} k_B T_e \sim k_B T_e$. Here we assume $n_1/n_0 \sim 1$ consist with the density fluctuation measurement. The observed plasma potential fluctuation behind the plate obstacle is ~10V, which confirms the above estimate. Then the particle transport in radial direction associated with the energy change is

$$\Delta r \sim \Delta\rho_f \sim \frac{1}{\Omega_f}\left(\sqrt{\frac{2(E_\perp + k_B T_e)}{m_f}} - \sqrt{\frac{2E_\perp}{m_f}}\right) \sim \rho_f \cdot \frac{k_B T_e}{2E_\perp} \quad (3.4)$$

For fast ion energy ~400eV and electron thermal energy ~10eV, $\Delta r \sim 0.046\text{cm}$, which is much smaller than the observed transport induced by wave. On the other hand, the gyro-center drift induced by the fluctuating potential during each transit can be estimated as

$$\Delta r_E \sim \frac{\delta E}{B}\frac{2\pi}{\Omega_{ci}} \sim 0.3\text{cm}, \quad (3.5)$$

with δE the fluctuating electric field. This is of the same order as the observed beam spreading. Thus the perpendicular energy of fast ion is approximately constant, and the transport is mainly induced by the drift of the fast ion gyro center.

3.3.1 Gyroaveraging

The energy dependence of the beam FWHM for "in wave" (diamonds in Fig. 3.6) can be explained in terms of the so-called gyro-averaging effect. Since the gyro motion is much faster than the turbulent wave frequency, the gyroaveraging approximation can be applied[14]. With the perturbed drift of the gyro center during each

cyclotron period small compared to the gyroradius, the turbulent potential ϕ is then substituted by an averaged $\bar{\phi}$ over the gyro-orbit (see Chapter 1.1),

$$\bar{\phi}(x) = \sum_k \phi_k e^{ik\cdot x} \cdot J_0(k_\perp \rho), \qquad (3.6)$$

which results a reduction in the potential fluctuation. In our experiment, $k_\perp \rho$ is of the order of 1, thus neither larger or small argument expansion can be applied. To estimate the gyroaveraging effect, the cross-correlation of ion saturation currents between two triple probes [Fig. 3.9(b)] is used to indicate the turbulence mode structure and relative wave amplitude at different wavelength, and the gyroaveraging approximation is imposed to calculate the reduced potential due to averaging along different gyro orbits. Here we assume that, for electrostatic drift waves, the fluctuation of the electric potential is proportional to the fluctuation of the plasma density, and that the density is proportional to the ion saturation current of the Langmuir probe measurement.

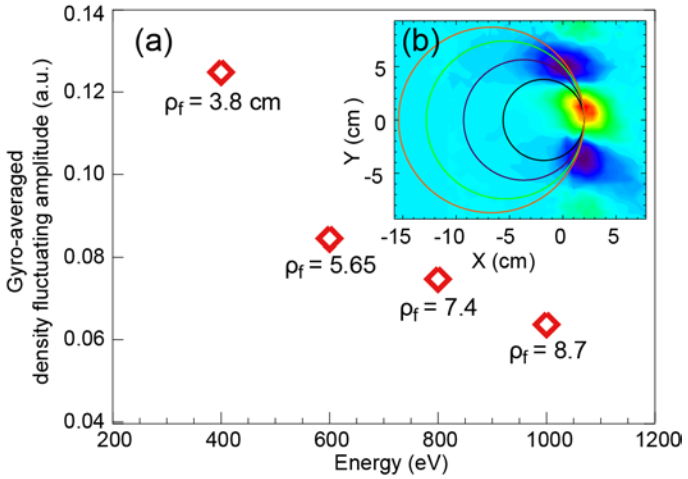

FIG. 3.9 (a) The gyro-averaged density fluctuation shows a large reduction of fluctuation amplitude, and the fluctuation amplitude decreases with increased fast-ion energy. (b) The cross-spectrum of the drift wave, measured by two triple probes two ports away (63.9 cm) from each other. The four measured gyroradii are overlaid.

Figure 3.9(a) shows the relative density fluctuation amplitude due to averaging over gyro-orbits of different energies (400-1000eV), which is characterized by δI_{sat} along the gyro-center positions. The gyro-averaged fluctuation is reduced at large beam energy, which agrees qualitatively with the energy dependence of the beam FWHM broadening.

3.3.2 Non-diffusive transport due to wave-particle correlation

The time dependence of the FWHM spreading (diamonds in Fig. 3.8) shows a non-diffusive nature of the radial transport. The data when the drift waves are on do not lie on a linear curve, indicating that the diffusivity D is not constant. The non-diffusive transport, also

referred to as ballistic transport, of ions with large Larmor radii has been discussed in several theoretical papers[12-13], and is related to the correlation between waves and fast ions. Following the discussion in Chapter 1.1, the diffusion coefficient D depends on the Lagrangian correlation function of the particle velocity L_{ii}, which in this experiment is closely related to the correlation between waves and fast ions. In the current experiment, the parallel decorrelation time $\tau_{\|}$ is much longer than the perpendicular decorrelation time $\tau_{\perp}$. $\tau_{\|}/\tau_{\perp} \sim (L_{\|}/v_z)/(L_c/\bar{v}_E) \sim 20$, where $L_{\|}$ is the parallel correlation length, v_z is the fast ion parallel velocity, L_c is the perpendicular scale length of the wave potential. Thus L_{ii} is mainly determined by the correlation of the fast-ion perpendicular velocity. The perpendicular velocity can be expressed as $v_i(x,t) = v_c + v_E(x,t)$, where v_c is the cyclotron velocity associated with its perpendicular energy, which is approximately constant; $v_E(x,t)$ is the drift velocity of its gyro center associated with the turbulent E field it samples during the whole gyro orbit. Thus $L_{ii} \cong \langle v_E(0,0) v_E(x,t) \rangle$. As the wave turbulence is static in the fast ion transition time scale, the spatial correlation between the fast ion orbit and the turbulent potential structure determines L_{ii}. As illustrated in Fig. 3.10, if $\bar{v}_E t < L_c$ [Fig. 3.10(a)], with L_c the spatial scale length of the wave potential structure, the fast ion orbit always samples approximately the same turbulent potential structure. Thus $L_{ii} \cong \text{const}$, and the gyro center drift is ballistic. When $\bar{v}_E t > L_c$ [Fig. 3.10(b)], the orbit starts to sample a different potential structure, which randomizes v_E and induces a diffusive transport.

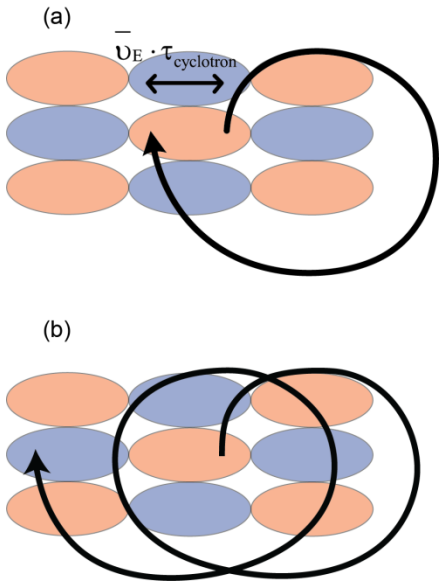

FIG. 3.10 (a) The fast ion is correlated with the turbulent potential structure if the drift of gyro center during each cyclotron orbit is smaller than the correlation length of the turbulence. (b) If the perturbed drift exceeds the turbulent potential scale length, the fast ion orbit starts to sample a different turbulent potential structure .

In the current experiment, the total broadening of the beam is ~1cm within 5 gyro orbits, $\bar{\upsilon}_E t_c \sim 0.2\text{cm}$ per orbit, and the typical $L_c \sim 5\text{cm}$. Thus decorrelation between the fast ion trajectory and the turbulent potential does not happen, the averaged drift velocity $\bar{\upsilon}_E$ is approximately constant during the whole particle trajectory, and $L_{ii} \cong \bar{\upsilon}_E^{\,2}$. The diffusive coefficient for the turbulence induced transport is then

$$D_{dr}(t) = \bar{\upsilon}_E^{\,2} t . \qquad (3.7)$$

The total beam FWHM, considering its initial width and classical diffusion[28, 60], is

$$\begin{aligned} W_{FWHM}^2 &= 8\ln 2[\langle(\Delta r_0)^2\rangle + 2(D_{cl} + D_{dr})t] \\ &= 5.545[\langle(\Delta r_0)^2\rangle + 2D_{cl}t + 2\bar{\upsilon}_E^{\,2} t^2] \end{aligned} \qquad (3.8)$$

Using Eq. 12 in Ref. [28] as the classical diffusivity D_{cl}, this expression fits the "in wave" data very well (blue curve in Fig. 3.8), proving the validity of the above model and analysis. This analytic model is confirmed by the more detailed simulation of Sec. 3.4.

3.4 SIMULATION RESULTS

A numerical simulation is performed to model the transport of fast ions in the turbulent drift wave field using a combination of the BOUT code and a test particle tracer code. BOUT was developed to model tokamak edge turbulence using collisional fluid equations, and was recently modified[44] to model the cylindrical LAPD plasma. The drift wave turbulence is simulated using fixed-profiles in BOUT by subtracting out the azimuthal average of the fluctuating density at each time step, preventing turbulent transport from relaxing the profile[45]. This technique in effect assumes that density fluctuations are small compared to the mean value and fails in the presence of strong fluctuations. Because of this, a shallower gradient than the actual experimental profile was used in the simulations. Simulations using particle sources and sinks which allow full nonlinear evolution of the profile are possible in BOUT and will be pursued in future work[45]. The other input parameters are the same as the experimental conditions in order to achieve a reasonable comparison with the experimental data.

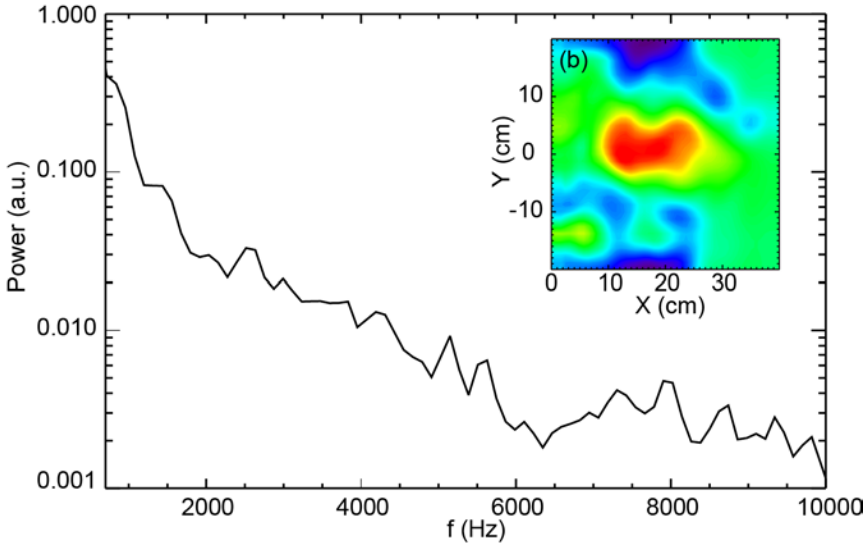

FIG. 3.11 The characteristics of drift wave turbulence simulated by the BOUT code. (a) Fluctuation power spectrum (b) Cross-correlation of the potential fluctuation

Figure 3.11(a,b) shows the frequency spectrum and cross-field correlation function of the potential fluctuation calculated with the BOUT code. It is qualitatively consistent with the previously discussed experimental results [Fig. 3.4(b)]. As in the experiment, the spectrum predicted by BOUT is dominated by low-frequency turbulence (0.1~10kHz) but the calculated spectrum is narrower than the observed one. The correlation length (~10cm) agrees well with the measurement from the triple probe [Fig. 3.9(b)]. The amplitude is smaller than in the experiment, presumably because the density gradient employed in the calculation is less steep. The wave electric field is derived from the potential profile, and the amplitude of the field is multiplied by a factor to match the experimental measurement.

The spatial fluctuation spectrum of the BOUT result is then imported into a Monte-Carlo code to simulate the fast-ion behavior in the calculated wave fields. The fast ion beam density in our experiment is typically $\sim 5.0\times10^{8}$ cm^{-3}, and is three to four orders of magnitude smaller than the background plasma density. Thus the fast ions can be treated as test particles in the code, and their trajectories are fully determined by the interaction with the turbulent wave field and background plasma. A previous investigation of fast-ion classical diffusion[28] shows that, in LAPD, pitch angle scattering is the dominant effect causing classical diffusion of the fast ions. Other effects such as Coulomb slowing down, and collision between fast-ions and neutrals, typically have a time scale two orders of magnitude larger than Coulomb collision, thus they can be neglected for the current configuration.

Classical diffusion by pitch angle scattering is modeled by a Monte-Carlo collision operator[61-62]. The drift wave turbulence induced transport is modeled by following the trajectory of a fast ion within the background electric field fluctuation. For comparison with

the experimental data, the calculated fast-ion beam spatial profiles are recorded at the same positions as each observation port. Since the experimental signals average over many realizations of the drift-wave turbulence, a randomly selected sample of the computed drift wave potential is chosen as the background turbulence at the beginning of each fast ion trajectory. When tracing each fast ion, the background field is assumed static and axially symmetric during the whole particle trajectory.

Without the turbulence, the fast ion transport, which is shown as the "Out of Wave" case in Fig. 3.12, is well described by classical diffusion theory. The simulated beam FWHM^2 at 0-5 ports away from the initial position are consistent with the experimental data shown in Fig. 3.8, and the transport is diffusive.

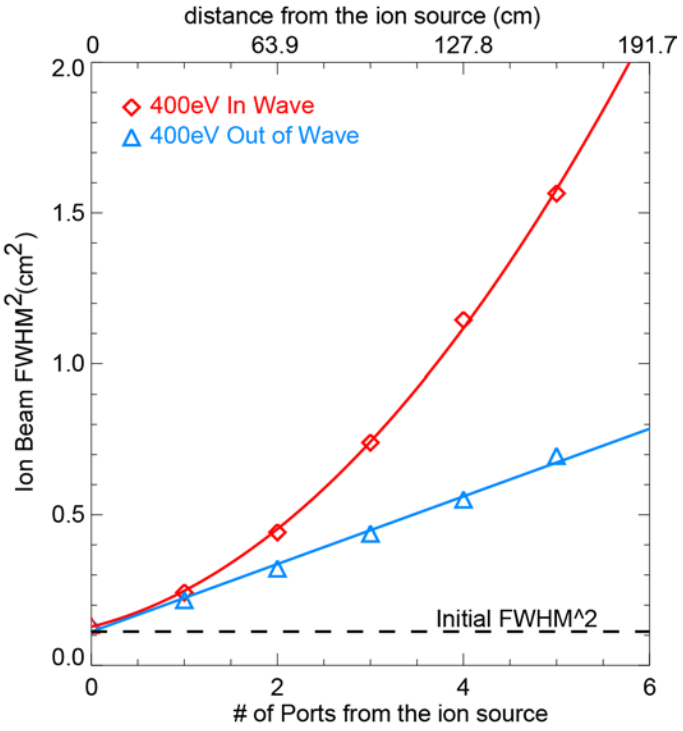

FIG. 3.12 Monte Carlo simulated fast ion FWHM^2 as a function of distance (time). Triangles denote the effect of the classical transport, and is fitted by a linear function. Diamonds denote the effect of both turbulent wave and classical transport, and is fitted by a polynomial function of 2nd order.

The turbulent wave effect is then added into simulation. The reduction of classical transport due to the density depression by obstacle was not considered in the simulation, thus the classical transport effect is assumed the same for both cases. In Fig. 3.12, the "In Wave" FWHM data shows a good fit with Eq. 3.8 when Δr_0 and $D_\perp$ are set the same as the "Out of Wave" case. Like the experimental data, the simulation shows the ballistic nature of the fast ion transport for these conditions.

To confirm the physical mechanism of the transport, the relation between decorrelation and diffusive transport is demonstrated by following the gyro-center (GC) trace of a single particle in turbulent wave fields of different amplitudes. Figure 3.13 displays the motion of the fast ion GC for two different wave amplitudes. When orbiting in a relatively small amplitude fluctuation, the drift of the fast ion GC drift (diamond) in each cyclotron period is small compared to the correlation length of the potential structure, which means that the fast ion is not decorrelated from the wave during its five cycles. Consequently, the GC shifts add approximately linearly over the entire trajectory, which yields a non-diffusive transport. In contrast, for stronger wave amplitude, the fast ion (triangle) drifts out of the correlation region. It is then able to sample a randomized potential field, and the transport is diffusive.

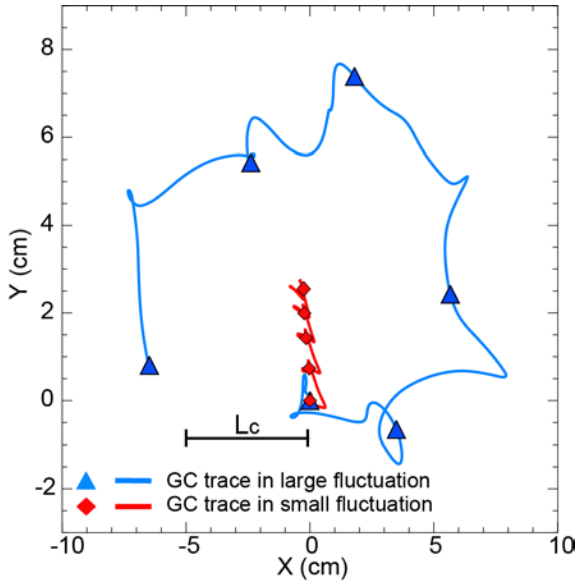

FIG. 3.13 The trajectory of an individual guiding center in a representative turbulent potential structure. The triangles and diamonds show the fast ion GC position after each cyclotron orbit, 0-5 ports away from the ion source for turbulence with large (blue) and small (red) amplitude.

3.5 CONCLUSIONS

In this experimental work, the energetic ion transport due to the turbulent drift wave is directly measured from the non-classical spreading of the beam induced by the electrostatic potential field of the turbulence. The transport is observed to decrease as the fast ion energy increases. The time dependence of the transport is non-diffusive (ballistic), with the diffusive coefficient proportional to time. The mechanism of such transport is modeled and discussed. The energy dependence of the beam spreading is due to the gyroaveraging effect of fast ions with different orbit size. The non-diffusive nature of the transport is the result of the correlation between the fast ion trajectory and the turbulent

potential structure. Both analytical model and simulation results provide good agreement with the experimental data.

Chapter 4
DEPENDENCE OF FAST-ION TRANSPORT ON THE NATURE OF THE TURBULENCE

4.1 EXPERIMENTAL SETUP

4.1.1 Overview

In Chapter 3, the energy scaling of fast-ion transport in drift-wave turbulence induced by a half-plate obstacle is investigated. However, the fast-ion orbits are only partially immersed in waves due to the geometry of the obstacle, and the wave characteristics are not modified. In the experiment reported in this chapter, the gyro-radius is kept constant, and the dependence of the fast-ion transport on the background turbulent wave characteristics, such as correlation length and perpendicular wavelength, are studied. An annular obstacle is placed in the LAPD chamber to block primary electrons from the cathode-anode source. The obstacle induces large density gradients with cylindrical geometry downstream and destabilizes waves. Modification of wave characteristics is done by changing the plasma species, and by biasing the obstacle at different voltages. Coherent and turbulent waves with various mode numbers are observed in helium and neon plasmas. The fast-ion beam diffusion in different background waves is thoroughly investigated.

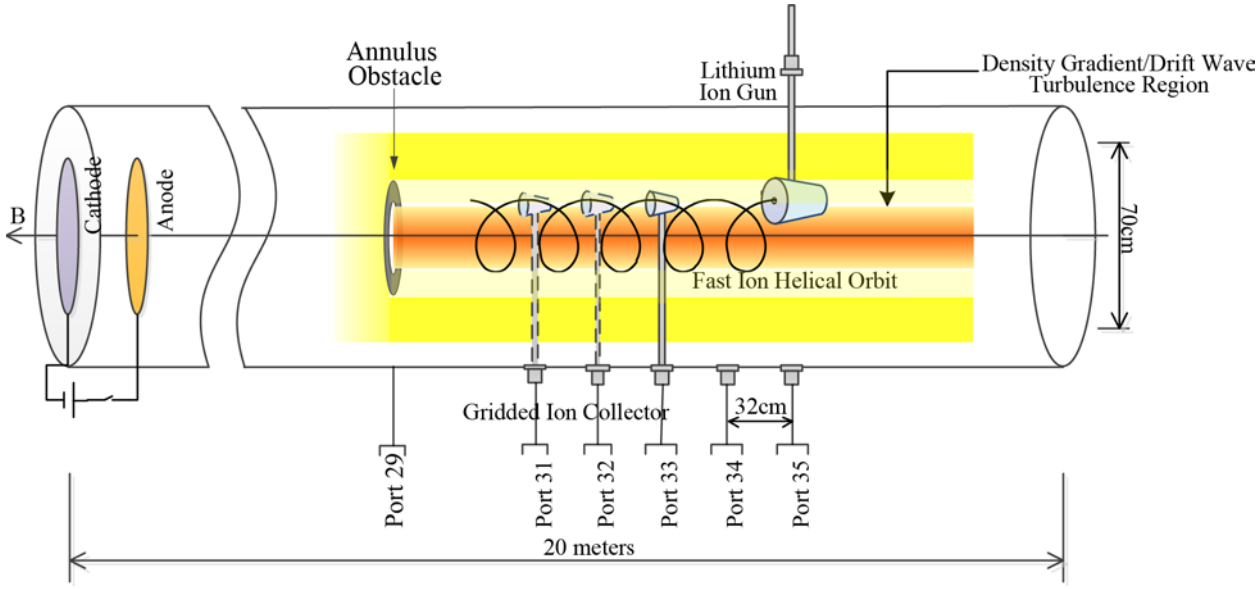

FIG. 4.1 Schematic of LAPD including the annular obstacle, the lithium ion gun and the ion collector. The ion collector is inserted at various axial locations to study the spatial dependence of the beam transport. The ion gun and collector are axially aligned and operated at the same pitch angle. Fast ion beam orbits are helical and fully overlapped with the steep gradient region.

The experimental setup is shown schematically in Fig. 4.1. The plasma parameters in LAPD for this experiment are set to be the same as that reported in Chapter 3. A copper, annular obstacle with inner radius of 6*cm* and outer radius of 10*cm* is inserted upstream (port 29), nearly concentrically with the plasma column. When placed, the obstacle blocks the plasma-forming primary electrons parallel to the magnetic field, and significantly decreases the downstream plasma density. A steep density gradient, along with large density fluctuations, is observed on the inner edge region of the annular depletion.

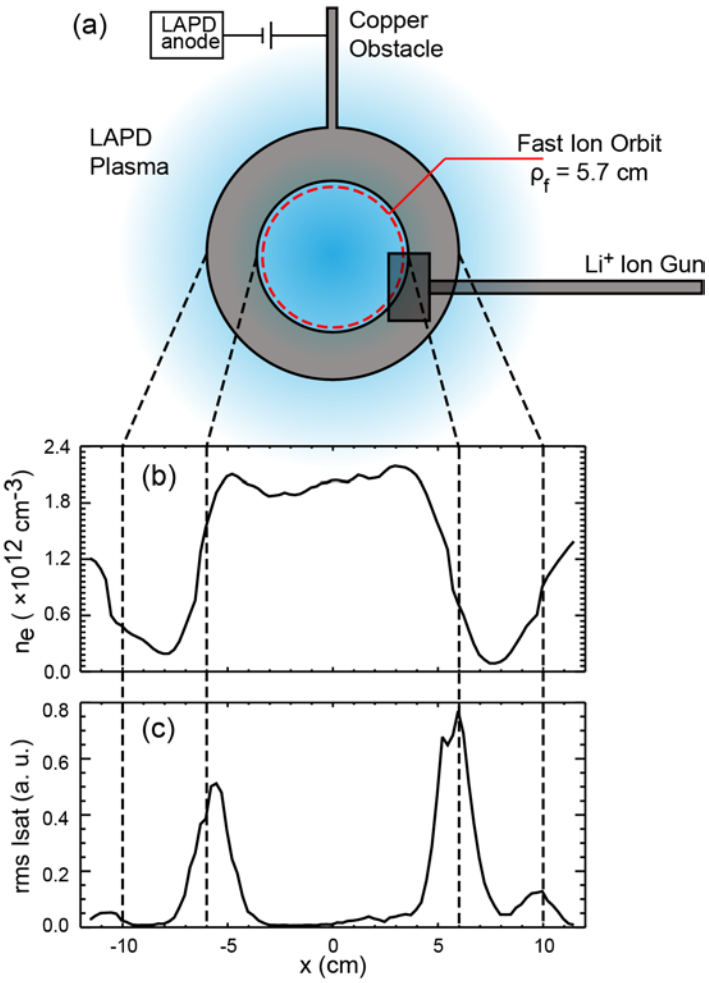

FIG. 4.2 (a) Schematic of the LAPD end-view. Fast ion gyro-orbit (dashed line) overlaps with the steep gradient region. The copper obstacle can be biased positively related to the LAPD anode by an external power supply. (b) Typical plasma density profile. (c) Typical root-mean-square (RMS) fluctuation of the ion saturation current.

Figure 4.2 shows a typical radial profile of the plasma density n_e and root-mean-square (rms) of ion saturation current I_{sat} fluctuation amplitude measured 0.3*m* downstream from the annulus during the ~10 ms plasma discharge. The annular obstacle is either floating or positively biased relative to the LAPD anode using a DC biasing power supply.

The lithium ion gun is inserted into the LAPD plasma at port 35 with variable pitch angle to the axial magnetic field. The fast ion energy in this experiment ranges from 300eV up to 600eV. The gyro-radius of the beam perpendicular motion is set to be 5.7*cm*, which is slightly smaller than the inner radius (6*cm*) of the annular obstacle (red dash line in Fig. 4.2(a)). Thus the beam trajectories fully overlap with large plasma density and potential fluctuations. A collimated fast ion collector is inserted at three axial locations (port 31-33, with axial distance of 64-128 cm from the source) to measure the beam spreading as a function of its time-of-flight in the waves.

4.1.2 Waves associated with an annular obstacle

In the current experiment, the observed plasma density gradient 0.3*m* downstream from the inner edge ($x = \pm 6\,\mathrm{cm}$) of the obstacle has a transverse scale length $L_n = |\nabla \ln n|^{-1} \sim 2\mathrm{cm}$ (the background ion sound gyroradius in helium plasma is $\rho_s = 0.6\,\mathrm{cm}$, and the ion gyro-radius $\rho_i \sim 0.24\,\mathrm{cm}$). The typical plasma density and potential fluctuations observed have similar amplitude ($\delta n / n \sim e\tilde{\phi} / k_B T_e \sim 0.5$). The parallel wavelength $\lambda_{||}$ of the fluctuation is measured by two Langmuir probes aligned axially and separated by 2.2*m*. A phase difference of 50° is observed between the I_{sat} signals of the two probes, indicating that $\lambda_{||} \sim 15\mathrm{m}$, which is comparable to the LAPD machine length. The long and finite parallel wavelength is expected in drift-wave like turbulence. Measurements with a B-dot probe indicate that the fluctuation in ambient magnetic fields is $\delta B / B \sim 0.2\%$.

Several means are employed to change the wave characteristics such as mode numbers (*m*) and spatial correlation length (L_{corr}). Driving azimuthal $E \times B$ flow has been reported as an effective way to modify the LAPD edge turbulence in a wall-biasing experiment[38]. A similar setup is used here to bias the annular obstacle positively relative to the LAPD anode. With the obstacle biased, a plasma potential gradient is observed downstream and large $E \times B$ drift in the azimuthal direction is driven ($v_{E\times B} / v_s \sim 0.5$, where v_s is the ion sound velocity, measured using a Mach probe). Other ways to modify the wave scale size are to use different plasma species and to modify the amplitude of the axial magnetic field. Density and potential fluctuations under a broad range of the obstacle biasing voltage, plasma species and axial magnetic field strength have been documented, and several typical cases with varied scale lengths are selected for the fast-ion transport study.

Case #	Plasma	$V_{annulus}$ (V)	$n_e (\times 10^{12} cm^{-3})$	$\delta n / n$	$e\tilde{\varphi} / k_B T_e$	$\bar{m}$	$L_s (cm)$	$L_{corr} (cm)$
A	helium	floating	2.2	0.55	0.46	7	2.6	23
B	helium	100	2.0	0.53	0.48	7	2.6	6
C	neon	75	1.4	0.35	0.47	2	6.3	19

D	helium	floating	2.0	0.30	0.30	7	2.6	7

Table 3. Wave characteristics for the four cases with complete fast-ion data

Three typical wave conditions with different azimuthal correlation length L_{corr} and potential structure scale length L_s (parameters listed as case (A)-(C) in Table 3) are chosen for the fast-ion transport study: (A) in helium plasma with the annulus floating, (B) in helium plasma with the annulus biased at 100V relative to LAPD anode; and (C) in Neon plasma with annulus biased at 75V. Figure 4.3(a) shows a two-dimensional (2D) cross-field correlation function for I_{sat} fluctuations in case (A), measured using two triple probes separated along the magnetic field by 0.3m. L_{corr} is defined as the azimuthal scale length of the wave cross-correlation function, and $L_s \sim \pi\rho_f / \bar{m}$ is the scale size of a wave density/potential structure, with $\bar{m}$ the average mode number and ρ_f is the fast-ion gyroradius. In fully turbulent fluctuations, $L_{corr} \sim L_s$ (case (B)), while in coherent waves L_{corr} can be much longer than L_s (case (A)). It is assumed here that density and potential fluctuations have similar scale size in drift-wave like turbulence. The power spectrum contours and 2D correlation functions of I_{sat} in all three cases are compared. In helium plasmas, when the annulus is floating (Fig. 4.3), the observed waves are very coherent, with mode number dominated by $m = 6-8$ ($L_s \sim 2.6\text{cm}$), and have relatively long azimuthal correlation length ($L_{corr} \sim 23\text{cm}$). When the annulus is biased to 100V, the waves (Fig. 4.4) are more turbulent. The azimuthal correlation length is changed significantly ($L_{corr} \sim 6\text{cm}$), and the I_{sat} power spectrum is closer to broadband. L_s in this case is similar to case (A). In neon plasmas with 75V bias on annulus, waves with mode number $m = 1-3$ ($L_s \sim 6.3\text{cm}$) and long azimuthal correlation ($L_{corr} \sim 19\text{cm}$) are observed (Fig. 4.5).

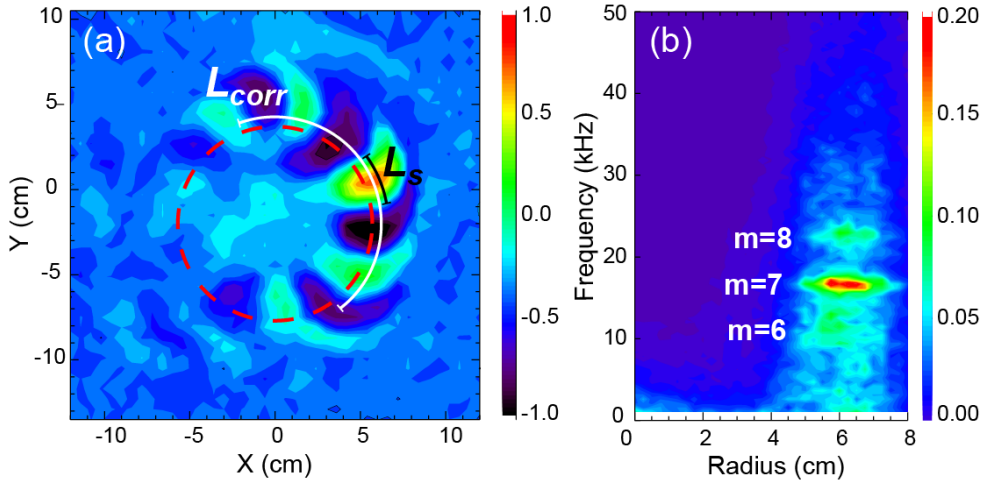

FIG. 4.3 (a) Two-dimensional cross-field correlation function for I_{sat} in case A, with the wave azimuthal correlation length (L_{corr}) and structure scale size (L_s). The asymmetry in the correlation pattern is caused by

the decorrelation of the signals between the reference probe (located at (6,0) in (a)) and the moving probe. (b) Contour of the spatially resolved wave spectrum for this case. The dominant modes are *m=6-8*.

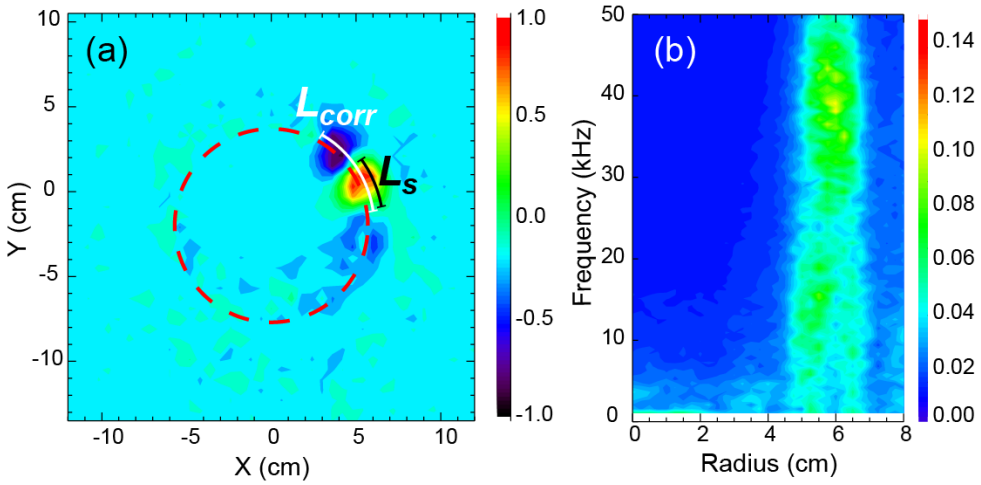

FIG. 4.4 (a) Two-dimensional cross-field correlation function for I_{sat} in case (B). (b) Contour of the spatially resolved wave spectrum for this case. The waves have average mode number $\bar{m} = 7$, short azimuthal correlation length and are broadband.

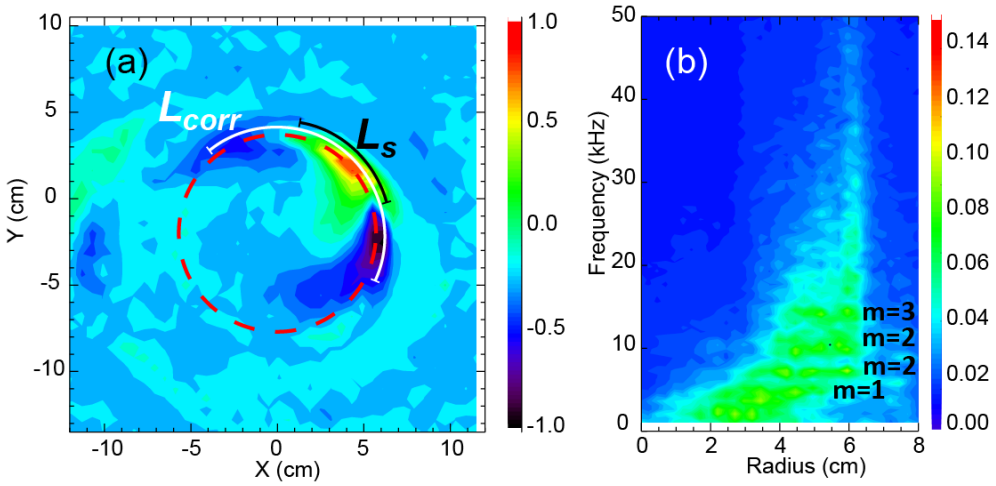

FIG. 4.5 (a) Two-dimensional cross-field correlation function for I_{sat} in case (C). (b) Contour of the spatially resolved wave spectrum for this case. The dominant modes are *m=1-3*.

4.2 FAST-ION TRANSPORT IN VARIOUS BACKGROUND WAVES

4.2.1 Observed beam broadening in waves

A ^{7}Li ion beam with energy $E = 575eV$ and pitch angle $\theta_{pitch} = 48^\circ$ is launched and collected at several positions (64 cm, 96 cm, 128 cm away from the source) to obtain the beam transport due to the background waves that were described in the previous section. Beam 2D profiles are obtained by time-averaging over the collector signal taken at a selected spatial grid. The broadening of the beam profiles in the radial (along the gyro-radius)

direction indicates cross-field transport. The spatial-averaged radial profile is fitted into a Gaussian function to quantify the beam full-width at half-maximum (FWHM). As discussed in Chapter 3, the beam broadening in the azimuthal direction (along the gyro-orbit) is not accurately measured, due to the limited angular acceptance of the collimated collector. Thus only the radial profiles of the beams are analyzed.

To quantify the fast ion transport due to interaction with drift-wave turbulence, the classical transport by Coulomb collisions with the background plasmas (dominated by ion-ion pitch angle scattering) is estimated and subtracted. The analysis method of the fast-ion signal is described in detail in Chapter 2.4.1, and is used throughout this thesis work. The classical diffusion of fast ion beams in LAPD is well understood[28] and a Monte-Carlo (MC) code simulates the beam broadening due to classical effects. Another indicator of the classical diffusion effect is the beam FWHMs in early afterglow plasmas ($<10\,\mathrm{ms}$ after the discharge ends). When LAPD discharge is terminated, the electron temperature (T_e) decays rapidly, while the plasma density (n_e) drops on a much slower timescale. In the early afterglow (n_e drops by $\leq 20\%$, $T_e \leq 1\mathrm{eV}$), the ambient plasma is quiescent relative to the active discharge, and fast-ion cross-field transport is mainly due to classical Coulomb collisions. Since the Coulomb collision mainly depends on the thermal plasma density, and is insensitive to the rapid drop in T_e, the beam width in early afterglow is a good indicator of the classical diffusion level of the fast ion beam. Figure 4.6 shows the collected beam in helium plasma for (a) afterglow, (b) active phase with no bias (case (A)) and (c) with V_{bias}=100V(case (B)). Figure 4.7 shows the collected beam in neon plasma for (a) afterglow, (b) active phase with V_{bias}=75V(case (C)).

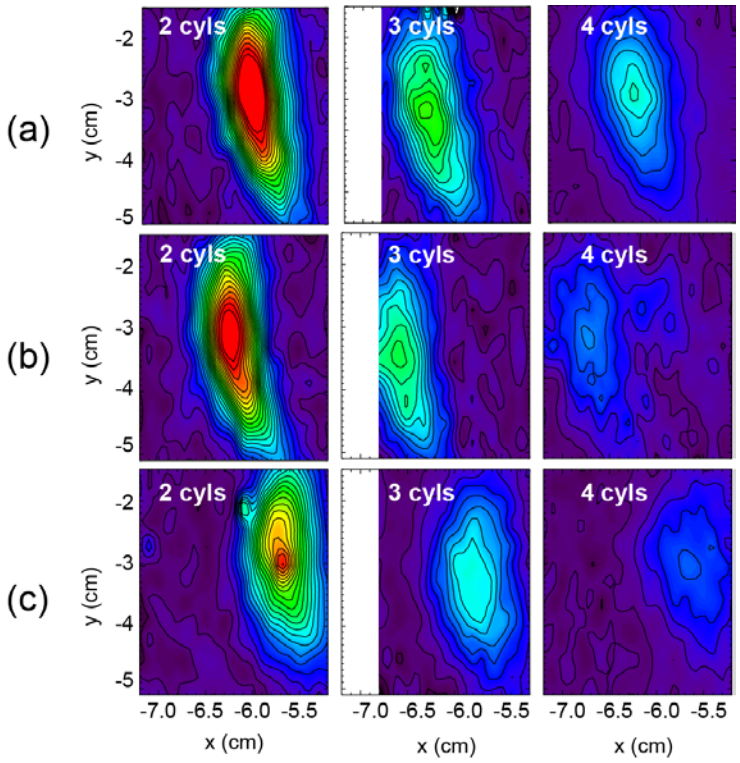

FIG. 4.6 Contour plot of the collected beam signal in helium plasmas for (a) afterglow, (b) active phase with no bias (case (A)) and (c) with V_{bias}=100V(case (B))

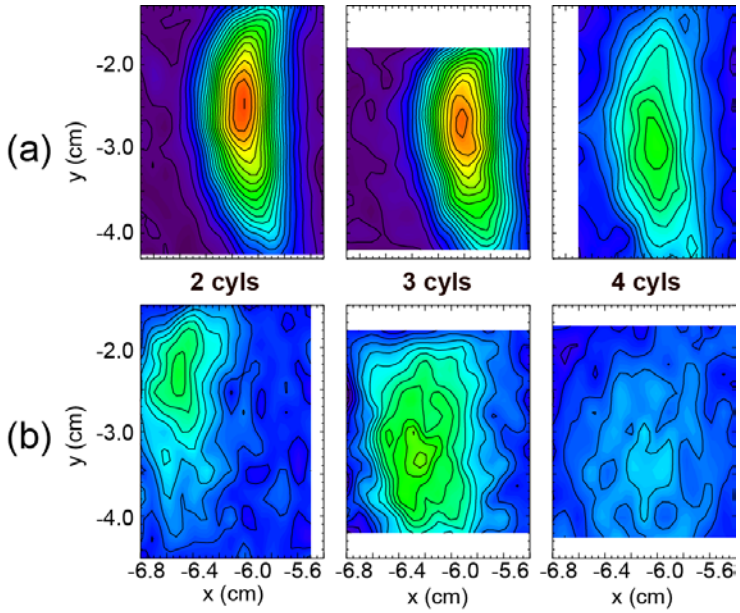

FIG. 4.7 Contour plot of the collected beam signal in neon plasmas for (a) afterglow, (b) active phase with V_{bias}=75V(case (C))

The beam FWHM measured in the early afterglow is compared with the simulation result obtained by the MC code and shows good agreement in both helium and neon plasmas (Fig. 4.8).

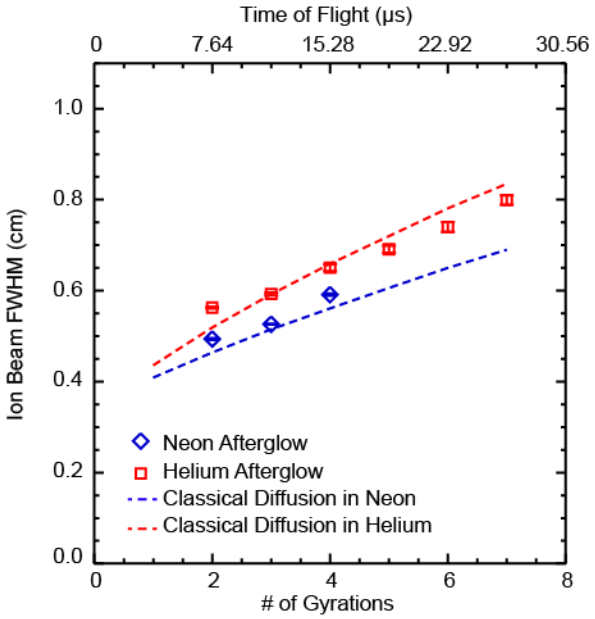

FIG. 4.8 Spatial-temporal evolution of the fast-ion beam full-width at half-maximum (FWHM) in LAPD afterglow in Helium (square) and Neon (diamond) plasmas. Classical diffusion levels in these cases (dashed lines) are simulated by a Monte-Carlo code and agrees well with the experimental data.

Fast ion beam profiles in LAPD active discharges ($n_e \sim 2.5\times10^{12}\,\mathrm{cm}^{-3}$, $T_e \sim 5\mathrm{eV}$) indicate both classical transport and transport due to interaction with low-frequency wave potential fields. Beam profiles in various background waves (cases (A)-(C)) are compared (Fig. 4.9).

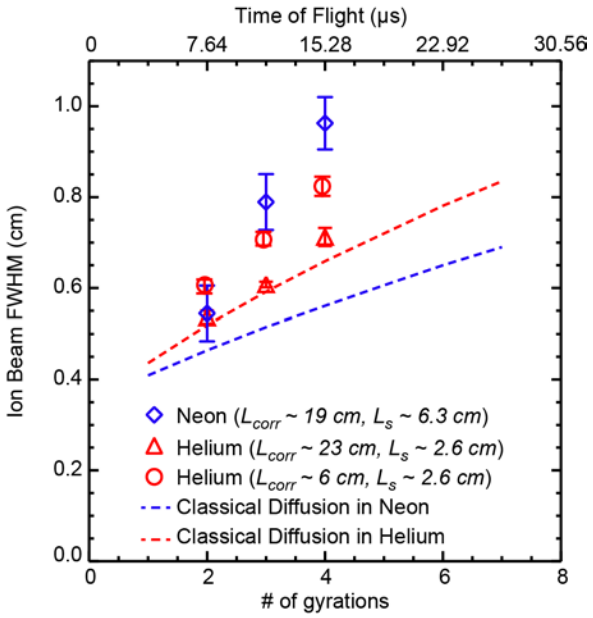

FIG. 4.9 Spatial-temporal evolution of the fast-ion beam FWHM during LAPD discharge when the fast ions overlap with the waves described in cases (A)-(C). The simulated classical diffusion (dashed lines) is also plotted.

When the background waves are azimuthally coherent and with a large mode number (case (A), red triangles), the beam radial FWHMs are comparable to the classical transport level, indicating that the wave induced transport is very small. In contrast, when in waves with small mode number and large structure size (case (C), blue diamonds), beam radial FWHMs greatly exceed the classical diffusion level, indicating that wave-particle interaction dominates the beam broadening. Two cases with similar averaged mode number, but very different correlation length L_{corr} (case (A) & (B)) also have different levels of transport. A more broadband wave with shorter L_{corr} (case (B), red circles) induces larger beam broadening.

4.2.2 Reduced fast ion cross-field transport by gyro-averaging

The difference of beam broadening in various background waves can be explained by the gyro-averaging effect. Following discussions in (3.3.1), equation (3.6) shows that the gyro-averaged potential depends on the amplitude and spatial spectrum of fluctuating potential (ϕ_k), and the ratio of fast-ion orbit size (ρ_f) to wave potential structure size ($k_\perp^{-1}$). In this thesis work, experimental results regarding the dependence of fast-ion transport on these parameters are discussed.

In the previous shear-Alfvén-resonance experiment, it was reported that the fast ion beam is weakly affected by magnetic fluctuations with $\delta B/B \sim 1\%$ unless the Doppler-shifted cyclotron resonance condition is satisfied[30]. Therefore, in this investigation, the beam broadening due to magnetic fluctuation can be neglected, and the ambient wave can be

treated as electrostatic. As discussed in Chapter 3.3, the fast ion beam broadening is mainly the result of the gyro-center drifts in the electrostatic wave potential.

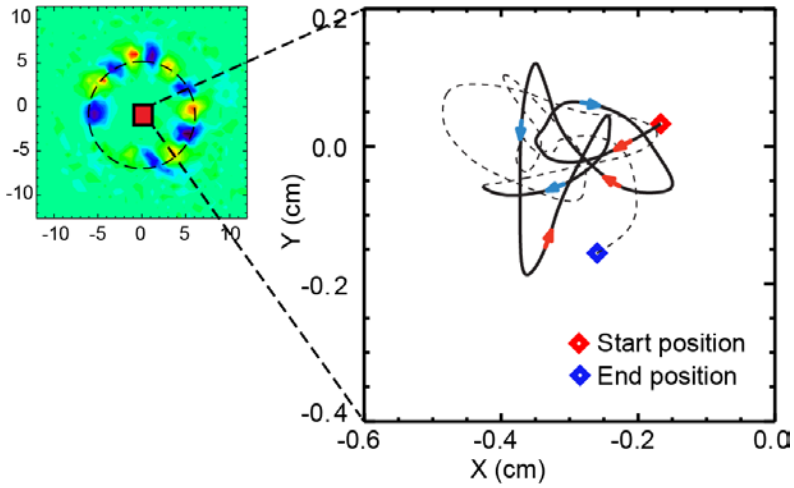

FIG. 4.10 The trajectory of a test particle gyro-center (GC) in coherent wave potential fields. The potential structure is inferred from the cross-correlation function of I_{sat} for case (A).

The predicted effect of the gyro-averaged fast ion gyro-center drifts are illustrated by plotting a test particle gyro-center (GC) trajectory (Fig. 4.10) in an experimentally measured coherent wave field (waves in case (A)). Due to the time scale separation between the fast ion cyclotron frequency and the characteristic frequency of the waves ($\Omega_f >> \omega_{DW}$), the fast-ion samples nearly static azimuthal potential structures during each gyro-orbit. The scale length of the test particle GC drift through one potential structure is ~ 0.2 cm. In waves with long L_{corr}, the $E \times B$ drifts cancels each other when the beam orbit passes through the coherent potential structures. So the total drift averaged over the gyro-orbit is greatly reduced compared to that in a stochastic potential field.

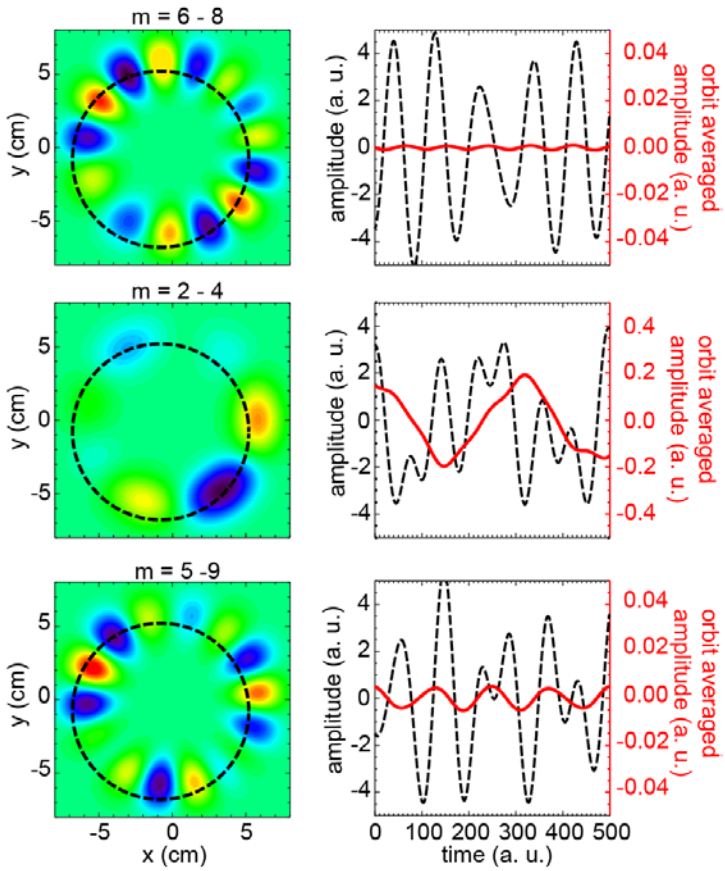

FIG. 4.11 (Left) Wave potential fields with characteristics similar to the experimental cases (A) - (C), modeled by Eqn (4. 2). (Right) Original potential fluctuation (black dashed line) and fluctuation after orbit-averaging (red solid line) over the indicated gyro-orbit.

An estimate of the gyro-averaging effect in different observed background wave fields is illustrated in Fig. 4.11. The wave potential structures for cases (A)-(C) are modeled by

$$\phi(r,\theta,t)=\sum_m \phi_m \cdot \sin(m\theta+\omega t+\theta_0)e^{(\frac{(r-r_0)^2}{a})} \qquad (4.1)$$

with $m=6-8$ for case (A) and $m=1-3$ for case (C). Nonlinear simulation is required to model the fully turbulent potential fields in case (B). However, the effect of the turbulent waves to the fast-ion transport can be demonstrated roughly by waves with more modes ($m=5-9$). The averaged potential $\bar{\phi}(r,\theta,t)$ over a gyro-orbit is obtained using Eqn. (3.6). The wave amplitudes in all cases are kept the same. The ratios of fluctuating amplitude after gyro-averaging to the original amplitude ($|\bar{\phi}_{A,B,C}|/|\phi_0|$) indicate the effectiveness of the gyro-averaging for different wave characteristics. For case (A), $|\bar{\phi}_A|/|\phi_0|<0.1\%$, indicating a large reduction of fast-ion-sampled wave amplitude due to the coherency and small scale size of the waves. For case (C), $|\bar{\phi}_C|/|\phi_0|\sim 5\%$, which shows that waves with larger scale size contribute more to the fast-ion transport. The fast-ion transport in fully turbulent waves

(case (B)) is expected to be enhanced compared to that in coherent waves with the same scale size. Because of the short decorrelation length of the turbulent structure, fast-ion guiding-center $E\times B$ drift in turbulent waves is more stochastic. A rough estimate by calculating the averaged $|\bar{\phi}_B|$ in potential fields with $m=5-9$ shows that $|\bar{\phi}_B|/|\phi_0|\sim 0.2\%$, which is larger than $|\bar{\phi}_A|/|\phi_0|$ and is consistent to our expectation. The analysis above indicates that the scale size (or average mode number $\bar{m}$) of the waves is the major influence factor on the gyro-averaging effect, while turbulent waves induces more fast-ion transport than coherent waves when $\bar{m}$ is about the same for the two cases. This agrees well with the experimental results.

4.3 TIME DEPENDENCE OF FAST ION DIFFUSIVITY IN WAVES

4.3.1 Observed transition from super-diffusive to sub-diffusive transport

The perpendicular diffusivity ($D_\perp$) of the fast-ion beam in background electrostatic wave fields is generally space and time dependent. In our analysis, the spatial dependence of $D_\perp$ is neglected because the turbulent wave structures observed in this experiment have a parallel wavelength much longer than the axial distance travelled by a fast-ion ($\lambda_{||}\sim 15\text{m}$, while the maximum axial distance a fast-ion travels is ~1.27m). Thus the background wave structure is approximately flute-like, and $D_\perp$ only depends on the fast-ion time-of-flight in waves. The time-dependence of the fast ion beam diffusivity can be generally written as $D_\perp \propto t^\gamma$. In diffusive transport, $D_\perp$ is independent of time and $\gamma = 0$. Transport with $\gamma > 0$ is described as super-diffusive, while transport with $\gamma < 0$ is sub-diffusive. In the current experiment, the modification of the fast-ion gyro-radius due to its energy change can be neglected, as discussed above. Thus the time variation of the collected beam FWHMs directly reflects the transport of the fast-ion gyro-centers. Two important characteristic time scales[15] decide the nature of the fast ion diffusivity in low-frequency electrostatic waves: the wave-particle decorrelation time (τ_c), and the time scale for the waves to change their phase (τ_{ph}). Here, $\tau_{ph}\sim \bar{L}_s/v_{dr}$ is defined as the phase changing scale time of the wave structures, where $\bar{L}_s$ is the averaged azimuthal potential scale length, and v_{dr} is the wave azimuthal phase velocity. In coherent waves, τ_{ph} is comparable to half of the wave period (π/ω). Since the fast ion cyclotron frequency is much larger than any of the wave timescales, τ_{ph} is also the amount of time that a fast ion samples the same phase of the wave. When the fast ion time-of-flight in the waves is short ($T_f \ll \tau_{ph}$), the background wave can be treated as a static potential field, and the fast ions sample the same wave fields during every gyro-orbit. The collective beam transport is then super-diffusive, with diffusivity linearly growing with time ($D_\perp \propto t$). When $T_f \sim \tau_{ph}$, sub-diffusive transport is expected: The

fast ion starts to sample different phases of the wave potential, and $D_\perp$ decreases with time. Diffusive transport ($D_\perp = \text{const}$) only happens when the fast ion orbit is fully decorrelated with the initial wave field ($T_f > \tau_c$) and its motion in the waves becomes stochastic.

The time dependence of the fast-ion transport in drift waves associated with a plate obstacle was discussed in Chapter 3. Super-diffusive (ballistic) transport was observed, since the fast-ion time-of-flight in the waves was much shorter than any of the wave time scales. In other words, long-time wave-particle interaction was not achieved. In the experiment described in this chapter, the ion gun and collector are operated in a slightly different manner so that the fast ion beam samples the waves for a longer time. The axial distance of fast ion travelling in the waves is limited by the distance between the ion gun and the obstacle (~1.5m). However, the wave-particle interaction time can be varied by increasing the pitch angle of the ion beam while keeping ρ_f a constant (Fig. 4.12). Since the fast ion cyclotron frequency (Ω_f) is constant, the time-of-flight of the fast ion before it is collected is

$$T_f = \frac{L}{v_z} = \frac{L}{\sqrt{2E_\perp / M_{Li^+}}} \tan(\theta_{pitch}), \quad (4.2)$$

Where L is the total axial distance between the ion gun and collector, and θ_{pitch} is the pitch angle of the fast ion beam. The fast ion perpendicular energy is kept constant at $E_\perp = 320\text{eV}$, (with $\rho_f = 5.7\text{cm}$) so that the beam trajectories always overlap with the same wave field. By operating the gun at higher pitch angles (up to $\sim 80^\circ$), the fast ion time-of-flight in the waves is greatly extended. Table 4 lists typical values of the fast-ion beam parameters in several cases (with 4-22 cyclotrons) under this configuration.

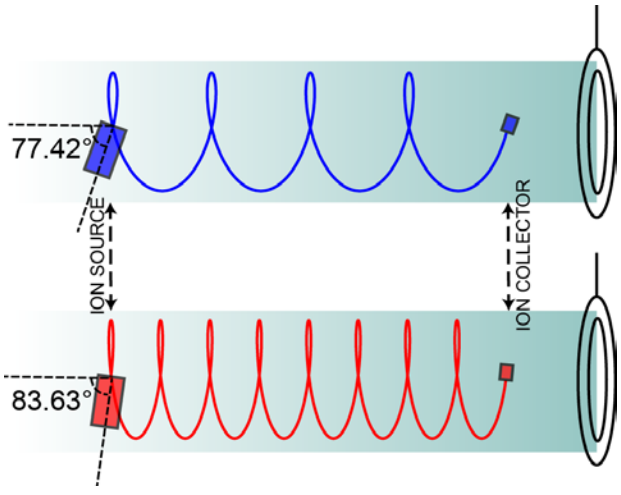

FIG. 4.12 Schematic of the ion source and collector setup for two cases with different fast-ion time in the waves. (a) $T_f = 4\tau_{ci}$, (b) $T_f = 8\tau_{ci}$

Avg # of Cyls	Pitch angle (degree)	gyro radius (cm)	Time-of-Flight (μs)
4	48.2	5.7	15.3
10	70.4	5.7	38.2
16	77.4	5.7	61.1
22	80.8	5.7	84.0

Table 4. Typical values of the fast-ion beam parameter with different number of cyclotrons

Fast ion beam profiles with the averaged number of gyro-orbits $\bar{n}_{gyro} = 4 \sim 22$ are obtained in helium plasmas with the annular obstacle floating. The fast-ion gun is located at port 35, while the collector is at port 31. The axial distance between the gun and the collector is fixed at 128cm. wave parameters in this data set are listed in Table 3 (case (D)). Notice that with the same experimental setup as case (A), the drift waves have the same azimuthal scale length, but are more broadband in this case (Fig. 4.13). This is possibly due to varied plasma conditions at different experimental run times, since a newly conditioned cathode was installed in the LAPD before this run.

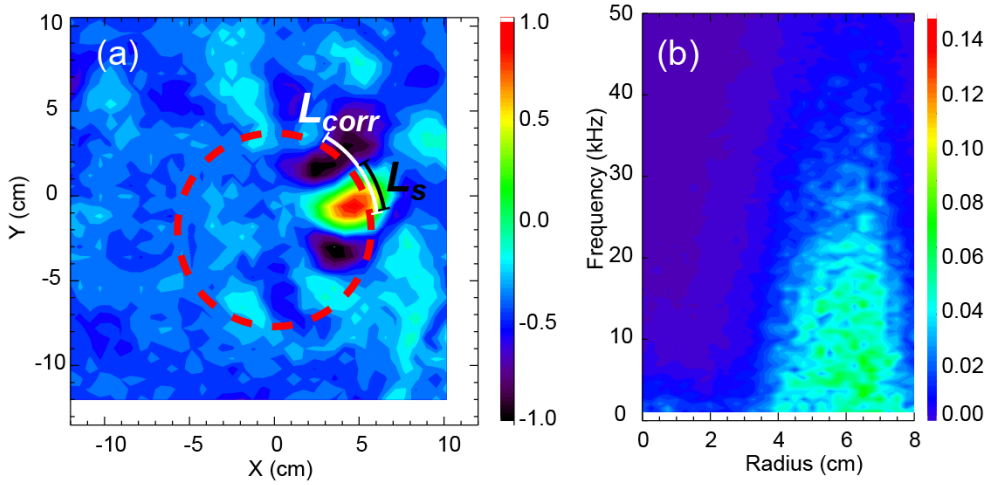

FIG. 4.13 (a) Two-dimensional cross-field correlation function for I_{sat} in case (D). (b) Contour of the spatially resolved wave spectrum for this case.

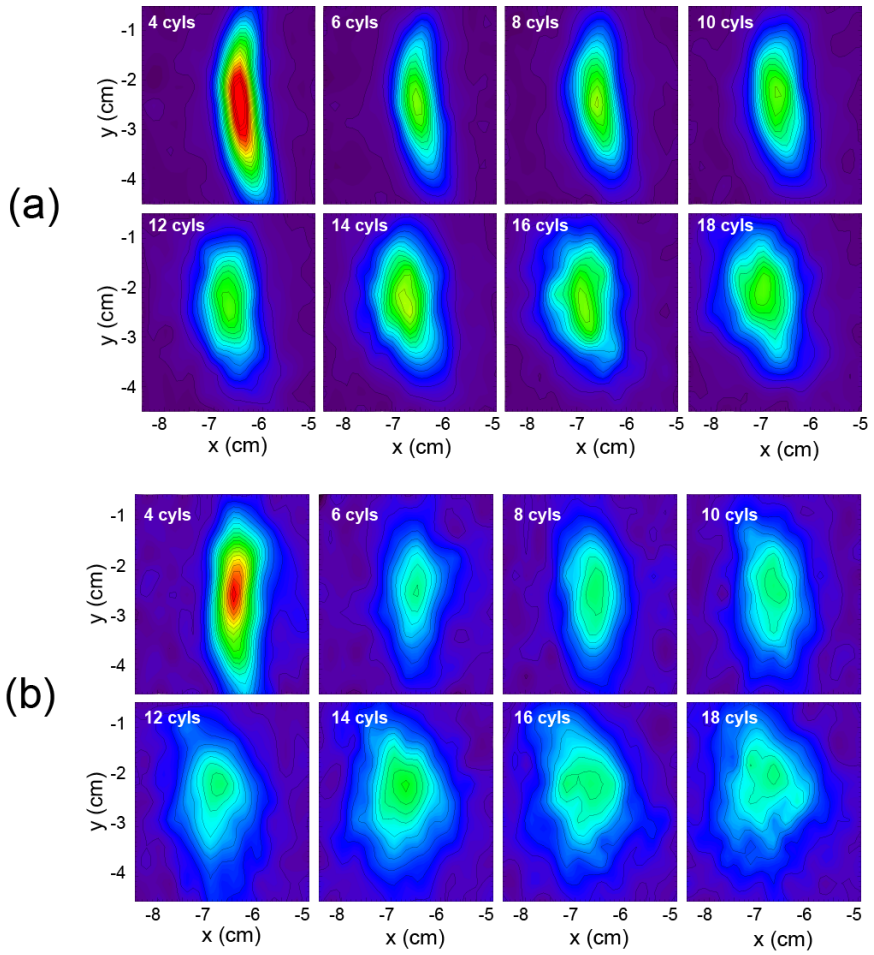

FIG. 4.14 Contour plot of the collected beam signal 4 ports away from the source in helium plasmas for (a) afterglow, (b) active phase with no bias (case (D))

Figure 4.14 shows the Contour plot of the collected beam signal 4 ports away from the source in helium plasmas for (a) afterglow, (b) active phase with V_{bias}=100V(case (D)). Beam FWHMs both in the active discharge and in the afterglow are obtained. In addition, beam profiles with no obstacle in the plasma are also measured, for which the classical transport dominates. Both the beam FWHMs in the afterglow plasma and with no obstacle agree well with the simulated classical prediction of the MC code. However, in active-phase plasmas with large fluctuations, the beam FWHMs exceed classical levels (Fig. 4.15). To quantify the fast-ion diffusivity, the beam $FWHM^2$ is plotted against T_f, with the classical transport effect subtracted (triangles in Fig. 4.16).

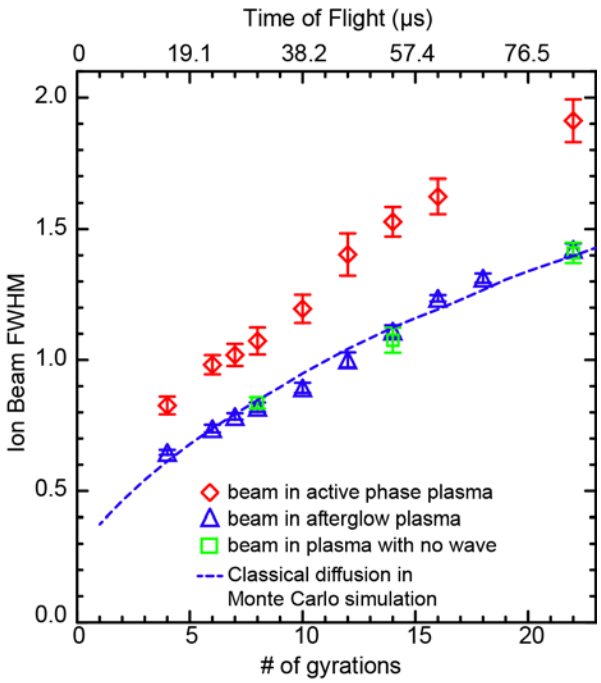

FIG. 4.15 Fast-ion beam FWHM versus number of gyro-orbits in active discharge (diamonds), afterglow (triangles) and with the obstacle removed (squares). Beam FWHMs both in afterglow plasma and with obstacle removed indicate classical transport effect, and agree well with the Monte-Carlo simulation result. Beam FWHMs in active discharge reflect both classical and wave-induced transport.

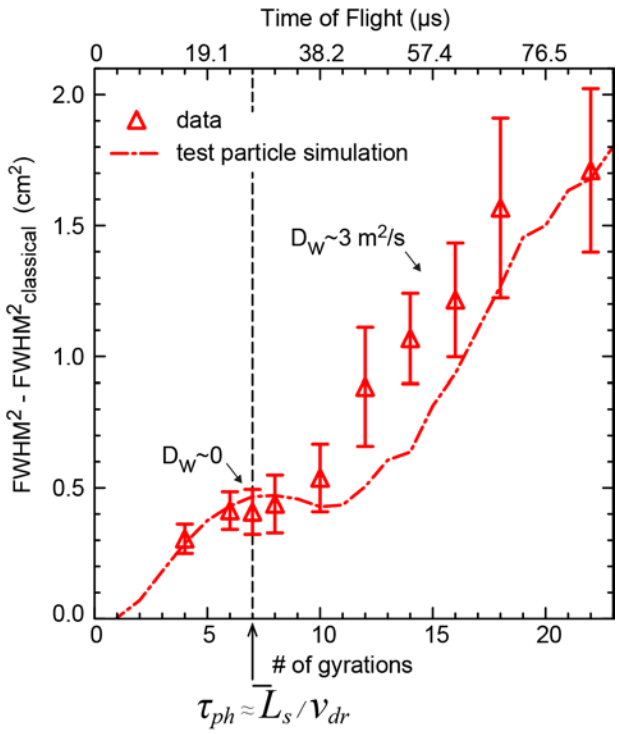

FIG. 4.16 Spatial-temporal evolution of the fast-ion beam (FWHM^2-FWHM$^2_{classical}$) versus number of gyro-orbits for case (D). Data are collected with the collector at port 31 (triangles). A test-particle simulation result (red dash-dotted line) agrees well with the data.

Since the fast ion gyro-period τ_{ci} is a constant, the fast-ion time-of-flight in the waves is also proportional to the number of gyrations it travels ($T_f = n_{gyro} \cdot \tau_{ci}$). The beam widths satisfy

$$W^2_{FWHM} - W^2_{classical} = 2\int_0^{T_f} D_W \, dt \,, \qquad (4.3)$$

where W_{FWHM} is the beam FWHM in waves, $W_{classical}$ is the beam FWHM due to classical transport, and D_W is the fast-ion perpendicular diffusivity in waves. When plotted versus time, the slope of $(W^2_{FWHM} - W^2_{classical})$ indicates the amplitude of D_W due to wave-particle interaction. A clear flattening in the data occurs for a gyration number of 6-8 and $T_f \sim 25\mu s$. This indicates that $D_W(t)$ has a significant drop (in Fig 4.16, $D_W(t) \sim 0$ at $\sim 25\mu s$) with time and the transition from super-diffusive to sub-diffusive transport occurs. The time scale for transport to be sub-diffusive is estimated as $\tau_{ph} \sim \bar{L}_s / v_{dr} \sim 26\mu s$, which agrees well with the observed sub-diffusive time scale.

4.3.2 Test particle simulation results

Monte Carlo test-particle simulation results clearly predict that the sub-diffusive transport due to wave phase variations should be observable. Firstly, a single particle gyro-center (GC) position is followed in measured wave fields for 12 gyro periods (Fig. 4.17).

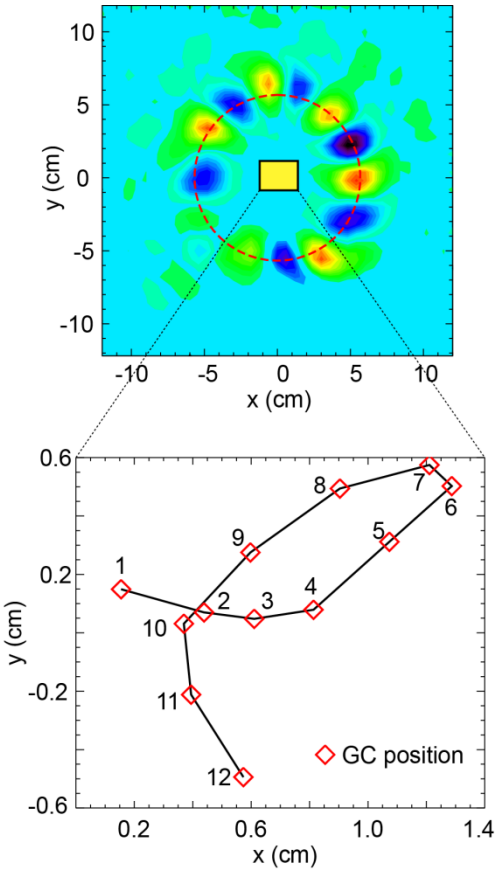

FIG. 4.17 Simulation of the gyro-center drifts of a single particle during 12 gyro-periods in experimentally obtained wave structures.

The time-dependent wave structures used in this simulation is inferred by the measured cross-field correlation function of the I_{sat} signal, and normalized to the maximum potential fluctuation amplitude. GC motion is initially ballistic (for $n_{gyro} \le 4$), drifting in the same direction with nearly constant step length during each gyro-orbit. This indicates that when the fast ion orbit samples approximately the same wave phase, the corresponding beam transport is super-diffusive. At $n_{gyro} > 4$, phase changes of the background potential due to the diamagnetic and $E \times B$ drifts start to affect the particle trajectory, induces a backward GC drift, and the corresponding beam transport becomes sub-diffusive. A full simulation of the same effect is performed by following 50000 test particles with random initial wave phases. The simulated beam FWHMs (dash-dotted line in Fig. 4.16) are normalized (to the maximum FWHM observed in experiment) and compared with experimental data. Flattening of $(W_{FWHM}^2 - W_{classical}^2)$ is also seen in the simulation, at the same time scale as the experimental result. This result agrees well with the theoretical explanation for sub-diffusive transport.

4.4 EFFECT OF THE STATIC RADIAL ELECTRIC FIELDS ON THE FAST ION BEAM

In this experimental setup, besides the interaction of the fast-ion beam with the turbulent wave fields, the fast ions are also affected by the static radial electric fields (E_r) induced by the bias on the annular obstacle. The fast ion beam gyro radius ($\rho_f = 5.7\text{cm}$) is set to be smaller than the inner radius of the annular obstacle (~6 cm), so that the fast ion beam trajectory avoids the sharp gradient (with a scale size $L_{\nabla\phi} \sim 0.5\text{cm}$) in plasma potential while still interacting with the potential structures ($L_{\tilde{\phi}} \sim 5\text{cm}$). The observed effect of the radial static electric fields on the fast-ion beam is mainly a convective drift of the beam center. Figure 4.18 shows the beam profiles collected 2 ports away from the source in helium plasmas when the bias on the obstacle is either off or on (V_{bias}=100V). It is observed that, during the pulse-bias time, the center of the beam drifts in the -r direction, with a displacement of ~ 5mm.

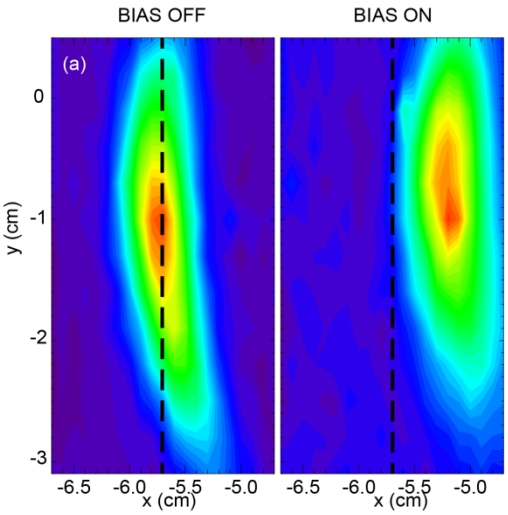

FIG. 4.18 Observed radial displacement of a fast-ion beam profile 2 ports away from the ion source during the bias time (V_{bias}=100V) of the obstacle in helium plasma.

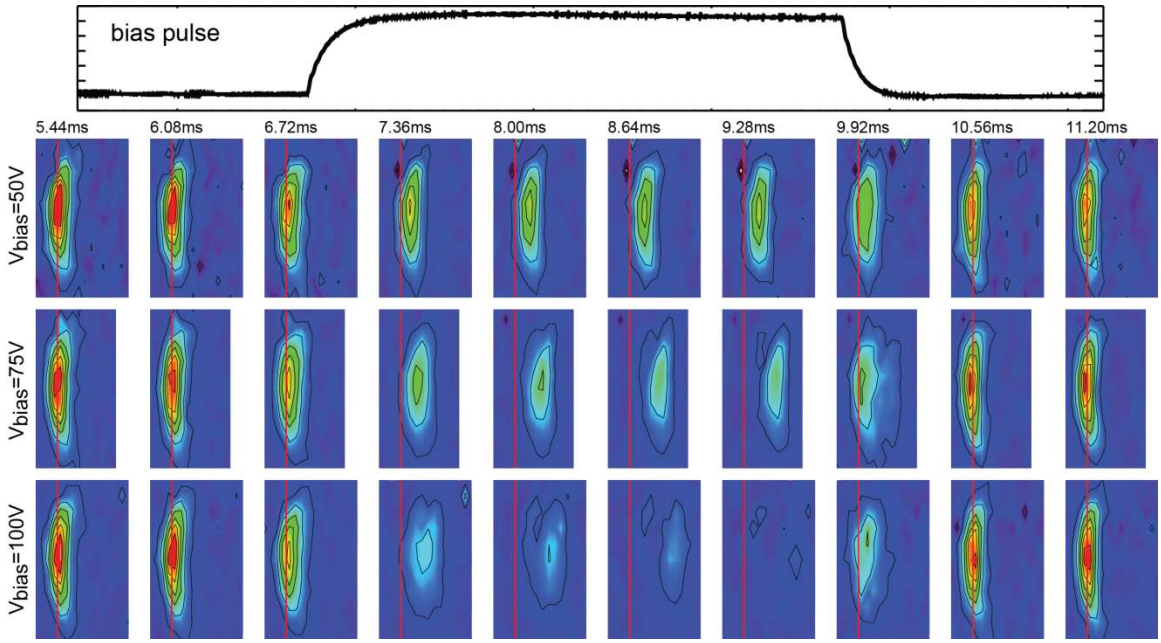

FIG. 4.19 Experimentally observed beam convective drift in cases with different obstacle bias (50V, 75V, 100V) in neon plasmas

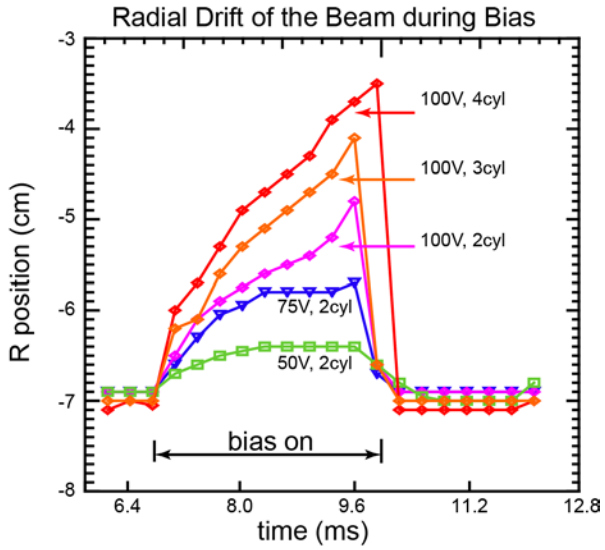

FIG. 4.20 The temporal evolution of the radial positions of the beam center in several typical cases

Drifting of the centroid is often observed. These drifts occur both in time (in a single discharge as plasma conditions change) and in space (at the same time in the discharge at different distances from the source). Figure 4.19 shows the temporal evolution of the beam during three typical cases with different bias voltage on the annular obstacle. The beam is collected after finishing two cyclotron orbits. It is observed that, during the pulse-bias time, the center of the beam is drifting in the -r direction. The drift is mainly convective for low

bias voltage (50V-75V), but degrades the beam for high bias voltage (100V). The evolution of the beam radial position for several cases is plotted in Fig. 4.20. Empirically, the magnitude of the drift tends to increase with increasing annulus bias, and increases with distance from the source. With a lower bias voltage (e. g., 50V and 75V in neon plasma), the radial displacement of the beam center reaches a steady value during the pulse time; with high bias voltage (100V in neon plasma), the radial displacement increases with time during the pulse. The different behaviors at different bias voltages are associated with the time evolution of the plasma conditions during the pulse time: with low bias voltage, the plasma density and potential profiles are in quasi-equilibrium while, with high bias voltage, a vast depletion in plasma density is usually observed. Evolution of the plasma conditions during various bias voltages is discussed in detail in Chapter 5.2.

In general, both radial and azimuthal drifts are observed. The direction and magnitude of the drift is sensitive to the alignment of the orbit relative to the annulus. Motion of the centroid also can occur in the absence of a biased plate. For example, the beam centroid often moves ~5 mm at the transition between the active phase of the discharge and the afterglow phase. The jump at this transition is sensitive to the electrical configuration of the ion source housing, with a different response depending on whether the gun is floating or grounded. All of these phenomena are consistent with the idea that static electric fields cause convective drifts.

The effect of a static E_r fields on the fast ion orbits can be studied analytically. Assuming the radial displacement of the ion $\delta r << \rho$, where ρ is the gyroradius of the fast ion, the equation of motion of a single fast ion is

$$m\frac{d^2\vec{r}}{dt^2} = q(\vec{E} + \vec{v}\times\vec{B}), \text{ with } \vec{r} = \vec{\rho} + \delta\vec{r}, \omega = \Omega + \delta\omega \quad (4.4)$$

Here Ω is the fast-ion gyro frequency. Consider the case of an orbit that is concentric with a biased annulus. By symmetry, the electric field is only in the radial direction; thus $E_\theta = 0$. The equation of motion in the radial direction is

$$\delta\ddot{r} = \frac{e}{m}E_r - \Omega^2\delta r \quad (4.5)$$

If E_r is a constant, the equation has a simple analytical solution of the form

$$\delta r = (eE_r / m\Omega^2) + A\sin(\Omega t + \varphi), \quad (4.6)$$

which is a sinusoidal oscillation at the fast ion gyro frequency. For a more complicated electric field, such as the experimental plasma potential and E_r profiles during the bias time, a numerical solution of Eqn. (4.5) can be derived.

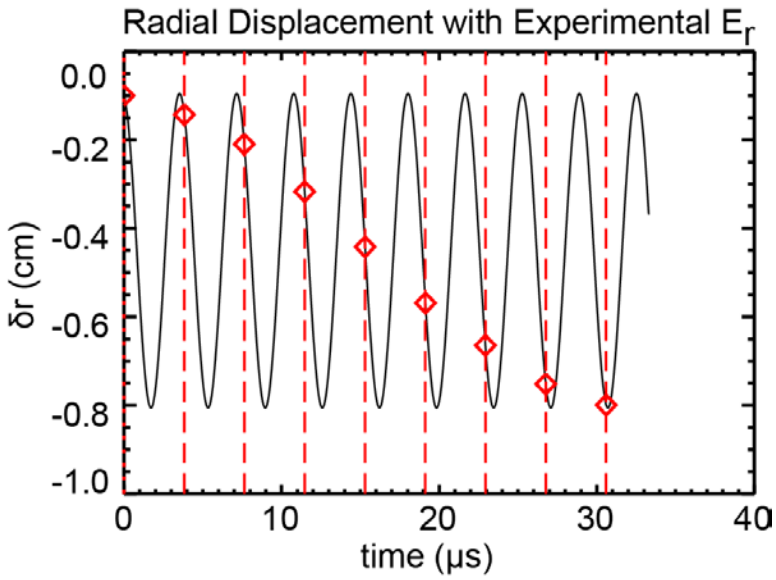

FIG. 4.21 Numerical solution of the particle radial displacement under the effect of the static radial electric field. Red diamonds are the particle radial displacement at the end of each cyclotron motion.

Figure 4.21 shows the numerical solution of the fast-ion radial displacement as a function of time under the measured equilibrium plasma potential with 75V obstacle-bias voltage in neon plasmas. The red dashed lines mark the end time of each fast-ion cyclotron motion. As the experimental profile of E_r is non-uniform, the radial oscillation frequency of the fast ion diverges from the cyclotron frequency Ω. The displacement of the fast ion in the -r direction at the end of each cyclotron motion increases with the number of gyrations. This indicates that the radial motion of the particle is precessing in these non-uniform electric fields. This result agrees with the observed tendency of the drift to increase approximately linearly with distance from the source (Fig. 1(b)). The numerically solved displacement scale length (~1cm) also agrees with the observation.

Due to the finite radial width of the fast-ion beam and the non-uniform fields, not all particles experience the same drift. Hence, the collective effect of the static electric fields on the beam spot is not fully convective. Broadening of the beam radial FWHM can result from the static fields as well. This is a source of error in the study of beam broadening due to the turbulent waves. To evaluate the effect of the static fields on the beam FWHM, a Monte-Carlo simulation is carried out. Equilibrium profiles of plasma potential in an experimental case (neon plasma with 75V bias) are imported to a Monte-Carlo particle following code as the background fields. The radial drift and broadening of 50,000 test particles are evaluated. Furthermore, since the misalignment between the fast ion beam orbit and the annular obstacle can also modify the effect of the radial fields, a sensitivity study is also conducted to quantify the effect of the static fields under several conditions with the beam orbit misaligned with the inner edge of the obstacle.

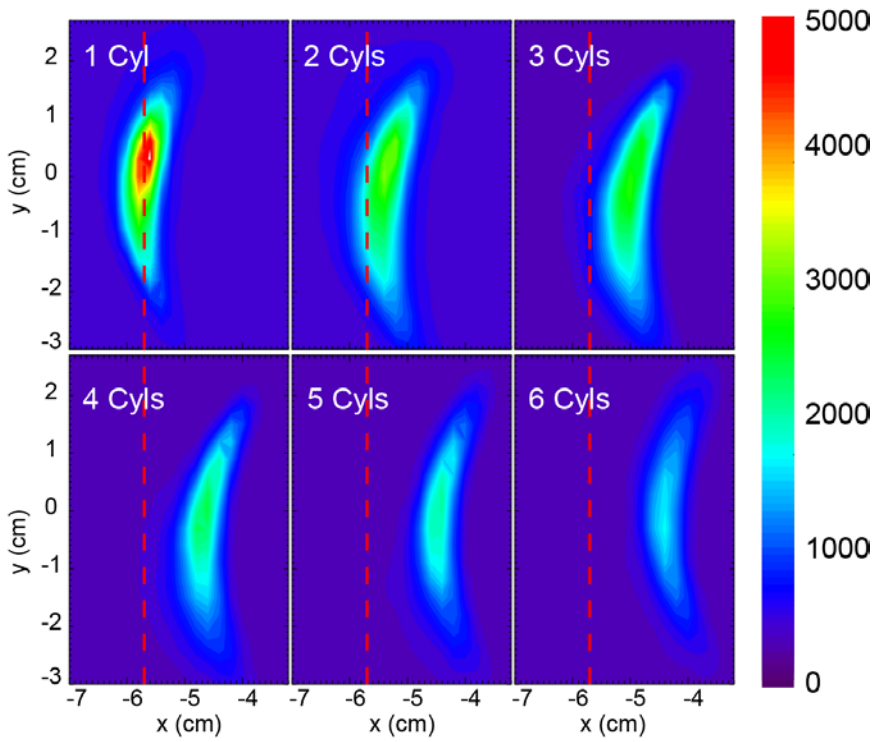

FIG. 4.22 Radial drift of the collected beam profiles at 1-6 gyrations, observed in a Monte-Carlo simulation with experimental profile of plasma potential and 50,000 test particles.

The beam profiles collected at 1-6 cyclotrons are shown in Fig. 4.22. A radial convective drift of the beam center is clearly shown in the simulation, with a typical value of ~1cm after 6 gyrations. This is consistent with the amount of drift observed in the experiment. Note that the decrease in total number of particles in the simulation is mainly due to azimuthal spreading of the beam. (The simulation includes the instrument function of the collector, so ions that drift outside of the collector acceptance angle are considered lost.) The radial positions of the fast-ion beam in several cases with different alignment conditions are shown in Fig. 4.23. In the well-aligned case (black), the radial displacement of the centroid is ~5mm, which is the typical value observed in experiment. The displacement clearly depends on the alignment. With a poor alignment between the beam orbit and the obstacle in x direction, the radial displacement can be ~1.5mm, which is comparable to the scale size of the wave potential structure. This means that the wave-particle interaction can be reduced due to the drift of the centroid. The broadening of the ion beam FWHMs in these cases are evaluated in Fig. 4.24. The beam $FWHM^2$s are plotted against the number of beam gyrations. The red dashed line indicates the classical diffusion level of the beam in neon plasmas, and the red triangles shows the observed beam $FWHM^2$ in experiment with large turbulent waves present. The diamond symbols represent a case with the fast ion orbit well aligned with the obstacle (centered), and four cases with them misaligned by ±5mm in either the x or y direction. It is indicated from Fig 4.23,24 that the static E_r induced transport is mainly convective, with radial displacement of ~1cm. It also

contributes to the broadening of the beam FWHM. However, wave-induced transport is still the dominant effect in the experimentally observed broadening of the fast-ion beam.

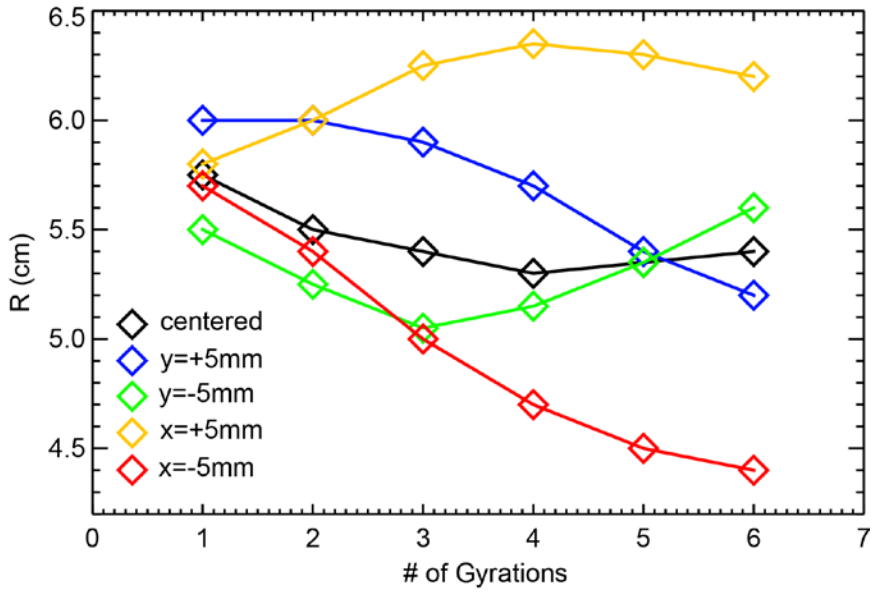

FIG. 4.23 Simulated radial position of the beam center versus number of gyrations. Misalignment between the beam orbit and the annular obstacle in both x and y directions are simulated.

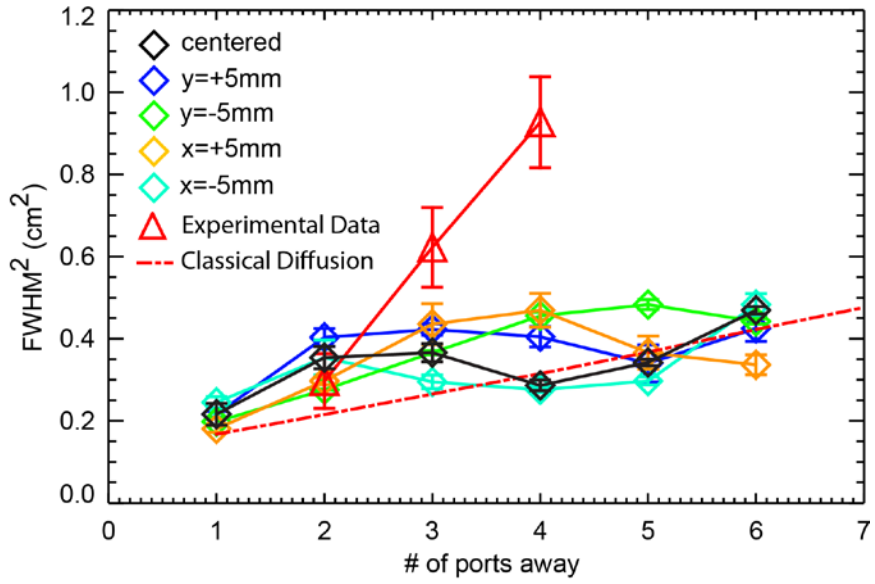

FIG. 4.24 Simulated broadening of the beam FWHM due to the static radial electric fields. The observed beam width (triangles) and classical diffusion level (dash-dotted line) are plotted for comparison.

With higher bias (≥100V) on the annular obstacle, the collected beams usually drift more radially and are degraded substantially, so that a quantitative measurement of the beam radial FWHM is difficult. Specifically, in cases with high V_{bias} and poor alignment between the beam orbit and the obstacle, a "split" of the collected beam profile is usually observed.

Figure 4.25(a) shows a typical "split" beam profile, observed at 100V obstacle-bias in neon plasmas. The split of the beam profile is mainly induced by the overlap of the beam with the peak in the radial electric field profile. Splitting of the beam profile is also observed in Monte Carlo simulations. Figure 4.25(b) shows a typical simulation result for a potential profile with sharp gradient. The radial electric field is plotted in dash-dotted lines, and the initial beam is misaligned with the E_r fields by 5mm. A "split" beam profile similar to the experimental one is observed.

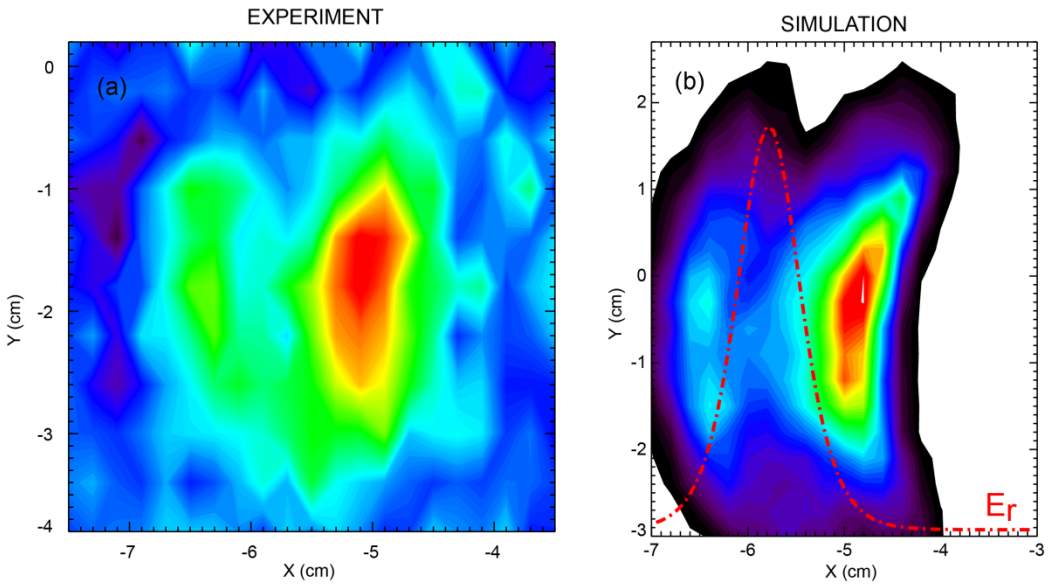

FIG. 4.25 Beam split observed in experiment (a) and in simulation (b). The split of the beam is correlated with sharp gradient in plasma potential, and misalignment of the beam to the potential fields.

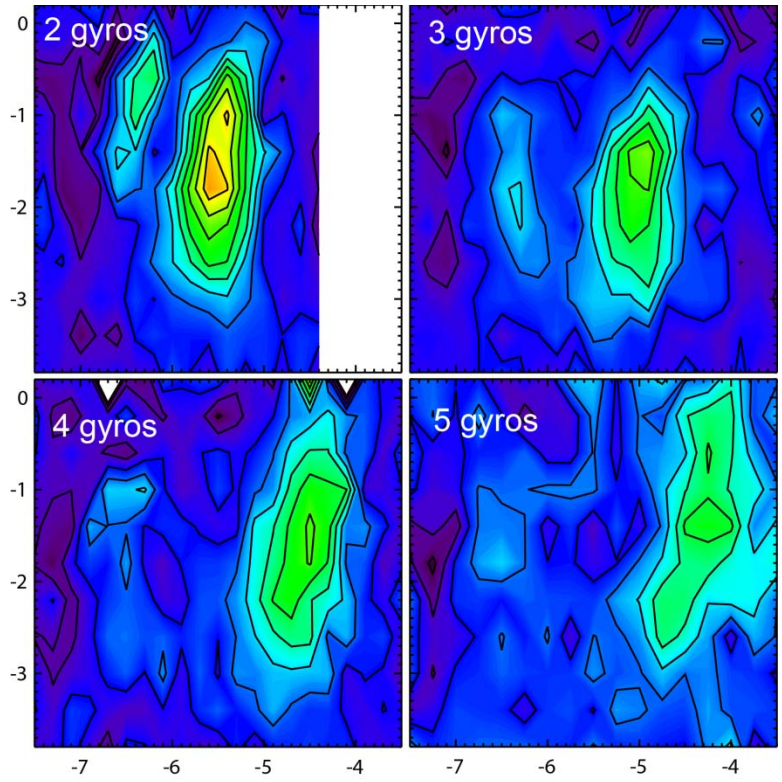

FIG. 4.26 Contour plot of the collected beam signal 2-5 ports away from the source in active-phase neon plasmas with V_{bias}=100V

The centroid drift and split of the fast-ion beam leads to additional complicity in the analysis of the collected beam data with V_{bias}=100V in neon plasmas. Figure 4.26 shows the contour plot of the collected beam at 2-5 gyrations away from the source. Analysis to quantify the wave induced broadening in this dataset is difficult for the following reasons: (1) The radial drift of the beam is ~3cm in 5 gyrations (the beam spot with no bias is located at r~-7cm), which is comparable or larger than the typical scale length of the wave potential structure, thus the overlap and interaction between the fast ion orbit and the wave is poor. (2) The split of the beam makes it difficult to accurately quantify the FWHM of the beam. (3) In neon plasma with V_{bias}=100V, the plasma is not in a steady state. Depleting in plasma density and damping of the turbulent wave happens during the 3-ms pulsed bias time (see Chapter 5.2.1 and Fig. 5.13 for detail). Thus the effect of the background turbulence on the fast ion transport is difficult to quantify.

The drift of the ion beam due to the static electric fields is unfavorable for studying the wave-induced, diffusive transport of the ion beam. Running the ion beam with a smaller gyro-radius to avoid the large plasma potential gradient regime is a possible method to minimize the effect of the static field. However, the gyro-radius of the beam has to be carefully chosen so that the beam trajectories are still able to overlap well with the mode structures of the waves.

4.5 CONCLUSIONS

In this experimental work, turbulent waves associated with large density gradients and drift flow shear is observed. Direct measurement of fast ion non-classical spreading in the background waves quantifies the fast-ion cross-field transport due to interaction with low-frequency electrostatic wave potential fields. The background wave characteristics are modified by switching the working gas from helium to neon, and by altering the biasing voltage on the annular obstacle. Fast ion beam spreading in several typical cases shows that waves with larger spatial scale size (smaller mode number) cause more fast-ion transport; and with similar potential scale size, the coherent waves cause less fast-ion transport than turbulent waves. The difference in fast-ion transport is well explained by gyro-averaging effect: The averaged wave potential fluctuation amplitude is reduced due to the large fast-ion orbits, and the averaging effect depends on the coherency and structure scale sizes of the waves. When the fast ion interacts with the wave for most of a wave period, a transition from super-diffusive to sub-diffusive transport is observed, as predicted by diffusion theory. Simulation results of a Monte-Carlo particle following code show good agreement with the experimental data.

Chapter 5

SHEARED-FLOW INDUCED CONFINEMENT TRANSITION OF THERMAL PLASMAS IN LAPD

5.1 EXPERIMENTAL SETUP

This experiment was performed in plasmas generated in the upgraded Large Plasma Device (LAPD) at the University of California, Los Angeles. The experimental setup is similar to the one described in Chapter 4.

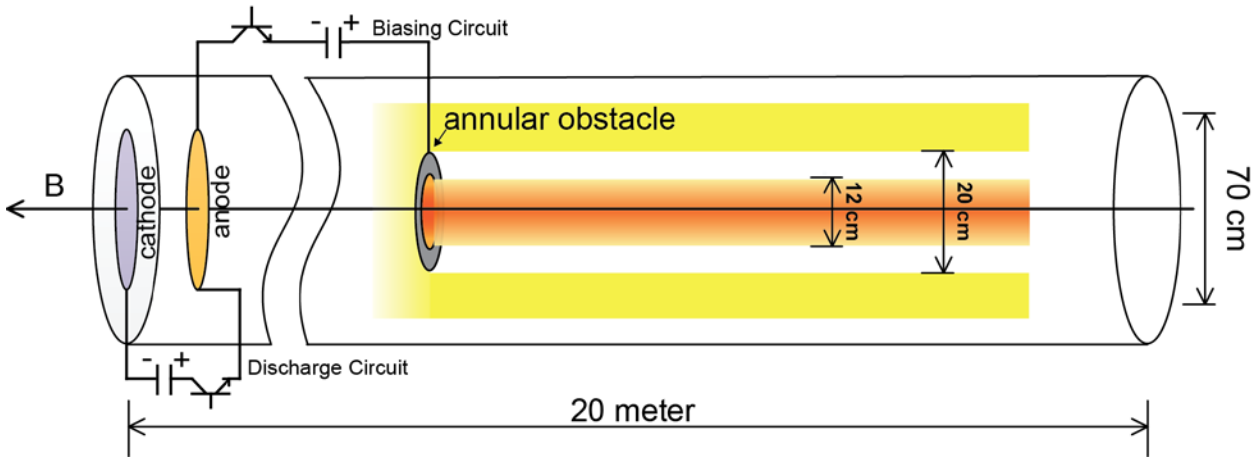

FIG. 5.1 (color online) Schematic of LAPD including the annular obstacle and the biasing circuit. The annular obstacle blocks the ionizing fast electrons generated during the cathode-anode discharge, and forms a plasma column with 12cm diameter downstream.

The working gases used in this experiment are helium and neon. The experimental setup is shown schematically in Fig. 5.1. A copper, annular obstacle is inserted concentrically in the main plasma. The obstacle has inner diameter of 12 cm and outer diameter of 20 cm. Downstream from the obstacle, a plasma column with diameter of 12 cm and steep edge density gradient is formed. The obstacle shaft and the LAPD anode are connected by a bias circuit including a capacitor bank and an IGBT (Insulated Gate Bipolar Transistor) switch. A pulsed bias with *~3ms* duration time is imposed on the obstacle during the steady portion of the LAPD discharge. The biasing voltage in this experiment is up to 250V, and it establishes radial electric fields and spins the edge of the 12cm-diameter plasma column through $E \times B$ drift. Figure 5.2 shows typical profiles of the plasma density n_e, root-mean-square (rms) of ion saturation current (I_{sat}) fluctuation and the plasma potential V_p, measured by Langmuir probes (described below) 0.3m downstream from the annulus when the bias voltage is 100V. Steep radial density and potential gradients are both localized at the inner edge of the obstacle (r ~ 6 cm), along with large I_{sat} fluctuation power.

In the region within r < 6 cm, the applied radial electric fields are shorted by the fast electron population, which ties the local plasma potential to the plasma source. Thus the effects of applied electric fields and sheared E×B flow are limited to the obstacle edge regions.

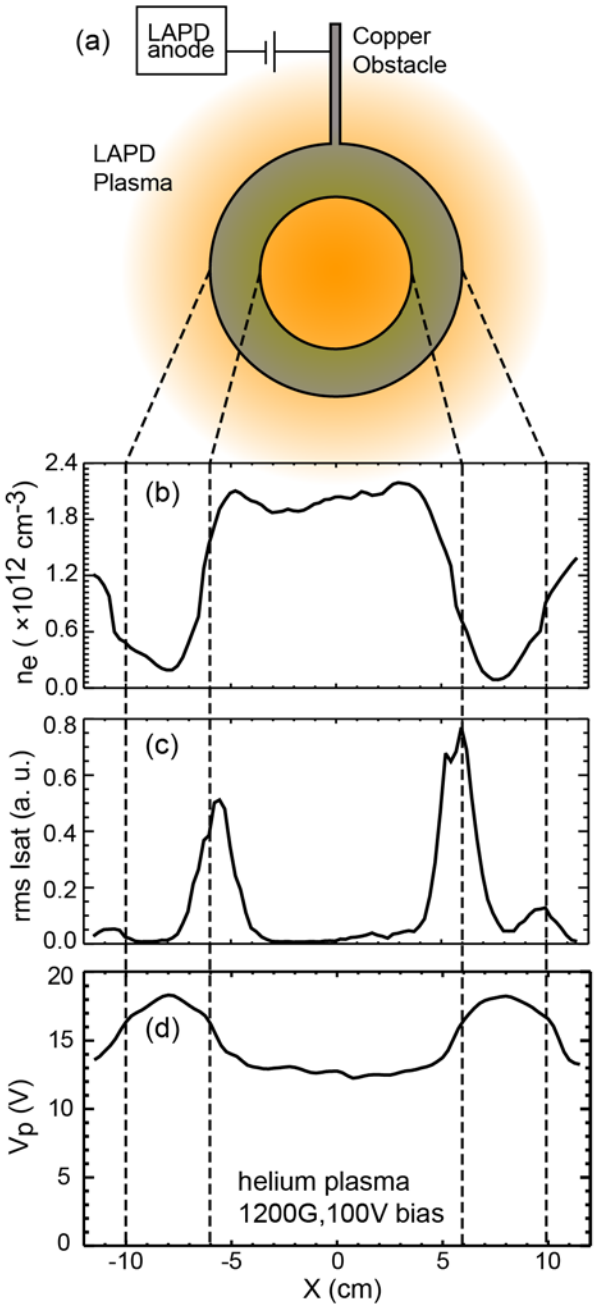

FIG. 5.2 (a) Schematic of the LAPD end-view. The copper obstacle can be biased relative to the LAPD anode by an external power supply. (b) Typical helium plasma density profile. (c) Typical root-mean-square (RMS) fluctuation of the ion saturation current. (d) Plasma potential profile 0.3m downstream from the obstacle when the obstacle is biased to 100V in helium plasma.

Measurements of density, potential, temperature and their fluctuations are made using Langmuir probes. A 3-tip probe is used as a triple Langmuir probe[49] to measure the fluctuations of ion saturation current ($I_{sat} \propto n_e\sqrt{T_e}$), floating potential ($V_f$) and electron temperature (T_e). A 65V bias is applied between two tips measuring I_{sat} to reject the primary electrons. A single-tip probe is also used as a swept Langmuir probe to measure the equilibrium profiles of plasma potential (V_p) and electron temperature. Two different methods are used to quantify the sheared flow profile. Firstly, the $E\times B$ drift velocity is calculated from the plasma potential profile measured by a swept Langmuir probe. Then, a Gundestrup (Mach) probe[51] with six faces is used to measure the flows directly in several bias voltages. Figure 5.3 shows the radial profiles of the flow velocity measured by both methods in helium plasma with 150V bias on the annulus. The flow velocity peaks at r = 6 cm and 10 cm, which aligns to the inner and outer edge of the annular obstacle. The peak velocity is comparable to the ion sound speed v_s with Mach number ~ 1 ($v_s \sim \sqrt{k_B T_e / M_i} \sim 1.1\times 10^6\,\mathrm{cm/s}$). The velocity profile measured by the Mach probe agrees with the calculated $E\times B$ drift. And the $E\times B$ drift velocity is much larger than the electron diamagnetic drift velocity ($v_{De} = (k_B T_e / eB_z)(n_0'/n_0) \sim 2\times 10^5\,\mathrm{cm/s}$).

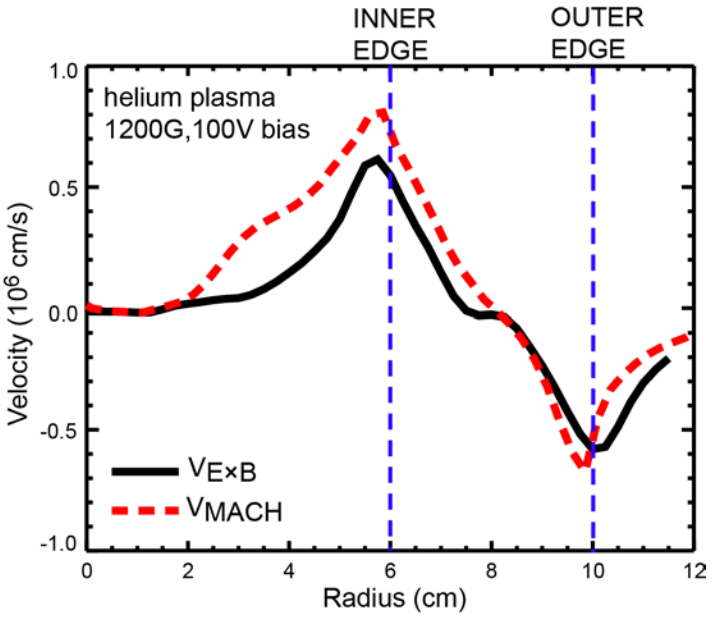

FIG. 5.3 (color online) Profile of plasma flow velocity measured by the Mach probe (red dashed line), and the $E\times B$ drift velocity profile (black solid line) calculated from the plasma potential (V_p) measurement of a swept Langmuir probe.

This suggests that the $E\times B$ drift dominates the plasma edge flow dynamics. The fluctuations of the magnetic fields are measured by a B-dot probe. A typical magnetic fluctuation level observed is $\delta B / B_z \le 0.1\%$, so the electrostatic approximation is assumed in all of the analysis below.

The relation between the external bias applied to the obstacle and the plasma potential (V_p) formed downstream of the obstacle is shown in Fig. 5.4(a), measured in neon plasmas with $B_z = 1200G$. The plasma potential profiles are measured by a swept Langmuir probe located 0.3m downstream of the obstacle. Then the V_p profiles are fit by a function of the form $A_2 + (A_1 - A_2)/(1 + e^{(x-x_0)/dx})$, where A_1, A_2, x_0, and dx are constants. The azimuthal $E \times B$ velocity and the shearing rate are derived from gradients of the fitted potential profiles. Profiles of the azimuthal velocity v_θ and the shearing rate γ (defined as $\gamma = \partial v_\theta / \partial r$) are shown in Fig. 5.4(b-c), with electron temperature profiles in Fig. 5.4(d). The peak plasma potential and the azimuthal drift velocity both increase with the bias on the obstacle. However, the shearing rate peaks at 50V-75V bias, while with 125V bias, the maximum of the shearing rate shifts radially inward significantly. The T_e profile is approximately constant with bias up to 75V, and increases by ~20% with 125V bias.

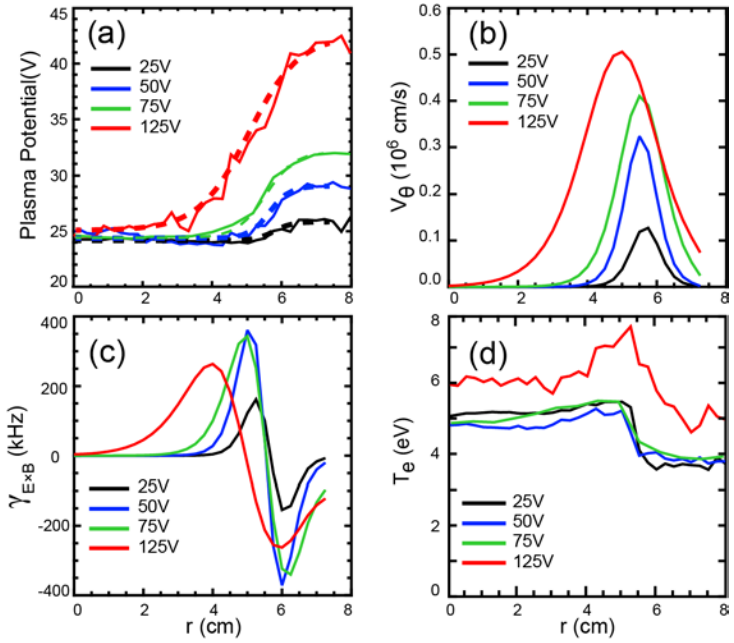

FIG. 5.4 (color online) Profiles of plasma potential with fit (V_p), azimuthal $E \times B$ drift velocity (v_θ), shearing rate ($\gamma_{E\times B}$) and electron temperature (T_e) for several bias values (neon plasma, $B_z = 1200G$). Measurement of V_p and T_e are made by a swept Langmuir probe, while v_θ and $\gamma_{E\times B}$ are calculated based on the fitted V_p profiles.

5.2 EXPERIMENTAL RESULTS

5.2.1 Overview

In this experiment, the plasma edge turbulence and the associated turbulent transport are modified in three different ways: (a) alter the bias voltage V_{bias} that is applied on the annular

obstacle (0V - 250V), (b) change the axial magnetic field strength B_z (600G-1800G) and (c) switch the plasma species (helium or neon). A previous study on the modification of the LAPD edge turbulence by biasing the vacuum vessel[38] shows that the amplitude and shearing rate of the edge flow are crucial parameters in the confinement transition. Studies of the gradient driven instabilities (e.g., the discussion of Fig. 4 in Ref. [25]) usually suggest that the scale size of the turbulent structure is proportional to the ion sound radius ρ_s. So, in this experiment, it is expected that the edge turbulence and transport are associated with both the azimuthal flow induced by the $E \times B$ drift and the value of ρ_s.

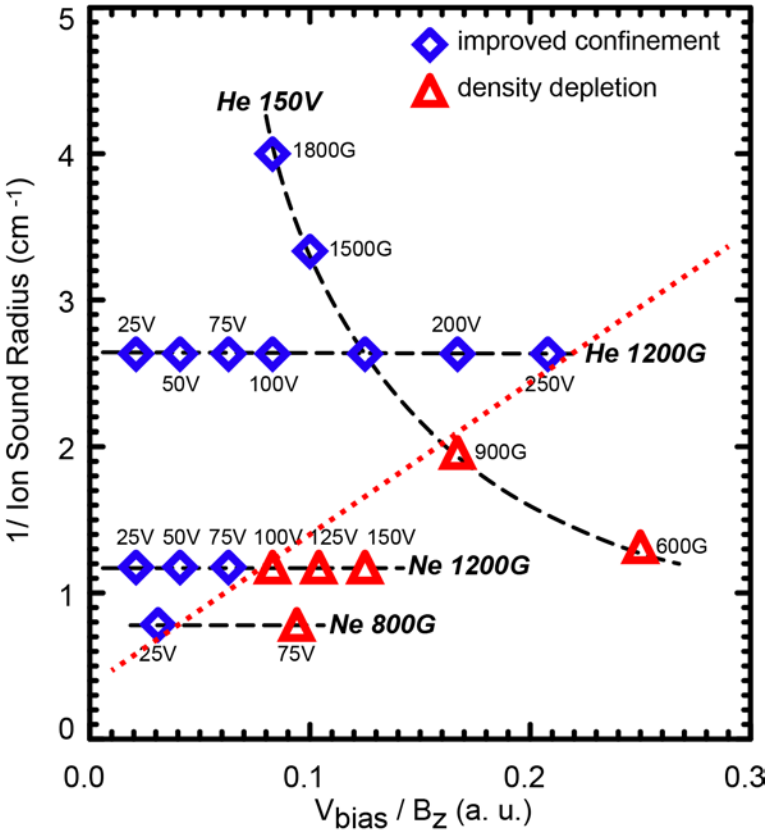

FIG. 5.5 Plot of all cases studied with control parameters marked. Horizontal axis indicates the direction of increasing flow velocity; vertical axis indicates the direction of decreasing ion sound radius (ρ_s). Dotted line is drawn to guide the eye. Cases with large radial transport and plasma depletion tend to be associated with large flow velocity and large ρ_s.

Figure 5.5 plots all the cases studied in this experiment in term of the values of (V_{bias}/B_z) and (ρ_s^{-1}), with control parameters (plasma species, V_{bias} and B_z) noted. The observed plasma characteristics can be categorized into two very different states: enhanced density confinement (blue diamonds) and density depletion (red triangles). Typical spatial-temporal evolutions of I_{sat} signals for both states are shown in Fig. 5.6(a, b). Comparison of

plasma density profile ($n_e \propto I_{sat} / \sqrt{T_e}$) before the end of the pulsed bias in these cases are shown in Fig. 5.7(a).

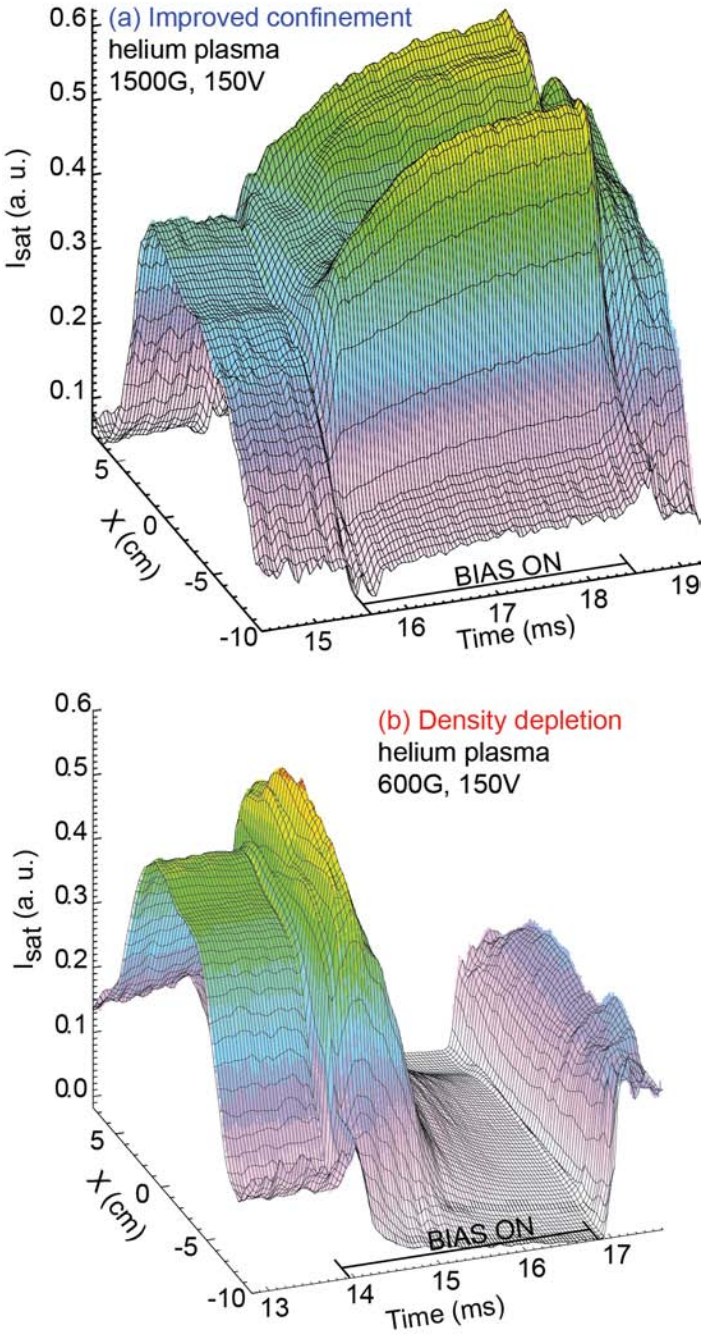

FIG. 5.6 (color online) Space and time resolved ion saturation current (I_{sat}) profiles in (a) a case of improved confinement, and (b) a case of plasma depletion.

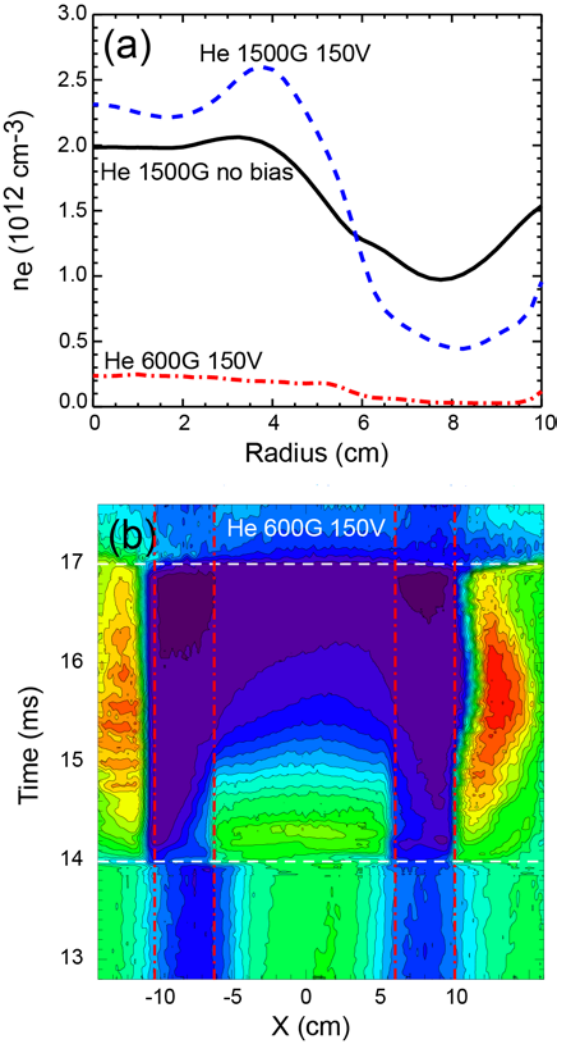

FIG. 5.7 (color online) (a) Density profiles ($n_e \sim I_{sat} / \sqrt{T_e}$) in cases with improved confinement (blue dashed line), plasma depletion (red dash-dotted line) and when the obstacle is floating (black solid line), with control parameters marked. (b) The contour of time and space resolved I_{sat} signal in helium plasma with $B_z = 600G$ and $V_{bias} = 150V$. The positions of the inner and out radius of the obstacle is marked (red dash-dotted lines). Outward density transport is indicated by the simultaneous evolution of the I_{sat} signal at the inner plasma column and the outer-edge plasma.

The plasma characteristics when no bias is applied to the obstacle (floating obstacle) is usually used for comparison. In cases with improved confinement (Fig. 5.6(a)), a much steeper edge density gradient, associated with increasing plasma density within the plasma column is observed. In helium plasma, the density growth is more significant at the edge region of the column; while in neon plasma, the density growth is larger near the center region. In cases with "density depletion" (Fig. 5.6(b)), the density of the plasma column transiently increases in the central region upon the application of the bias, then decreases rapidly during the remainder of the biasing pulse, becoming totally depleted in some cases.

Meanwhile, the density downstream of the obstacle outer edge ($r \geq 10\,\mathrm{cm}$ region) increases during the bias pulse, with the time sequence correlated to the depletion of the inner plasma column (Fig. 5.7(b)). This is observed in all cases with density depletion, suggesting that large cross-field transport happens in the radial direction during the biasing time. Overall, enhanced confinement cases are usually associated with smaller ρ_s and slower edge $E \times B$ flow velocity (upper-left in Fig. 5.5)), while density depletion cases are associated with larger ρ_s and faster edge $E \times B$ flow (lower-right in Fig. 5.5).

The density evolutions during the bias pulse for both states are also suggested by the high-speed camera imaging data (Fig. 5.8), which observes the visible light intensity from the end-window of the LAPD. Typical cases with improved confinement or density depletion are investigated. The evolution of the light intensity observed after the pulsed bias is applied (at ~0ms in Fig. 5.8) agrees with the I_{sat} data.

(a) helium 150V 1200G

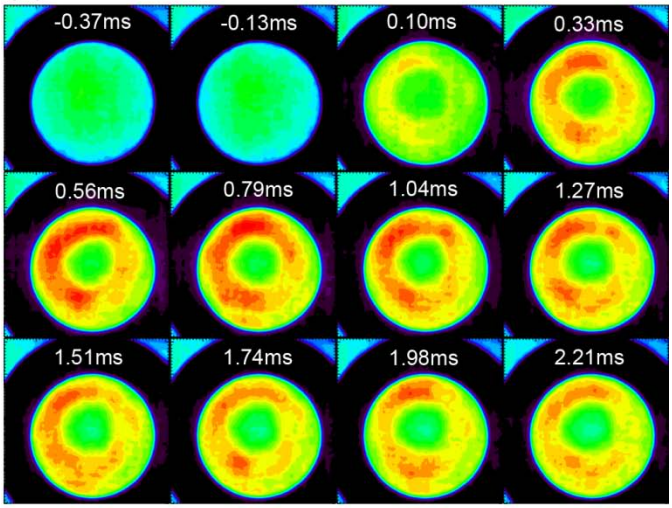

(b) helium 150V 600G

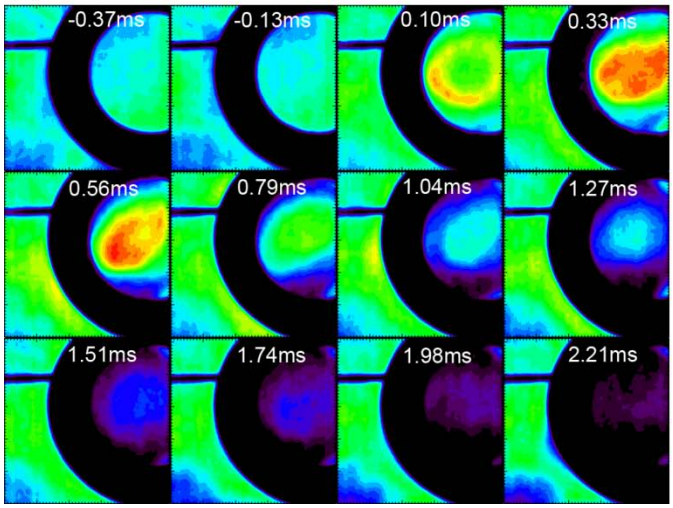

FIG. 5.8 Intensity of the visible light measured by the high-speed camera imaging for (a) improved confinement and (b) density depletion. The camera is located at the north end-window of LAPD and facing the cathode. The black annular region suggests the shadow of the obstacle. The obstacle bias pulse starts at *0ms.*

5.2.2 Confinement Transition and Radial Flux

To understand the transition from improved confinement to depletion of the plasma density, three sets of data are analyzed in detail: (a) in helium plasma with $B_z = 1200\text{G}$ and $V_{bias} = 25\text{V} - 250\text{V}$; (b) in neon plasma with $B_z = 1200\text{G}$ and $V_{bias} = 25\text{V} - 150\text{V}$; (c) in helium plasma with $V_{bias} = 150\text{V}$ and $B_z = 600\text{G} - 1800\text{G}$. To quantify the density evolution when sweeping the bias or the axial magnetic field, the averaged densities at the center region of the plasma column ($r \le 2\text{cm}$) are calculated from the I_{sat} measurement. Figure 9 shows the plasma densities $\bar{n}_{e,r\le 2\text{cm}}$, normalized to the density when no bias is applied on the annular obstacle. The no-bias case is used as a reference to minimize the uncertainty induced by changes in machine condition (such as the discharge power and the cathode condition) for data acquired at different run times. It is observed that in helium plasmas with $B_z = 1200\text{G}$ (Fig. 5.9(a)), the central density linearly increases with the applied bias. A similar density increase is also initially observed in neon plasmas, until the transition to large outward transport occurs at $V_{bias} \sim 100\text{V}$ (Fig. 5.9(b)). The confinement transition correlates with the scale length of the ion sound gyroradius ρ_s. For the same edge biasing ($V_{bias} \ge 100\text{V}$) and field ($B_z = 1200\text{G}$), the confinement transition happens in neon plasma (with $\rho_s = 0.85\text{cm}$), but not in helium plasma (with $\rho_s = 0.38\text{cm}$). In helium plasmas, the confinement transition happens when $B_z \le 900\text{G}$ (Fig. 5.9(c), $\rho_s \ge 0.51\text{cm}$).

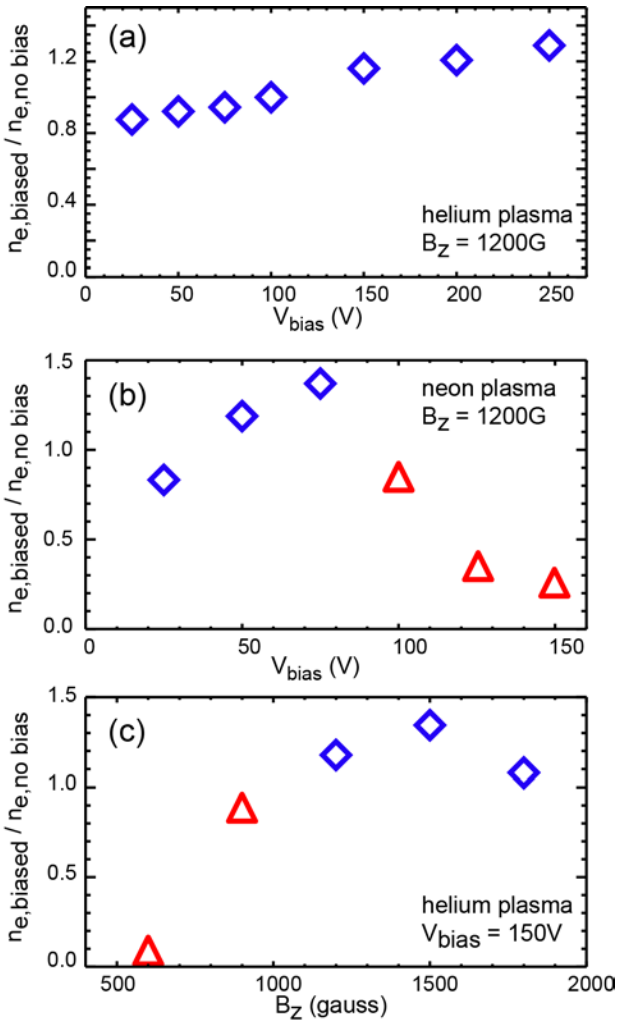

FIG. 5.9 Evolution of the averaged density at the center of the plasma column ($r \le 2cm$) with increased bias voltage on the obstacle (V_{bias}) or axial magnetic field (B_z). The densities are normalized to the averaged plasma density when the obstacle is floating. Diamonds represent cases with improved confinement, while triangles represent cases with plasma depletion.

Direct evaluations of the radial particle flux are made using the $\tilde{I}_{sat}$ and the floating potential $\tilde{V}_f$ data measured simultaneously by triple probes. The electrostatically-driven particle flux is calculated by Eqn. 1.4. The fluctuation of the azimuthal electric field is not directly measured in this experiment. Instead, an estimate of $|E_\theta(\omega)|$ is made using the fluctuation of the floating potential $\tilde{V}_f$. Assuming the waves at the edge plasma have a drift-wave like dispersion relation ($k_\theta \sim \omega$) and that the electron temperature fluctuation $\tilde{T}_e / T_e$ is much smaller than the density fluctuation $\tilde{n}_e / n_e$, one can estimate the four terms in Eqn. 1.4 by:

$$|\tilde{I}_{sat}| \propto |\tilde{n}_e \sqrt{T_e}| \propto |\tilde{n}_e| \qquad (5.1)$$

$$|\tilde{E}_\theta(\omega)| \sim |-\nabla_\theta \tilde{\phi}(\omega)| \sim |k_\theta \tilde{\phi}(\omega)| \sim |\frac{\omega}{V_D}\tilde{\phi}(\omega)| \propto |\omega \cdot \tilde{\phi}(\omega)|, \qquad (5.2)$$

$$\gamma_{n,E_\theta}(\omega) \simeq \gamma_{n,\phi}(\omega), \qquad (5.3)$$

$$\cos(\theta_{n,E_\theta}(\omega)) \sim \cos(\theta_{n,\phi}(\omega) - \frac{\pi}{2}) \sim \sin(\theta_{n,\phi}(\omega)). \qquad (5.4)$$

Then the radial particle flux profile $\Gamma_n(r)$ can be calculated. Figure 5.10(a) shows the evolution of the radial flux profiles as a function of the bias on the obstacle. Positive flux indicates radially outward transport and negative flux indicates inward transport. It is known from Eqn. 1.4 that the direction of the radial flux only depends on the sign of $\sin(\theta_{n,\phi}(\omega))$, which suggests that the cross-phase between the density and potential structures is very important in the radial transport. When increasing the bias on the obstacle from 0V to 75V (the cases with improved confinement), a sheared radial flux profile is observed at the edge of the plasma column, where the maximum flow shear is localized. Outward radial flux is observed at the inner region of the plasma edge. However, a steep change of the radial flux profile, with an inward flux layer at the outer region of the plasma edge, is formed. The reversed flux profile across the radius works as a transport barrier, leading to steeper edge density gradient and improved plasma confinement. The amplitude of the outward and inward flux both increase with the bias voltage, indicating that the sheared azimuthal flow plays an important role in the formation of the flux reversal. Similar flux profiles are observed in the edge plasmas of tokamaks (e. g., in TEXTOR[63]) and basic devices(e. g., in CSDX[64]), where sheared edge flows are driven either by applied external radial electric fields or by the self-generated nonlinear zonal flow. However, when the bias is further increased ($V_{bias} \geq 100V$, cases with density depletion), the outward particle transport dominates the radial flux profiles, and the radial width of the outward flux is comparable to the radius of the plasma column. These results agree well with the observed density evolution within the plasma column in all the cases. The evolution of the radial flux with modified B_z is shown in Figure 5.10(b). B_z is also an effective control parameter to modify the flow velocity. In addition, it affects the turbulent waves by modifying the scale length of ρ_s. The radial particle flux profiles are similar to that with V_{bias} modified. Strong axial magnetic field is favorable to improved plasma confinement, while weak field leads to large outward transport and plasma depletion. This is also consistent with the observed density profiles in these cases.

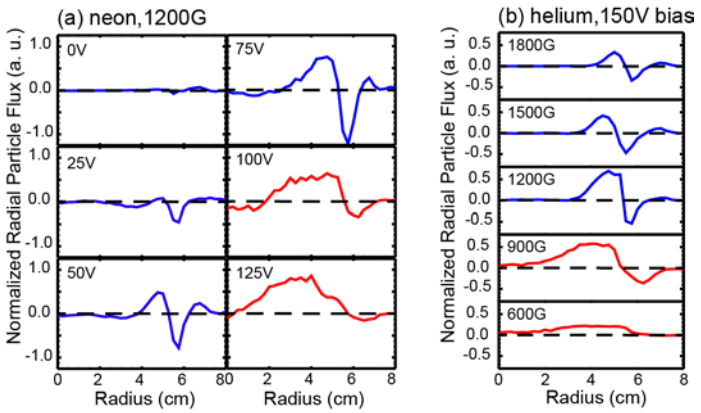

FIG. 5.10 (color online) (a) Radial particle flux profiles with increasing bias on the obstacle in neon plasma with $B_z = 1200G$. Positive flux represents radially outward. (b) Radial particle flux profiles with various B_z in helium plasma with 150V bias on the obstacle. All profiles are averaged over the ~3ms bias time.

5.2.3 Spectrum and Correlation Profiles of the Edge Turbulence

Having examined the radial flux profiles of the cases with both improved confinement and density depletion, we now turn to the plasma edge fluctuations that account for the density behavior. Figure 11 shows the radial profiles of the I_{sat} fluctuating power during the 3-ms pulsed bias on the obstacle, integrated over all frequencies and normalized to the maximum fluctuating power. It is observed that the radial location and extent of the fluctuating power is closely associated with the turbulent transport. Under larger B_z (lower $V_{E\times B}$ and smaller ρ_s), the density fluctuation is localized at the edge region of the plasma column ($r \sim 6cm$) and has a radial extent of *~2cm* (Fig. 5.11(a)). With the axial magnetic field lowered to $B_z \le 900G$, the fluctuations extend throughout the entire plasma column. The lowered total power in cases with small B_z is mainly the result of the rapid density decline during the pulse time, rather than the suppression of the turbulence. Similarly, when the obstacle bias is modified (Fig. 5.11(b)), in the cases with improved confinement ($V_{bias} = 0V - 75V$), the fluctuations are localized at the edge region while, in the cases with density depletion ($V_{bias} \ge 100V$), the radial span of the fluctuation power profile is comparable to the radius of the plasma column. These fluctuation profiles suggest that electrostatic turbulent transport causes the steepening and flattening of the density profile that was described in Ch. 5.2.2.

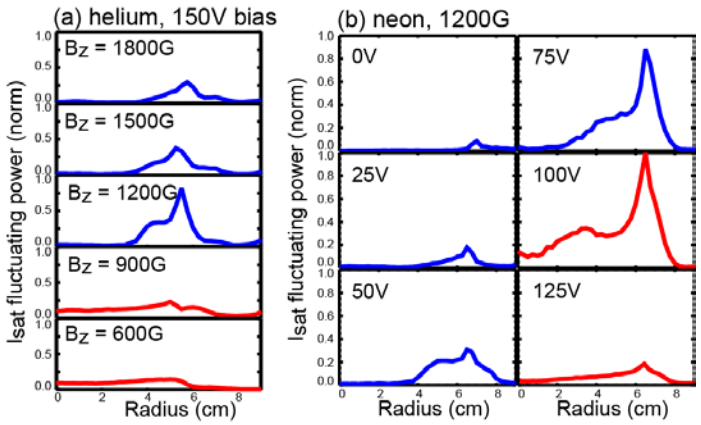

FIG. 5.11 (color online) (a) Radial profiles of the fluctuating power of I_{sat} (averaged over the *3-ms* bias time and totaled over 2-*100 kHz*) with various B_z in helium plasma with 150V bias on the obstacle. Positive flux represents radially outward. (b) Radial profiles of the fluctuating power of I_{sat} with increasing bias on the obstacle in neon plasma with $B_z = 1200G$.

Figure 5.12 presents space and frequency resolved power spectra for six bias voltages (a-f), and the two-dimensional cross-field correlation function of I_{sat} fluctuations under 75V and 125V bias (g-h) in neon plasmas. The frequency range of the edge fluctuations is ~0-30kHz (the ion cyclotron frequency in this experiment is $f_{ci} = 457kHz$ in helium plasma and $f_{ci} = 91kHz$ in neon plasma with $B_z = 1200G$). The frequency gaps between adjacent peaks in the spectrum increase with biasing voltage, indicating the effect of the Doppler-shift in frequency due to larger flow velocity. The two-dimensional (2D) correlation profiles are measured by two Langmuir probes, located downstream of the annulus and separated by 0.3m. The parallel wavelengths of the edge fluctuations are also measured using 2-point correlation techniques, with Langmuir probes separated by various distances. The observed parallel wavelength is $\lambda_{||} \sim 15m$, which is comparable to the machine length. Thus the 2D correlation measurements mostly reveal the mode structures perpendicular to the magnetic field. The correlation function with 75V bias (Fig. 5.12(g)) indicates waves with an average mode number $\bar{m} \sim 2$. The correlated structures are asymmetric, elongated in the azimuthal direction. In contrast, with 125V bias (Fig. 5.12(h)), an $m = 1$ mode dominates. It suggests from the power spectrum that the mode numbers of the dominant modes decrease with increasing bias. The radial correlation length of the $m = 1$ mode structure is ~6cm, which is consistent with the observed fluctuating power and flux profile. Moreover, the $m = 1$ mode is favorable for outward particle transport: the mode structure extends to the core region of the plasma column, and large radial transport along the equipotential line is expected.

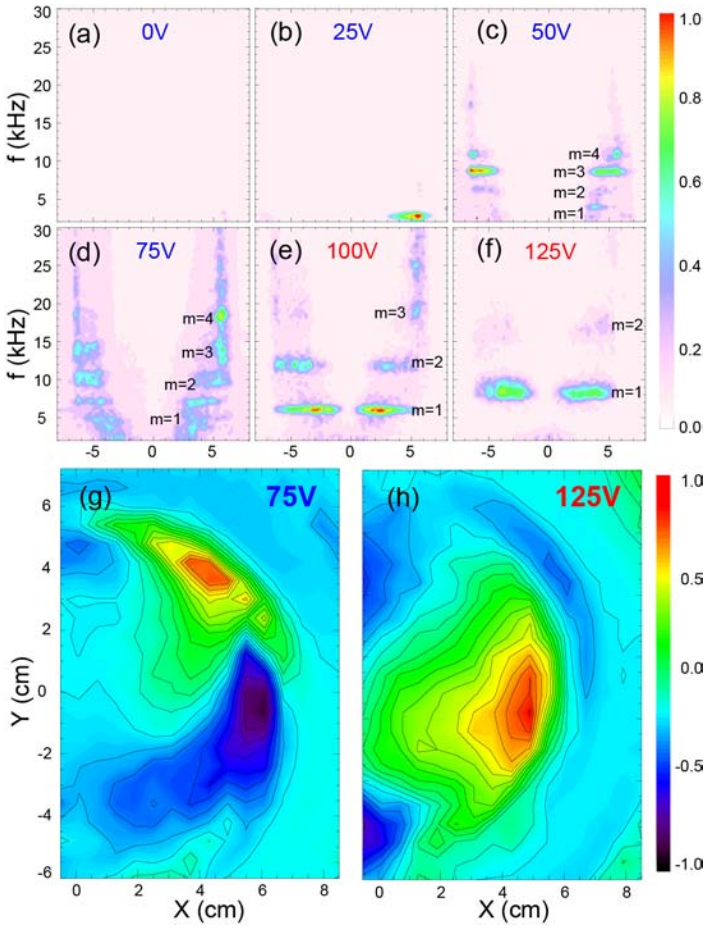

FIG. 5.12 (color online) (a-f) Space resolved I_{sat} FFT power spectra in neon plasma with $B_z = 1200G$ and increasing V_{bias}. (g-h) Two-dimensional cross-field correlation functions for I_{sat} fluctuations in case (d) & (f).

The correlation between density depletion and the *m* = 1 mode is also evident by the time evolution of the fluctuation power spectrum at different bias. Figure 5.13 shows the time evolution of the ion saturation current (I_{sat}) power spectrum for cases discussed above, calculated by Fast Fourier Transform (FFT) with moving time window. With 75V bias on the annulus, the power spectrum is steady during the ~3ms pulse time, and modes with *m* = 1 - 4 have comparable amplitude. With 100V - 150V bias, damping of the modes are observed during the bias time, especially modes with higher m numbers. The up-chirping of the mode frequencies are usually observed in cases with density depletion. With decreasing plasma density during the bias time, the potential applied on the annular obstacle are less shielded by plasmas, which induces larger $E \times B$ drift velocity. This is reflected by a larger Doppler shift effect in frequency in the power spectrum, which explains the up-chirping of the mode frequencies. In all cases with density depletion, it is observed that the *m* = 1 mode dominates in the power spectrum.

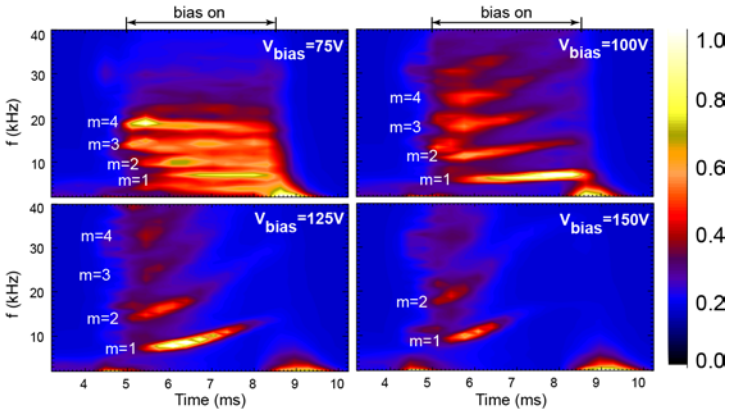

FIG. 5.13 (color online) Time evolution of the power spectrum of fluctuations in ion saturation current for different bias voltage on the annulus. (a) V_{bias} = 75V (case with enhanced plasma confinement) (b)-(d) V_{bias} = 100-150V (cases with depletion in plasma density)

Similar dependencies on the control parameter are observed when the bias is kept constant and the axial magnetic field is varied (Fig. 5.14). With lower B_z, the edge fluctuations have smaller azimuthal mode numbers. Cases with density depletion are also associated with the $m = 1$ mode and with large radial correlation length (Fig. 5.14(h)).

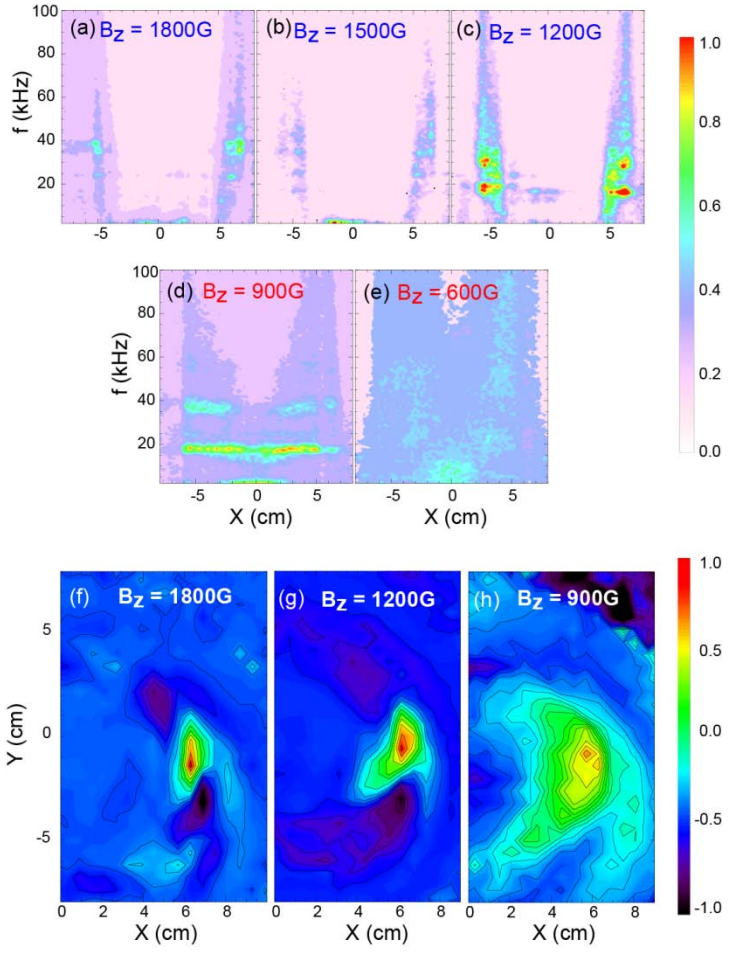

FIG. 5.14 (color online) (a-e) Space resolved I_{sat} FFT power spectra in helium plasma with $V_{bias} = 150V$ and decreasing B_z. (f-h) Two-dimensional cross-field correlation functions for I_{sat} fluctuations in case (a) (c) & (d).

The radial flux profile changes sign at the plasma edge (Fig. 5.10). The mechanism responsible for this reversal is reversal of the cross-phase $\theta_{n,\phi}$ between the density and the potential structures. Figure 5.15 shows the 2-point cross-correlation functions of I_{sat} (colored contour) and the floating potential V_f (white dotted contour), measured using the same triple-probe-pair in helium plasma with 100V bias at the obstacle (a case with improved confinement). The floating potential signal is adjusted according to the phase between the I_{sat} and V_f signals at the reference probe, so that Fig. 5.15 reflect a snapshot of the density and potential structure with the right relative phase between them. The red dashed line indicates the inner edge of the obstacle, which also shows where the radial particle flux reverses its direction. Due to the sheared edge flow, the density and potential fluctuations develop radially sheared structures. The overlap between I_{sat} and V_f structures suggests that a dramatic phase change between density and potential happens across the edge region. Opposite phases between I_{sat} and V_f are observed at the inner and the outer region of the plasma edge (red dashed line). This result clearly confirms that changes in $\theta_{n,\phi}$ cause the observed reversal in radial particle flux.

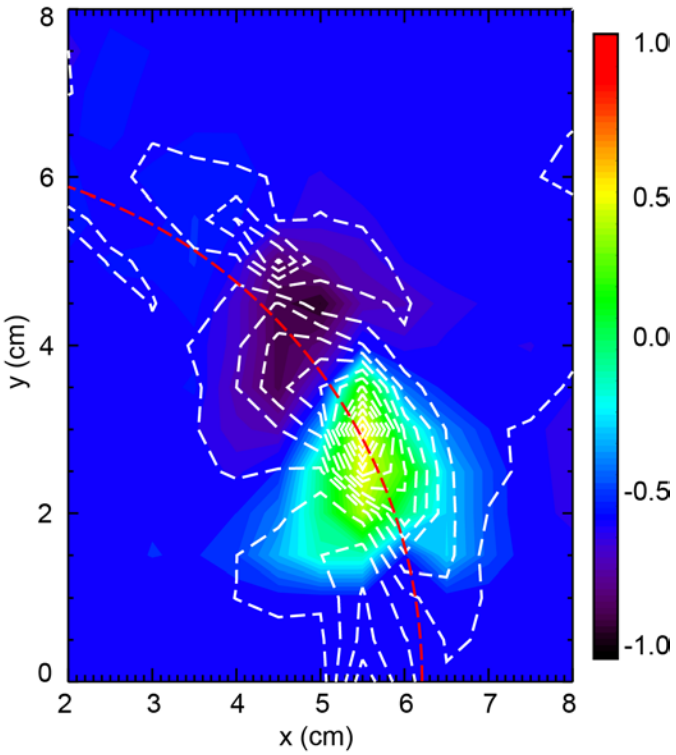

FIG. 5.15 (color online) Two-dimensional cross-field correlation functions for I_{sat} fluctuations (color-filled contour) and the fluctuation of the floating potential V_f (white-dashed contour). The red dashed line indicates the edge of obstacle.

5.3 DISCUSSION AND LINEAR ANALYSIS OF THE EDGE MODES

Identification of the wave modes of the observed edge turbulence is important in understanding the mechanisms of the particle flux and the effects of the biasing on the obstacle. The mode transition in a magnetized plasma column with sheared rotation has been discussed in several publications[42, 65]. In the current experiment, large local radial variation of the phase for plasma potential ($90^\circ - 180^\circ$, indicated in Fig. 15) is observed, which is a signature of the Kelvin-Helmholtz instability (as discussed in Ref. [65]). However, the fact that the density and potential fluctuations have comparable fluctuation amplitude ($\delta n / n \sim e\phi / k_B T_e \sim 0.5$) indicates that the density-gradient driven waves are also important in the edge fluctuation. In LAPD edge plasmas with radial electric field applied by edge biasing, a parameter regime where the turbulence is driven by both density gradient and sheared azimuthal flow is observed (so called Drift-Wave-Kelvin-Helmholtz (DWKH) regime, see Ref. [42]). In DWKH regime, density and potential fluctuations are comparable, and the scale length of the radial velocity shear is comparable to the density gradient. In this experiment, the scale length of the density gradient ($L_n \sim 2\text{cm}$) and the velocity gradient ($L_v = |\ln v_\theta|^{-1} \sim 2\text{cm}$) are comparable to each other, which also fits with the DWKH parameter regime.

Linear analysis on the edge wave modes is done using a Braginskii two-fluid model[66]. Although full nonlinear simulation might be necessary to compare with the experimental results, simple analytic solutions of the fluid equations using the experimental parameters help in mode identification. The fluid equations used here represent conservation of density, electron and ion momentum, and charge, A detailed description of the application of the two-fluid model on LAPD edge turbulence can be found in Appendix C.2 and Ref. [44].

Here we present the linear solutions of the fluid equations using experimentally obtained profiles of the plasma density and potential. The instabilities investigated are drift-wave (DW), interchange instability (IC) and Kelvin-Helmholtz instability (KH). Their frequencies and growth rates are compared. The density profile used in all cases is obtained in neon plasma with 75V bias. Different potential profiles are used to model specific instabilities. The resistive drift wave branch is driven by the gradient of the density profile alone (Fig. 5.16(a)). To model the interchange mode (IC) induced by the plasma rotation, a uniform-rotation potential profile $\phi_0(r) = \Omega r^2 / 2$ is chosen (Fig. 5.16(b)) with the rotation frequency comparable to the maximum rotation frequency in the experimental potential profile. The parallel wave number is also set to zero. This removes the drift-wave (requires finite

parallel wave number) and the Kelvin-Helmholtz instability (requires sheared flow profile) branches from the solution. Pure Kelvin-Helmholtz instability is calculated using a flat density profile but a sheared $E \times B$ flow (Fig. 5.16(c)). Finally, experimental profiles of density and potential (Fig. 5.16(d)) are used to calculate the dispersion relation for the drift-wave-Kelvin-Helmholtz (DWKH) mode. The numerical solutions of the frequencies and growth rates (both normalized to the ion cyclotron frequency ω_{ci}) for these instabilities are shown in Fig. 5.16(e,f). The dispersion relation for both DWKH modes and KH modes agrees with the experimental data. This confirms that the Doppler-shifted frequency spectra observed in this experiment are dominated by the azimuthal flow induced by biasing. The growth rates of the DWKH modes are the largest among all cases examined. The maximum of the growth rate in DWKH mode is at $m_\theta = 6$, which is larger but comparable to the experimental observation ($m_\theta \sim 1-4$, see Fig. 5.12(d, g)). The discrepancy on the mode number between the linear analysis and the experiment may be due to inaccurate modeling of dissipation, or insufficiency of using a linear model to compare with the nonlinear state measured in the experiment.

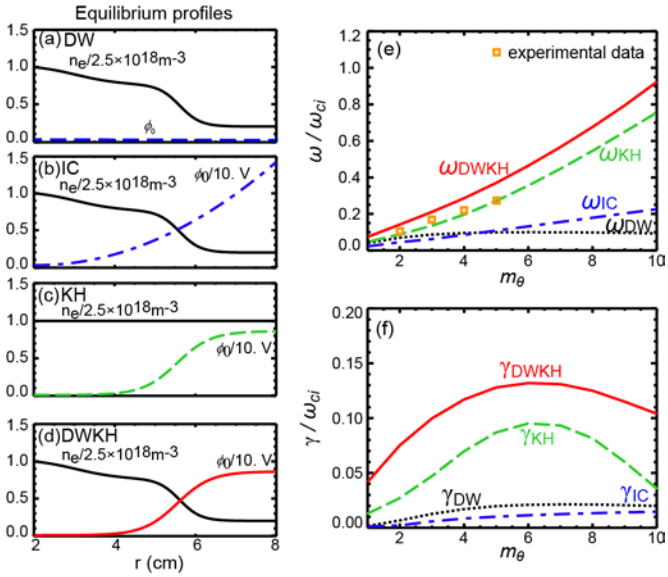

FIG. 5.16 (color online) (a-c) Density and potential profiles used for calculating drift wave, interchange, and Kelvin-Helmholtz branches of the dispersion relation for the experimental parameters. (d) Experimental density and potential profiles in neon plasma with 75V bias on the obstacle. (e-f) frequency and growth rate of the instabilities as a function of azimuthal mode number. The measured data are plotted in squares.

The effect of different obstacle-bias voltages on the mode growth rates for the DWKH modes are also explored using the linear model. The experimentally measured plasma potential profiles at various bias voltages in neon plasmas (Fig. 5.17(a)) are used in the model. Figure 5.17(b) shows the m numbers of the modes with the largest growth rate (γ), in four cases with different bias on the annulus. The simulation result shows that the

dominant mode number decreases with increasing bias. This agrees with the observation (Fig. 5.12) very well.

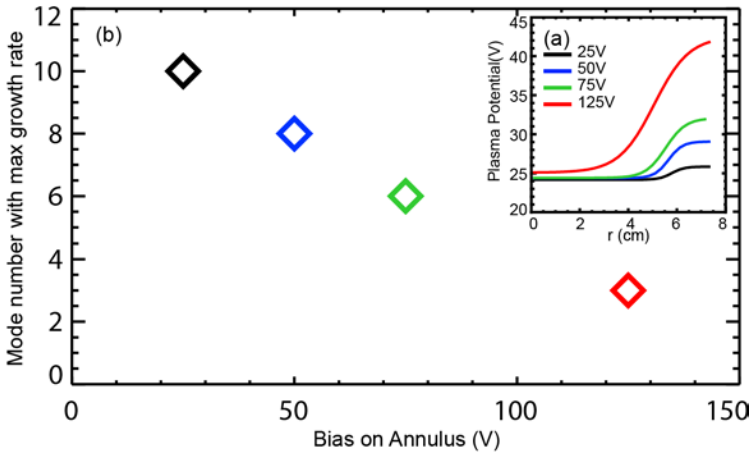

FIG. 5.17 (color online). (a) Plasma potential profiles used in the linear model, measured by swept Langmuir probe. (b) Mode number (m) of modes with largest growth rate as a function of the annulus bias voltage.

Overall, the analysis of the linear instabilities for the plasma column supports the idea that the edge turbulence is co-driven by the steep density gradient and the large sheared azimuthal flow, and that the edge $E\times B$ drift dominates the dispersion relation of the fluctuation. However, some aspects of the experiment, such as the damping rate of the high m number modes with large bias and the radial correlation scale of the low m modes (which leads to plasma depletion), are not correctly simulated by linear modeling. Kinetic effects might also play an important role in the instabilities, especially in cases with neon plasmas and low axial magnetic fields. The boundary condition used in the linear model is periodic, thus the effect due to the fixed boundary at the LAPD end is not included. Such boundary condition will leads to a so-called "line-tying" effect, which is stabilizing the Kelvin-Helmholtz mode[67]. An estimate of the "line-tying" stabilizing effect can be made by comparing the maximum growth rate (γ) of K-H instability in the linear 1D model and $k_{||}V_A$, where $k_{||}$ is the parallel wavenumber of the mode and V_A is the Alfvén speed. Figure 5.18 plots an estimate of $k_{||}V_A/\gamma$ versus the strength of the magnetic fields in both helium and neon plasmas. It is indicated that K-H mode is better stabilized with increasing B_z, and with helium plasma comparing with neon plasma. The trend in this estimate agrees with the experimental observation. Another way to estimate the growth rate of the modes from the experimental data is to estimate the damping rate of the modes from the fluctuating power spectrum. In a simple damped oscillation model, the damping rate for a certain mode is $\gamma\sim\Delta\omega/2$, where $\Delta\omega$ is the FWHM of the power spectrum of that mode. In a typical experimental case we studied, the FWHM of a mode in plasma frame is $\Delta f\sim 1$kHz, and the normalized damping rate for this mode is $\gamma/\omega_{ci} \sim \pi\Delta f/\omega_{ci} \sim 0.004$. This is much smaller than the calculated growth rate of the KH modes in linear model, but comparable to the growth rate of drift wave or interchange instability (see Fig. 5.16). Full nonlinear

simulation (e. g., by using the BOUT[45, 68] three-dimensional Braginskii fluid turbulence code) is necessary to reach quantitative agreement with the experimental data.

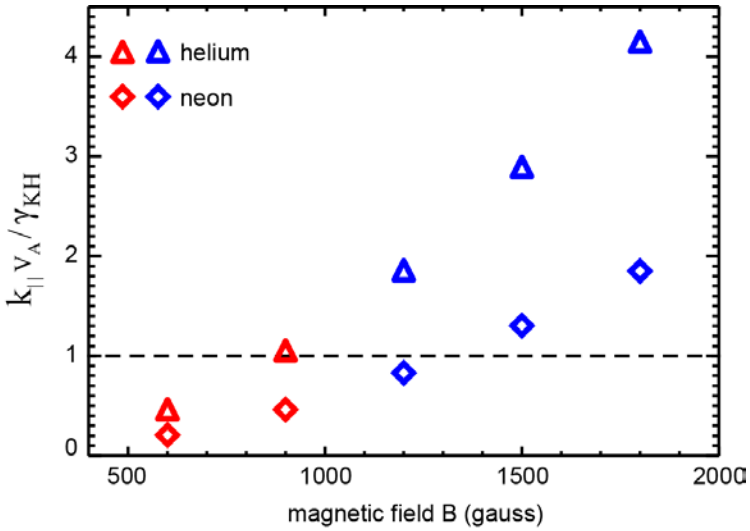

FIG. 5.18 Estimate of the "line-tying" effect on the stability of Kelvin-Helmholtz instability. Red data points indicate density depletion cases in experiment, while blue data points indicate improved confinement.

5.4 CONCLUSION

A plasma column with 12 cm in diameter is formed by inserting an annular shaped obstacle concentrically with the main plasma in the LAPD. Sheared $E \times B$ flow is applied to the edge of the plasma column by biasing the obstacle. Modification of the plasma characteristics and cross-field transport by changing the obstacle biasing voltage, the strength of the axial magnetic field and the plasma species are fully studied.

With sheared flow induced, the most significant change in plasma characteristics is the formation of a reversed particle flux layer at the plasma edge. The reversal in transport direction is explained by the ~180° change in the cross-phase between the density and potential fluctuation across the sheared layer, which forms a transport barrier and improves plasma confinement. It is also observed that when the control parameters are above a threshold, the cross-field transport is enhanced dramatically, leading to depletion of the plasma density. In the fluctuation power spectrum, the depletion cases are associated with the dominant *m=1* mode and the damping of the high m number modes with large Doppler-shift in frequency.

Chapter 6
CONCLUSIONS

6.1 Summary

In this thesis work, the interaction between a test-particle fast-ion beam and electrostatic wave turbulence has been fully studied. The thermal plasma cross-field transport induced by electrostatic instabilities is also explored.

The main approach to study the fast-ion transport in electrostatic turbulence described in this thesis work is launching fast-ion beam as test particles in the background plasmas, with turbulent waves driven by gradients in plasma density (drift wave like instabilities) and potential (Kelvin-Helmholtz or interchange like instabilities). Gradients in plasma density are induced by obstacles. A half-plate and an annular-shape obstacle are used. Gradients in plasma potential are induced by positive bias on the obstacles related to the LAPD anode. The fast-ion orbits are controlled by the pitch angle and voltage on the acceleration grids of the fast-ion gun. The background wave instabilities are modified by the geometry of the obstacles, bias voltage on the obstacle, axial magnetic field strength and plasma species. These control parameters effectively modify the spatial and temporal scales of the instabilities. In this experiment, the fast-ion beam is treated as test particles and the turbulent waves are treated as background. The fast-ion population induced instabilities are negligible. The dependence of the fast ion transport on the fast-ion energy, the wave number ($k_{\perp}$) and correlation length (L_{corr}) are fully studied. The experimental results agree well with the so called gyro-averaging theory. The fast-ion transport decreases with increasing fast-ion energy. And wave instabilities with a larger spatial scale induce more fast-ion transport. These experimental observations are also consistent with the test-particle Monte-Carlo simulation results.

In the experiment with an annular obstacle, the turbulence downstream from the inner edge of the annulus and the induced plasma transport are also explored. Modification of the edge instabilities and density confinement are achieved. Two parameters, $E \times B$ drift velocity ($v_{E\times B}$) and ion sound radius (ρ_s), are proved to modify the mode number of the plasma instabilities and the density confinement effectively. A parameter regime with improved density confinement, as well as a parameter regime with large radial density transport, is observed. The cases with improved density confinement are correlated with small ρ_s and modes with high m number. The cases with density depletion are correlated with large ρ_s and modes with low m number (mainly m=1). Investigation on the radial density flux profiles in these cases indicates that, in cases with improved density confinement, the radial flux reverses its direction at the plasma edge. The reversal is

induced by the reversal in phase between the plasma density fluctuations ($\tilde{n}_e$) and the potential fluctuations ($\tilde{\phi}$) at the plasma edge region. In contrast, in cases with density depletion, the outward radial flux dominates in the profiles, which is correlated with the large spatial structure scale of the m=1 mode. The large outward flux is consistent with the quick depletion in plasma density in these cases. The edge turbulence is also analyzed by a linear model using two-fluid Braginskii equations and the experimental density and potential profiles. It is indicated that Kelvin-Helmholtz instabilities have the largest growth rate, and its dispersion relation also matches the experimental observation.

The experimental setup reported in this paper provides an effective and unique approach to study the energetic ion transport in a variety of electrostatic or electromagnetic background waves. It is also designed to study the modification and control of the edge plasma characteristics and thermal plasma transport, which helps to understand the basic mechanisms of the transport induced by gradient-driven and shear-driven edge turbulent waves. The diagnostics in this experiment are usually direct with probes, avoiding the complexities of indirect diagnostic approaches. The interpretations of the data are very clear and easy to compare with theoretical and simulation results. The instabilities driven by the obstacles are very well diagnosed, forming a good dataset for comparison with linear and nonlinear simulation results from fluid or gyrokinetic codes such as BOUT++ and GTC.

6.2 Future Work

The experimental setup in this thesis work serves well to study the interaction between a fast-ion beam and the background turbulence in a short time-scale (comparable to the average period or decorrelation time of the background waves). Running the Lithium ion source at high pitch angles effectively increases the ion beam time-of-flight in wave. However, this technique has some limitations: Firstly, the maximum pitch angle of the ion source is limited by the size of the gun housing to ~80°. And the maximum number of gyrations the ion beam can orbit through between two diagnostic ports is ~6. Moreover, due to the angular and energy divergence of the ion beam, as well as the Coulomb collisions between the beam ions and the background plasma, the divergence in the axial energy (E_z) of the fast ion beam increases with the axial distance the beam travels. This leads to large axial divergence of the beam and uncertainty in the number of gyrations the ion beam completes before it is collected. An estimate base on the Monte Carlo particle tracing simulation indicates that, at the pitch angle of 77°, when the ion beam finish an average of 16 gyrations, the uncertainty in the number of gyrations among the ion population is ~3 gyrations. In future experiments, a long time-scale wave-particle interaction is desired. Thus improved diagnostics to quantify the divergence in the beam axial energy (E_z) is needed. The recently installed fast-imaging camera system at the LAPD is able to capture optical signals with ~10μs temporal resolution and 14-bit spatial resolution, which is a

good candidate for a direct optical diagnostic of the axial broadening of the ion beam. On the other hand, a lithium ion beam source with higher emission current, smaller energy and smaller angular divergence would also be beneficial.

The improvement of the diagnostic tools will benefit the future experiments in multiple aspects. Firstly, a detector probe with higher bandwidth is highly desirable to study the temporal evolution of the fast-ion beam in the antenna-driven waves in the LAPD. For example, if the fast ion beam is phase-locked with the background waves (which is true for shear Alfvén waves driven by an antenna), then modification of the fast ions by electromagnetic waves with different initial phases and multiple frequencies can be observed. Secondly, due to the energy, angular and spatial spreading of the fast ion beam under a variety of effects, a single diagnostic probe is not sufficient to depict the spatial and energy distribution of the fast ion population. Development and comparison of multiple diagnostics tools is both challenging and rewarding.

The study of fast-ion transport in waves with larger magnetic fluctuations is also of great interest and predicted[15] to have different scaling to that in electrostatic waves. Several publications[69-71] suggest that the turbulent waves induced by obstacles in the LAPD are drift-Alfvén modes in nature, and the coupling between density fluctuations and magnetic fluctuations depends upon the electron plasma beta[72] (β_e). Substantial density and magnetic fluctuations ($\delta n/n \approx 0.2$, $\delta B/B \approx 2\times10^{-3}$) is observed[72] along a filamentary density depletion. The response of the fast-ion beam under such electromagnetic background turbulence is interesting and can be compared with published theoretical and simulation results. If the fast-ion collector is improved to resolve the beam energy distribution accurately, fast ion stochastic heating in turbulence also could be examined.

In the study of turbulence and thermal plasma transport at the edge of the obstacles, several topics will be also rich in physics. Firstly, in Chapter 5, the radial transport of the thermal plasmas is evident from the radial particle flux profiles, density evolution of the plasma column, and the fast-imaging camera data. However, a direct measurement of the "scrape-off" of the density at the edge of the plasma column is not available. How the density and energy transport happen at the so-called scrape-off layer (SOL) is of great interest in both Tokamak edge confinement and basic plasma experiments, and many works[25, 73-76] have been done to investigate it. In an experiment at the LAPD using the plate obstacle described in Chapter 3, it is observed that the transport events at the SOL are dominated by density depletion (or "holes") in the high-density region and density enhancement (or "blobs") in the low-density region. The detachment and outward propagation of the turbulent structures (blobs) are argued to be the major form of the cross-field transport. In this thesis work, the annular obstacle used is also a good approach to study the turbulent transport events. The variable V_{bias} on the obstacle and other control parameters leads to a variety of edge turbulence conditions, and the effects of these

parameters on the blob-like detachment events can be fully explored. It is evident from several of the wave cross-field correlations functions (e. g., Fig. 5.14 (f)-(h)) that the density scrape-off behavior varies with parameters such as B_z. Further investigation on this topic is worthwhile.

Another aspect to investigate in this direction is the nature of the modes driven at the plasma edge. In the linear analysis discussed in Chapter 5, it is indicated that the Kelvin-Helmholtz instability is the dominant mode at the plasma edge, with the largest growth rate. However, the linear model misses some very important physics. For example, the kinetic effects are not included, which is proved to be important in experiment: very different edge turbulences are observed in helium and neon plasmas, for which the kinetic effects due to different scale length of the ion sound radius ρ_s may play an important role. Thus nonlinear, gyrokinetic simulations will describe the nature of the edge turbulence more accurately. Two nonlinear simulation codes, BOUT++[44, 68] and GTC[33], are recently modified to simulate a LAPD-like device with cylindrical geometry. The equilibrium profiles of plasma density and potential in the annular-obstacle setup are of very symmetrical cylindrical geometries. Thus this is a good case to benchmark and compare these codes. The nonlinear simulation results are also desirable to understand the mechanism of the edge modes and turbulent transport.

Experimentally, modification of the edge instabilities can also be done by introducing magnetic shear. It is predicted that the Kelvin-Helmholtz like instabilities can be suppressed by magnetic shear[32]. As a linear device, LAPD has only axial magnetic field. However, magnetic shear could be introduced experimentally. Ideas such as inducing an axial current, or launching shear Alfvén waves have been discussed in order to induce shear in the magnetic field lines. Studies on the modification of the edge turbulence by magnetic shear is practical and of great interest. Also, the diameter of the plasma column affects the edge turbulence. Studies in these aspects will help to better understand the mechanism of the sheared-flow induced confinement transition.

APPENDIX A
Typical Parameters for LAPD Plasmas and Ion Beam Operation

Magnetic field, B	0.6 - 1.8 kG
Pressure, P	2.3×10^{-5} Torr
Electron density in afterglow, n_e	10^{11} cm^{-3}
Electron density in Discharge, n_e	2×10^{12} cm^{-3}
Neutral density, n_0	6×10^{11} cm^{-3}
Electron temperature in afterglow, T_e	0.13 eV
Electron temperature in Discharge, T_e	6 - 7 eV
Ion temperature in afterglow, T_i	0.1 eV
Ion temperature in Discharge, T_i	1 eV
Plasma column length	18 m
Plasma column diameter	70 cm
Cathode-anode discharge current	5 - 6 kA
Cathode-anode discharge frequency	1 Hz
Afterglow time	50-60 ms
Discharge time	8 - 10 ms
Floating potential	45-50 V
Beam energy, W	~ 600 eV
Beam current density, *j*	1 mA / cm^2
Beam size	0.5 cm Dia.
Pitch angle, θ	28 - 80°
Gyro-radius of fast ions, ρ	3 - 6 cm
Emitter voltage	600V
Accelerator voltage	- 100 V
Energy spread, ΔE	~15 eV
Beam divergence	~5 degrees

APPENDIX B
List of Data Sets Supporting Experimental Results

B. 1 Fast Ion Transport in Electrostatic Turbulent Waves

FIGURE	DATASET	DATE	IDL CODE
Fig. 3.2	p32xy_sen2_p30xy_b9_plate_1200G_detailed.hdf5 p29xy_triple_plate_1200G_background.hdf5	JUN2009	figure09_density fluctuation.pro
Fig. 3.3	p32xy_hybridIII_1200G_466V_fine.hdf5	JUN2009	figure02_time trace.pro
Fig. 3.4	p32xy_sen2_p30xy_b9_plate_1200G_detailed.hdf5	JUN2009	figure01_turbulence.pro
Fig. 3.5	p32xy_hybridIII_1200G_466V_fine.hdf5 p32xy_hybridIII_656V_Plate_ON_fine.hdf5 p32xy_hybridIII_920V_Plate_fine.hdf5 p32xy_hybridIII_1150V_Plate_ON_fine.hdf5	JUN2009	figure04_contour_energy dependence.pro
Fig. 3.6	p32xy_hybridIII_466V_Plate_OFF_coarse.hdf5 p33xy_hybridIII_656V_Plate_OFF_fine.hdf5 p32xy_hybridIII_920V_Plate_OFF_fine.hdf5 p32xy_hybridIII_1150V_Plate_OFF_fine.hdf5	JUN2009	figure06_energy dependence.pro
Fig. 3.7	p33_Hybrid_fine_467V.hdf5 p32_Hybrid_fine_467V_I.hdf5 p31_Hybrid_fine_467V.hdf5 p30_Hybrid_fine_467V.hdf5	FEB2010	figure05_contour_time dependence.pro
Fig. 3.8	p33_Hybrid_fine_467V_L.hdf5 p32_Hybrid_fine_467V_II_L.hdf5 p31_Hybrid_fine_467V_L.hdf5 p30_Hybrid_fine_467V_L.hdf5	FEB2010	figure07_time dependence.pro
Fig. 3.9	p30xy_triple_plate_1200G_detailed.hdf5	FEB2010	figure11_Gyro averaging.pro
Fig. 3.12	n/a	n/a	figure13_MC time dependence.pro

Fig. 3.13	n/a	n/a	figure14_MC GC trace.pro
Fig. 4.2	P31_line_100V.hdf5	AUG2010	Figure001_Sample_Profile.pro
Fig. 4.3 Fig. 4.4 Fig. 4.5	Aug24_P31_P33_fine_Correlation_scan_6mmx6mm_100V.hdf5 Aug26_P31_P33_fine_Correlation_scan_6mmx6mm_100V_Neon.hdf5	AUG2010	Figure_TCorrelation.pro Figure_Spectrum_Triple.pro
Fig. 4.6 Fig. 4.7	Aug29_fine_He_2_port_realigned.hdf5 Aug29_fine_He_3_port_realigned.hdf5 Aug29_fine_He_4_port_realigned.hdf5 Oct22_p33_Neon_Hybrid_fine.hdf5 Oct22_p32_Neon_Hybrid_fine.hdf5 Oct22_p31_Neon_Hybrid_fine.hdf5	AUG2010 OCT2010	Figure_FWHM_k_perp.pro Figure_FWHM_Lcorr.pro
Fig. 4.9	n/a	n/a	Figure_Illustrate_Gyro Averaging.pro
Fig. 4.11	Jan10_p32tpmov_p34mpfixd_150V_correlation.hdf5	JAN2011	Figure_TCorrelation.pro Figure_Spectrum_Triple.pro
Fig. 4.12 Fig. 4.13	Jan13_HYBRID_p31_150V_1x4_realign.hdf5 Jan13_HYBRID_p31_150V_15x4_realign.hdf5 Jan13_HYBRID_p31_150V_7in4_realign.hdf5 Jan13_HYBRID_p31_150V_2x4_realign.hdf5 Jan13_HYBRID_p31_150V_25x4_realign.hdf5 Jan13_HYBRID_p31_150V_3x4_realign.hdf5 Jan13_HYBRID_p31_150V_35x4_realign_II.hdf5 Jan13_HYBRID_p31_150V_4x4_realign.hdf5 Jan13_HYBRID_p31_150V_45x4_realign.hdf5 Jan14_HYBRID_p31_150V_55x4_realign.hdf5	JAN2011	Figure_Subdiffusion.pro Figure_Subdiffusion_4P_II.pro Figure_Subdiffusion_MC.pro
Fig. 4.15	Jan12_HYBRID_p33_150V_1x2_realign.hdf5	JAN2011	
Fig. 4.16	AUG31_2Ports_1TURN_50V_R52.hdf5 AUG31_2Ports_1TURN_75V_R52.hdf5	AUG2011	Drift_Stat.pro

Fig. 4.17	AUG31_2Ports_1TURN_100V_R52.hdf5 AUG31_2Ports_15TURN_100V_R52.hdf5 AUG31_2Ports_25TURN_100V_R52.hdf5		
Fig. 4.22	AUG31_2Ports_2TURN_100V_R52.hdf5	AUG2011	

B. 2 Sheared-Flow Induced Transition of Thermal Plasma Confinement

FIGURE	DATASET	DATE	IDL CODE
Fig. 5.3	Jan10_p32_He_100Vbias_triple.hdf5 Jan14_p32_mach_100V_xline.hdf5	JAN2011	MACH_analysis.pro
Fig. 5.4	Oct24_p34_Neon_25V_triple.hdf5 Oct24_p34_Neon_50V_triple.hdf5 Oct24_p34_Neon_75V_triple.hdf5 Oct24_p34_Neon_125V_triple.hdf5	OCT2010	Figure001_Sample_Profile.pro
Fig. 5.5	n/a	n/a	Fig01_Cases.pro
Fig. 5.6 Fig. 5.7	Jan11_p32_He_150Vbias_1500G_triple.hdf5 Jan11_p32_He_150Vbias_600G_triple.hdf5	JAN2011	Figure003_3D_Isat.pro Figure004_Density_3cases.pro Figure005_density_depletion.pro
Fig. 5.8	fc_annulus_150V_1200G_128x128.cine annulus_150V_600G_B.cine	JAN2011	loadphantom_eps.pro
Fig. 5.9 Fig. 5.10 Fig. 5.11 Fig. 5.12 Fig. 5.13 Fig. 5.14	P31_line_25V.hdf5 P31_line_50V.hdf5 P31_line_75V.hdf5 P31_line_100V.hdf5 Oct24_p34_Neon_25V_triple.hdf5 Oct24_p34_Neon_50V_triple.hdf5 Oct24_p34_Neon_75V_triple.hdf5 Oct24_p34_Neon_125V_triple.hdf5 Jan10_p32_He_100Vbias_triple.hdf5 Jan10_p32_He_150Vbias_triple.hdf5	AUG2010 OCT2010 JAN201	Figure006_Trend_Density.pro Figure007a_FFT_Isat_Bz.pro Figure007b_RMS_Isat_Bz.pro Figure008_FFT_Isat_Vb.pro Figure009a_Spectrum_Isat_Bz.pro Figure009b_Spectrum_

	Jan10_p32_He_200Vbias_triple.hdf5 Jan10_p32_He_250Vbias_triple.hdf5 Jan11_p32_He_150Vbias_600G_triple.hdf5 Jan11_p32_He_150Vbias_900G_triple.hdf5 Jan11_p32_He_150Vbias_1500G_triple.hdf5 Jan11_p32_He_150Vbias_1800G_triple.hdf5	1	Isat_Vb.pro
Fig. 5.15	Jan10_p32tpmov_p34mpfixd_150V_correlation.hdf5	JAN2011	Fig05_XSPEC_Isat_Vf.pro
Fig. 5.16	n/a	n/a	Fig08_Omega_Gamma.pro

APPENDIX C
Simulation Codes

C. 1 Monte-Carlo Particle Following Code

A Monte-Carlo particle following code is developed[77] and upgraded[54] to simulate the orbit trajectories of a test-particle fast-ion beam by tracing the equation of motion for each test particle simulated using 4th order Ronge-Kutta method. The following effects are included in the simulation:

- Coulomb collisions (pitch angle scattering): The collision operator (*pas.pro*) is developed by A. H. Boozer[61-62]. The collision operator is called once per each fast ion gyro-orbit. The velocity space scattering during each gyro-orbit is:

$$\bar{V}_n = (1-\nu_\perp \tau)\bar{V}_0 + \sqrt{(1-\frac{1}{2}\nu_\perp \tau)\nu\tau}(\pm\hat{\pi}_0 \pm \pi_0 \times \hat{V}_0)V_0$$

  where $\bar{V}_0$ and $\bar{V}_n$ are velocity vectors before and after collision, τ is the gyro-period, and $\nu_\perp$ is the pitch angle scattering[78] frequency. $\hat{\pi}_0$ is the unit vector of a random direction perpendicular to $\bar{V}_0$.
- Energy and angular divergence of the initial fast-ion particle velocity: set by "*sourcedivergence"* and "*energyspread"* in *orbit_Drift.pro*
- Two-dimensional or three-dimensional background electric and magnetic fields: imported in *derives_drift.pro* in Cartesian coordinates.
- The geometrical effect of the fast-ion collector and the effect of the static bias on the collector grids: A modified module ("*collector*") is developed to simulate the instrumental function of the collector probe, with the purpose of comparing better with the experimental data. The criterion for a fast ion particle to be collected is that it reaches the copper disk inside the collector housing. The particle hitting the side wall inside the collector will be considered lost. Furthermore, since the two grids inside the collector are usually biased, simulations that include static electric fields from the biased grids are more accurate. The static electric field is simulated using COMSOL, and is imported as background field in calculating the fast-ion trajectory inside the collector.

C. 2 Eigen-Solver and BOUT

The linear analysis described in Chapter 5.3 is solved by an Eigen-Solver code[44] developed by P. Popovich and B. Friedman, UCLA. This code is base on a Braginskii two-fluid model. The equations represent conservation of density, electron and ion momentum, and charge,

$$(\partial_t + v_e \cdot \nabla)n = 0$$

$$nm_e(\partial_t + v_e \cdot \nabla)v_e = -\nabla p_e - ne(E + \frac{1}{c} v_e \times B) - nm_e \nu_{ei} v_e$$

$$nm_i(\partial_t + v_i \cdot \nabla)v_i = ne(E + \frac{1}{c} v_i \times B) - nm_i \nu_{in} v_i$$

$$\nabla \cdot J = 0, \quad J = en(v_{i||} - v_{e||}) + en(v_{i\perp} - v_{e\perp})$$

Typical commands to run the Eigen-Solver are (see "example_run.py"):

```
im = int(raw_input())

p = eigsolver_4var.PhysParams(Nr=100, aa=20, b0=0.12, mtheta=im, rmin_m=0.005, rmax_m = 0.08, np='NE75V', pp='NE75V_P', tp=0, phi0v=1., nz=1, n0=2.5e18, mu_fac=0, mag_mu=0)

esolver = eigsolver_4var.EigSolve(equation, p)  # Solve the eigenvalue problem
```

Here the parameters are set in *eigsolver_4var.PhysParams* as follows:

Nr	number of points in radial array (1/radial grid size)
aa	mass number
b0	axial magnetic field strength (Tesla)
mtheta	azimuthal mode number to calculate
rmin_m, rmax_m	minimum and maximum radial position (m)
np, pp, tp	equilibrium profiles of density, potential and temperature, set in "profiles.py"
phi0V	amplitude of the plasma potential (V)
nz	axial mode number
n0	equilibrium density (m^{-3})
mu_fac	include (1)/ignore (0) ion viscosity
mag_mu	use magnetized (1)/unmagnetized (0) ion viscosity

The solutions of the eigen-values and eigen-vectors are stored in a structure named "*esolver*". The two-dimensional eigen-mode structure can be plotted by "plot_2Deig.py"

The turbulent wave structures used in Chapter 3.4 are simulated using BOUT. BOUT is a three-dimensional Braginskii fluid turbulence code. The model used in BOUT is the same as in Eigen-Solver. However, BOUT solves an initial value problem, and can simulate both the linear growth and nonlinear saturation of the turbulent modes. The linear results of BOUT have been compared[44] with the numerical eigen-mode solution by Eigen-Solver and reach good agreement.

REFERENCES

[1]A. Fasoli, C. Gormenzano, H. L. Berk, B. Breizman, S. Briguglio, D. S. Darrow, N. Gorelenkov, W. W. Heidbrink, A. Jaun, S. V. Konovalov, R. Nazikian, J.-M. Noterdaeme, S. Sharapov, K. Shinohara, D. Testa, K. Tobita, Y. Todo, G. Vlad and F. Zonca, Nucl. Fusion **47**, S264 (2007)

[2]W. W. Heidbrink and G. Sadler, Nucl. Fusion **34**, 535 (1994)

[3]T. Hauff, F. Jenko, A. Shalchi and R. Schlickeiser, Astrophysical Journal **711**, 997 (2010)

[4]S. Günter, G. Conway, S. daGraça, H.-U. Fahrbach, C. F. M. G. Muñoz and T. Hauff, Nucl. Fusion **47**, 920 (2007)

[5]T. Suzuki, S. Ide, T. Oikawa, T. Fujita and M. Ishikawa, and the JT-60 team, Nucl. Fusion **48**, 045002 (2008)

[6]W. W. Heidbrink, J. M. Park, M. Murakami, C. C. Petty, C. Holcomb and M. A. V. Zeeland, Phys. Rev. Lett. **103**, 175001 (2009)

[7]J. M. McChesney, P. M. Bellan and R. A. Stern, Phys. Fluids **B 3**, 3363 (1991)

[8]J. M. McChesney, R. A. Stern and P. M. Bellan, Phys. Rev. Lett. **59**, 1436 (1987)

[9]H. Naitou, T. Kamimura and J. M. Dawson, J. Phys. Soc. Jpn. **46**, 258 (1979)

[10]G. Manfredi and R. O. Dendy, Phys. Rev. Lett. **76**, 4360 (1996)

[11]G. Manfredi and R. O. Dendy, Phys. Plasmas **4**, 628 (1997)

[12]M. Vlad, F. Spineanu, S.-I. Itoh, M. Yagi and K. Itoh, Plasma Phys. Control. Fusion **47**, 1015 (2005)

[13]T. Hauff and F. Jenko, Phys. Plasmas **13**, 102309 (2006)

[14]G. I. Taylor, Proc. London Math. Soc **20**, 196 (1920)

[15]T. Hauff and F. Jenko, Phys. Plasmas **15**, 112307 (2008)

[16]T. Hauff, M. J. Pueschel, T. Dannert and F. Jenko, Phys. Rev. Lett. **102**, 075004 (2009)

[17]W. Zhang, Z. Lin and L. Chen, Phys. Rev. Lett. **101**, 095001 (2008)

[18]M. Albergante, J. P. Graves, A. Fasoli and X. Lapillonne, Nucl. Fusion **50**, 084013 (2010)

[19]H. Vernickel, M. Blaumoser, K. Ennen, J. Gruber, O. Gruber, O. Jandl, M. Kaufmann, H. Kollotzek, W. Köppendörfer, H. Kotzlowski, E. Lackner, K. Lackner, J. Neuhauser, J.-M. Noterdaeme, M. Pillsticker, R. Pöhlchen, H. Preis, K.-G. Rauh, H. Röhr, H. Schneider, W. Schneider, U. Seidel, B. Sombach, B. Streibl, G. Venus, F. Wesner and A. Wieczoreka, J. Nucl. Mater. **128**, 71 (1984)

[20]J. M. Park, M. Murakami, C. C. Petty and W. W. Heidbrink, Phys. Plasmas **16**, 092508 (2009)

[21]W. W. Heidbrink, M. Murakami, J. M. Park, C. C. Petty and M. A. V. Zeeland, Plasma Phys. Control. Fusion **51**, 125001 (2009)

[22]G. Plyushchev, A. Diallo, A. Fasoli, I. Furno, B. Labit, S. H. Müller, M. Podestà, F. M. Poli, H. Boehmer, W. W. Heidbrink and Y. Zhang, Rev. Sci. Instrum. **77**, 10F503 (2006)

[23]G. Plyushchev, Interaction of supra-thermal ions with turbulence in magnetized toroidal plasma, Ph. D. thesis, Ecole Polytechnique Fédérale de Lausanne (2009)

[24]W. Gekelman, H. Pfister, Z. Lucky, J. Bamber, D. Leneman and J. Maggs, Rev. Sci. Instrum. **62**, 2875 (1991)

[25]T. A. Carter, Phys. Plasmas **13**, 010701 (2006)

[26]H. Boehmer, D. Edrich, W. W. Heidbrink, R. McWilliams and L. Zhao, Rev. Sci. Instrum. **75**, 1013 (2004)

[27]Y. Zhang, H. Boehmer, W. W. Heidbrink and R. McWilliams, Rev. Sci. Instrum. **78**, 013302 (2007)

[28]L. Zhao, W. W. Heidbrink, H. Boehmer and R. McWilliams, Phys. Plasmas **12**, 052108 (2005)

[29]Y. Zhang, W. W. Heidbrink, H. Boehmer, R. McWilliams, S. Vincena, T. A. Carter, W. Gekelman, D. Leneman and P. Pribyl, Phys. Plasmas **15**, 102112 (2008)

[30]Y. Zhang, W. W. Heidbrink, S. Zhou, H. Boehmer and R. McWilliams, Phys. Plasmas **16**, 055706 (2009)

[31]F. Wagner, G. Becker, K. Behringer, D. Campbell, A. Eberhagen, W. Engelhardt, G. Fussmann, O. Gehre, J. Gernhardt, G. v. Gierke, G. Haas, M. Huang, F. Karger, M. Keilhacker, O. Klüber, M. Kornherr, K. Lackner, G. Lisitano, G. G. Lister, H. M. Mayer, D. Meisel, E. R. Müller, H. Murmann, H. Niedermeyer, W. Poschenrieder, H. Rapp, H. Röhr, F. Schneider, G. Siller, E. Speth, A. Stäbler, K. H. Steuer, G. Venus, O. Vollmer and Z. Yü, Phys. Rev. Lett. **49**, 1408 (1982)

[32]K. H. Burrell, Phys. Plasmas **4**, 1499 (1997)

[33]Z. Lin, T. S. Hahm, W. W. Lee, W. M. Tang and R. B. White, Science **281**, 1835 (1998)

[34]R. J. Taylor, M. L. Brown, B. D. Fried, H. Grote, J. R. Liberati, G. J. Morales, P. Pribyl, D. Darrow and M. Ono, Phys. Rev. Lett. **63**, 2365 (1989)

[35]R. R. Weynants, G. v. Oost, G. Bertschinger, J. Boedo, P. Brys, T. Delvigne, K. H. Dippel, F. Durodie, H. Euringer, K. H. Finken, D. S. Gray, J. D. Hey, D. L. Hillis, J. T. Hogan, L. Konen, R. Leners, A. M. Messiaen, A. Pospieszczyck, U. Samm, R. P. Schorn, B. Schweer, G. Telesca, R. v. Nieuwenhove and P. E. Vandenplas, Nucl. Fusion **32**, (1992)

[36]J. A. C. Cabral, C. A. F. Varandas, M. P. Alonso, P. Belo, R. Canário, H. Fernandes, R. Gomes, A. Malaquias, P. Malinov, F. Serra, F. Silva and A. Soares, Plasma Phys. Control. Fusion **40**, 1001 (1998)

[37]G. V. Oost, J. Adámek, V. Antoni, P. Balan, J. A. Boedo, P. Devynck, I. Ďuran, L. Eliseev, J. P. Gunn, M. Hron, C. Ionita, S. Jachmich, G. S. Kirnev, E. Martines, A. Melnikov, R. Schrittwieser, C. Silva, J. Stöckel, M. Tendler, C. Varandas, M. V. Schoor, V. Vershkov and R. R. Weynants, Plasma Phys. Control. Fusion **45**, 621 (2003)

[38]T. A. Carter and J. E. Maggs, Phys. Plasmas **16**, 012304 (2009)

[39]H. Biglari, P. H. Diamond and P. W. Terry, Phys. Fluids **B 2**, 1 (1990)

[40]R. E. Waltz, G. D. Kerbel, J. Milovich and G. W. Hammett, Phys. Plasmas **2**, 2408 (1995)

[41]B. D. Scott, P. W. Terry and P. H. Diamond, Phys. Fluids **31**, 1481 (1988)

[42]J. C. Perez, W. Horton, R. D. Bengtson and T. A. Carter, Phys. Plasmas **13**, 055701 (2006)

[43]W. Horton, J. C. Perez, T. A. Carter and R. Bengtson, Phys. Plasmas **12**, 022303 (2005)

[44]P. Popovich, M. V. Umansky, T. A. Carter and B. Friedman, Phys. Plasmas **17**, 102107 (2010)

[45]P. Popovich, M. V. Umansky, T. A. Carter and B. Friedman, Phys. Plasmas **17**, 122312 (2010)

[46]S. Zhou, W. W. Heidbrink, H. Boehmer, R. McWilliams, T. A. Carter, S. Vincena, S. K. P. Tripathi, P. Popovich, B. Friedman and F. Jenko, Phys. Plasmas **17**, 092103 (2010)

[47]S. Zhou, W. W. Heidbrink, H. Boehmer, R. McWilliams, T. A. Carter, S. Vincena and S. K. P. Tripathi, Phys. Plasmas **18**, 082104 (2011)

[48]S. Zhou, W. W. Heidbrink, H. Boehmer, R. McWilliams, T. A. Carter, S. Vincena and B. Friedman, Phys. Plasmas (2011) to be submitted

[49]S. L. Chen and T. Sekiguchi, J. Appl. Physics **36**, 2363 (1965)

[50]R. H. Huddlestone and S. L. Leonard, *Plasma Diagnostic Techniques* (Academic Press, New York, 1965), pp. 113-151.

[51]J. P. Gunn, C. Boucher, P. Devynck, I. Duran, K. Dyabilin, J. Horacek, M. Hron, J. Stockel, G. V. Oost, H. V. Goubergen and F. Zacek, Phys. Plasmas **8**, 1995 (2001)

[52]L. Oksuz and N. Hershkowitz, Plasma Sources Sci. Technol. **13**, 263 (2004)

[53]I. H. Hutchinson and L. Patacchini, Plasma Phys. Control. Fusion **52**, 124005 (2010)

[54]Y. Zhang, "Fast Ions and Shear Alfvén Waves", Ph. D. thesis, (2008)

[55]V. Kanarov, D. Siegfried, P. Sferlazzo, A. Hayes and R. Yevtukhov, Rev. Sci. Instrum. **79**, 093304 (2008)

[56]Y. C. Kim and E. J. Powers, IEEE Trans. Plasm Sci. **7**, 120 (1979)

[57]A. E. White, S. J. Zweben, M. J. Burin, T. A. Carter, T. S. Hahm, J. A. Krommes and R. J. Maqueda, Phys. Plasmas **13**, 072301 (2006)

[58]E. T. Everson, P. Pribyl, C. G. Constantin, A. Zylstra, D. Schaeffer, N. L. Kugland and C. Niemann, Rev. Sci. Instrum. **80**, 113505 (2009)

[59]F. F. Chen, *Introduction to Plasma Physics and Controlled Fusion* (Plenum Press, New York, 1984), pp. 219.

[60]R. McWilliams and M. Okubo, Phys. Fluids **30**, 2849 (1987)

[61]A. H. Boozer and G. Kuo-Petravic, Phys. Fluids **24**, 851 (1981)

[62]A. H. Boozer, Phys. Plasmas **9**, 4389 (2002)

[63]J. A. Boedo, P. W. Terry, D. Gray, R. S. Ivanov, R. W. Conn, S. Jachmich, G. V. Oost and T. T. Team, Phys. Rev. Lett. **84**, 2630 (2000)

[64]C. Holland, J. H. Yu, A. James, D. Nishijima, M. Shimada, N. Taheri and G. R. Tynan, Phys. Rev. Lett. **96**, 195002 (2006)

[65]F. Brochard, E. Gravier and G. Bonhomme, Phys. Plasmas **12**, 062104 (2005)

[66]S. I. Braginskii, *Reviews of Plasma Physics, edited by M. A. Leontovich* (Consultants Bureau, New York, 1965), pp. 205-311.

[67]A. Miura and J. R. Kan, Geophys. Res. Lett. **19**, 1611 (1992)

[68]M. V. Umansky, X. Q. Xu, B. Dudson, L. L. LoDestro and J. R. Myra, Commun. Comput. Phys. **180**, 887 (2009)

[69]A. T. Burke, J. E. Maggs and G. J. Morales, Phys. Rev. Lett. **84**, 1451 (2000)

[70]J. R. Penano, G. J. Morales and J. E. Maggs, Phys. Plasmas **7**, 144 (2000)

[71]S. Vincena and W. Gekelman, Phys. Plasmas **13**, (2006)

[72]J. E. Maggs and G. J. Morales, Phys. Plasmas **4**, 290 (1997)

[73]D. C. Pace, M. Shi, J. E. Maggs, G. J. Morales and T. A. Carter, Phys. Plasmas **15**, 122304 (2008)

[74]G. R. Tynan, A. Fujisawa and G. McKee, Plasma Phys. Control. Fusion **51**, 113001 (2009)

[75]I. Furno, B. Labit, M. Podestà, A. Fasoli, S. H. Müller, F. M. Poli, P. Ricci, C. Theiler, S. Brunner, A. Diallo and J. Graves, Phys. Rev. Lett. **100**, 055004 (2008)

[76]C. Theiler, I. Furno, P. Ricci, A. Fasoli, B. Labit, S. H. Müller and G. Plyushchev, Phys. Rev. Lett. **103**, 065001 (2009)

[77]L. Zhao, "Measurements of Classical Transport of Fast Ions", Ph. D. thesis, (2005)

[78]J. D. Huba, *NRL Plasma Formulary* (Naval Research Laboratory, 2007), pp. 31-33.